NANO-ENABLED HYDROGELS FOR CONTINUOUS SURFACE ENHANCED RAMAN SPECTROSCOPY MONITORING OF METABOLITES

A Dissertation

by

YILHWAN YOU

Submitted to the Office of Graduate and Professional Studies of
Texas A&M University
in partial fulfillment of the requirements for the degree of

DOCTOR OF PHILOSOPHY

Chair of Committee,	Michael J. McShane
Committee Members,	Kenith E. Meissner
	Jun Kameoka
	Xiaofeng Qian
Head of Department,	Ibrahim Karaman

May 2019

Major Subject: Materials Science and Engineering

ABSTRACT

Chronic disease management can benefit from continuous real time tracking of disease relevant biochemical levels using minimally invasive implants. Current methods however rely on electrochemical sensing methods integrated into rigid, invasive transdermal probes that are expensive, short lived, and require frequent calibration. The development of new optically interrogatable sensing methods that can be housed in soft biocompatible hydrogel matrixes and implanted subcutaneously can provide a means to extend biosensor life, reliability, and comfort.

This work demonstrates the development of pH responsive surface enhanced Raman spectroscopy (SERS) assays using 4-mercaptobenzoic acid (MBA) capped gold nanoparticles (AuNP). By encapsulating MBA-AuNPs into polyelectrolyte multilayer (PEM) microcapsules (MCs) and then casting MCs into a bulk hydrogel matrix, a soft biocompatible sensor that exhibited pH sensitivity and reproducibility in SERS scattering signal could be developed. To extend this sensing approach to more relevant analytes, enzymatic glucose sensors were prepared with MBA-AuNPs co-encapsulated with glucose oxidase (GOx). SERS spectra recorded from the hydrogels exhibited apparent trends of decreasing pH from 6.50 to 4.50 due to glucose oxidization within the microdomains.

To demonstrate multi-modal sensing capabilities with these SERS approaches, pH and oxygen sensitive microdomains were integrated into a single hydrogel that could be interrogated via SERS and phosphorescence lifetime optical modalities respectively.

The PEM nanofilms were effective at minimizing optical interferences by spatially separating optical probes.

To highlight the benefits of using a PEM MC embedded hydrogel approach, an aggregation based SERS assay with metal nanoparticle encapsulation was studied. The PEM MCs provide vacant pockets where the aggregation-based SERS assay specifically interacts with the analyte, while excluding large proteins which result in non-specific aggregation. As a proof of concept, hybridization-based microRNA-17 sensing assay was embedded in the PEM MCs. In the presence of large protein molecules, microRNA-17 sensing PEM MCs exhibited target level dependent SERS signal changes.

The above results demonstrate significant advances in enabling SERS sensing assays to be integrated into soft biocompatible hydrogels while still retaining selectivity and repeatability via the use of PEM MCs. This lays the foundation for developing implantable SERS biosensors that can be integrated with other sensing strategies to develop multimodal multi-analyte sensors.

DEDICATION

I dedicate this dissertation to my wife, Minhee Kim, who has fully supported me throughout this journey.

ACKNOWLEDGMENTS

I would like to express my sincere gratitude to my committee chair, Dr. Michael McShane, for his endless support and guidance during my journey at Texas A&M University. I also want to thank my committee members, Dr. Kenith Meissner, Dr. Jun Kameoka, and, Dr. Xiaofeng Qian for their encouragement and support throughout this research.

I would like to sincerely acknowledge Dr. Ashvin Nagaraja for imparting me practical knowledge on research techniques and methodology. I am particularly grateful to Dr. Aniket Biswas for the numerous useful discussions and also for photoluminescence life time measurements. I want to thank Dr. Jinha Hwang and Dr. Swayoma Banerjee for acquiring and providing me with TEM and confocal microscopy images respectively for my research. I would like to thank Dr. Gerard Coté, Dr. Andrea Locke, Miss Monika Schechinger and Dr. Haley Marks for their contributions and advices in microRNA-17 sensing. I am grateful to Dr. Jung Heon Lee and Mr. Si Hyun Kim for their collaboration and suggestions in adenosine sensing. I want to acknowledge Mr. Alex Quinn, Dr. Javier Garza, Dr. Subin George, Mr. Abishai Dominic, and Miss Priyanka Vasanthakumari for their friendship and advices in my research. Finally, I would like to express my tremendous gratitude to my wife, two daughters, parents, and parents in law for their unconditional love, patience, encouragement and support.

CONTRIBUTORS AND FUNDING SOURCES

Contributors

The work in this dissertation was supervised by a committee composed of Dr. Michael McShane (chair) of the Department of Biomedical Engineering, Dr. Kenith Meissner of the Department of Physics at Swansea University, Dr. Jun Kameoka of the Department of Electrical and Computer Engineering, and Dr. Xiaofeng Qian of the Department of Materials Science and Engineering.

Phosphorescence lifetime data (Figures 3-16B, 3-17, and 3-18) was collected by Dr. Aniket Biswas. TEM images (Figures 3-2 and 4-4B) and confocal images (Figure 3-7) were captured by Dr. Jinha Hwang and Dr. Swayoma Banerjee, respectively. A darkfield image and reflectance spectra were recorded by Mr. Byron Cheatham (CytoViva, Auburn, AL, USA). All other work in the dissertation was completed by the author independently.

The oligonucleotides used for the study in Section 5 were provided by Dr. Coté's group. The protocol for oligonucleotide conjugation to metal nanoparticles for microRNA-17 sensing was obtained from Miss Schechinger and Dr. Locke in the same group. All Raman data presented in this dissertation was collected using the Raman spectrometers in Dr. Coté's group.

Funding Sources

This work was supported partially by a grant (CBET #1403002) from the National Science Foundation and by a funding (Award#1648451) from the Engineering

Research Center for Precise Advanced Technologies and Health Systems for Underserved Populations (PATHS-UP).

TABLE OF CONTENTS

Page

LIST OF FIGURES

Page

LIST OF TABLES

Page

1. INTRODUCTION

According to the definition by US National Health Statistics, chronic diseases are characterized by a long-lasting condition (longer than 3 months).[1] Chronic diseases are one of the major causes of mortality. In 2005, 61 % of human death worldwide was related to chronic diseases such as cardiovascular diseases, cancer, chronic respiratory diseases, diabetes, etc.[2] In 2010, approximately 50 % of adults in the United States was influenced by one chronic disease while nearly 26 % of adults suffered from two or more chronic conditions.[3] Health care costs spent on treating patients with chronic diseases are becoming a financial burden.[4] For example, nearly 300 billion US dollars was spent on the Medicare program in 2010. 93 % of this expenditure was used to take care of senior citizens (over 65 years old) who have two or more chronic diseases.[5] The main problematic characteristic of a chronic disease is its resistance to treatment. This means that the patients with chronic diseases need to monitor and manage their symptoms ahead of time.

Detection of physiologically relevant biochemicals in patient's body plays a crucial role in the diagnosis and treatment of chronic diseases. Traditional biochemical measurements have been performed using laboratory based analytical equipment which requires high costs and long analysis time. Moreover, frequent analytical measurements are needed for patients to improve the quality of disease treatment. To achieve this, biosensors have been utilized over the past decades since Clark and Lyons showed the first concept by indirectly measuring glucose concentration using an electrochemical

electrode combined with glucose oxidase.[6] For example, diabetes patients check their glucose levels from a drop of blood extracted from their fingers using lancet devices. With such a method, the diabetes patients could access their blood glucose level more easily in comparison to visiting a clinical laboratory. However, this method is still limited since the diabetes patients obtain only single snap shot of their analytical level. It is hard for them to regulate their symptoms without tracking dynamic changes in blood glucose level.

Minimally invasive biosensors can be a solution for this problem since they continuously monitor the glucose levels in the interstitial fluid which is highly correlated with blood glucose levels. Microdialysis method utilizes an implantable hollow fiber to extract interstitial glucose from the subcutaneous tissue.[7] An isotonic buffer solution is circulated through the implanted fiber. Analyte molecules whose size is smaller than the molecular cutoff of semipermeable membrane diffuse from the interstitial fluid to the buffer solution, which are then transported to an external glucose sensor. This method circumvents a sensitivity degradation issue by implanting a sensing compartment in the subcutaneous tissue. Nonetheless, permanent skin puncture and glucose sensing response delay need to be overcome for real life applications.[8-9] Alternatively, continuous glucose monitoring devices (CGMs) have been developed with a subcutaneous electrode. Glucose oxidase (GOx) is immobilized in a polymeric layer coated on the subcutaneous electrode. The interstitial glucose in the subcutaneous tissue diffuses into the polymeric layer and is further catalyzed by the GOx, producing hydrogen peroxide as an enzymatic reaction byproduct. As a result, an electric current proportional to the interstitial glucose

level is generated by the oxidation of the produced hydrogen peroxide. Several types of subcutaneous electrodes for glucose sensing have been commercialized after they were approved by FDA.[10] However, the host response induced by the implantation of the electrode, not only requires frequent calibrations with the finger prick method but also needs weekly replacement of the electrode.[11]

Fully implantable sensors can be alternatives to the commercially available minimally invasive methods. The fully implantable sensors are free from serious tissue trauma, potential infections, and inflammatory responses since there is no physical connection between an interstitial fluid sampling site and an external device. Mortellaro and DeHennis reported a clinical glucose sensing in human subjects for 28 days using fully implantable optical biosensors.[12] An LED excitation source and arrays of Ferrite Antenna (for remote power charging and wireless communication) were encased by a hydrogel containing a non-enzymatic glucose sensing chemistry. Interstitial glucose diffuses through the hydrogel and reversibly bind to boronic acid functional groups of fluorescence dyes conjugated in the hydrogel. This glucose binding induces an increase in fluorescence through photoinduced electron transfer disruption. However, high power consumption due to a LED light source limits the miniaturization of this glucose sensor.[13]

Soft hydrogel based fully implantable optical biosensors can also be applied in continuous biochemical monitoring. Since hydrogels possess tissue like mechanical properties, a host response related to mechanical mismatch between skin tissues and implants can be minimized. Biofouling issue of implants can be also resolved by

adopting thermally responsive hydrogels or inverted colloidal crystal hydrogels.[14-15] Our group has developed enzymatic glucose sensing hydrogels by co-encapsulating GOx and oxygen sensitive porphyrin dye in the same matrix.[16] When interstitial glucose diffuses into the hydrogel matrix where the GOx is immobilized, oxygen is consumed as a result of the enzymatic reaction. Therefore, glucose level in the interstitial fluid can be accessed by indirectly measuring oxygen concentration using phosphorescence. The biocompatibility of this sensor can be further improved by the hydrogel matrix. However, such an additional modification can influence the diffusion of analytes via the matrix. By isolating the sensing compartment into microdomains dispersed in the hydrogel, we can independently control the biocompatibility and the analyte transport (See Figure 1-1).

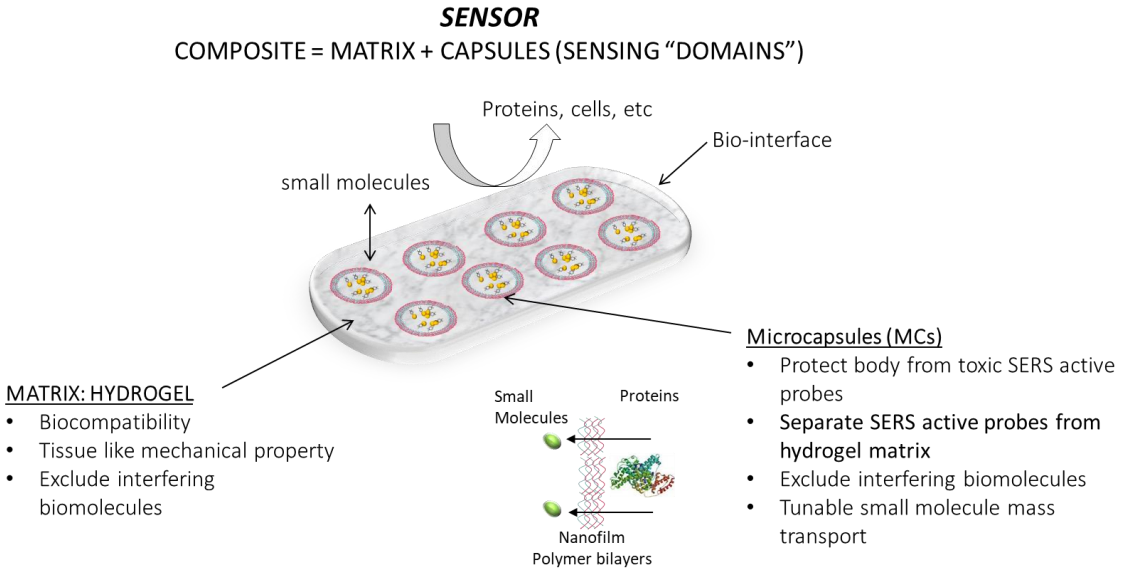

Figure 1-1. Schematic diagram of the hydrogel composite containing microdomains.

These microdomain-based hydrogels were combined with phosphorescence-based oxygen sensing chemistry to measure dissolved oxygen and/or glucose. In addition, this unique hydrogel structure also finds attractive applications in other sensing chemistries especially that based on SERS. Nanofilm microdomains prevent SERS active nanoprobes with potential toxicity from leaching to the body. On the other hand, the nanofilm microdomains also exclude large biomolecules which may interfere with SERS signals to enter the hydrogel. Moreover, by embedding SERS based and phosphorescence based sensing chemistries in discrete microdomains, multimodal-mulitanalyte sensing hydrogel sensors can be synthesized.

The contents in this dissertation have been organized to depict the development of unique SERS based hydrogel biosensors and to describe the practical knowledge necessary to encapsulate aggregation based SERS sensing assay in microdomains. Section 2 describes the backgrounds for this work: theoretical overviews of optical sensing modalities, other prior works in glucose sensing, and other hydrogel based SERS sensor designs. Moreover, each section contains more detailed background for the specific study. Section 3 describes the material characterization of hydrogel sensors and the development of multimodal (SERS/phosphorescence) hydrogel sensors. Section 4 illustrates the development of enzymatic glucose sensing hydrogels using pH sensitive SERS probes; a portion of this section was published in the *Proceeding of IEEE Sensors* and *IEEE Sensors Journal*. In Section 5, the encapsulation of hybridization-based microRNA-17 sensing assay in microdomains is presented to prove the feasibility of adopting aggregation based SERS assays in microdomain based hydrogels. A portion of

this section was published in the *Proceeding of SPIE*. Finally, Section 6 depicts the optimization of experimental method to synthesize an aggregation based nanoparticle assay with aptamers which can be potentially embedded in the microdomain based hydrogels for continuous SERS monitoring.

2. BACKGROUND

The main goal for this work is to develop a hydrogel based SERS sensor which can be used for minimally-invasive small molecule monitoring. For example, by incorporating SERS based pH sensing hydrogel with glucose-sensitive enzyme, glucose concentration can be indirectly monitored using external optical devices. Such hydrogel based SERS sensors are designed to be implanted subcutaneously. The external optical glucose reader can continuously interrogate glucose concentration in the interstitial fluids near the implanted SERS based hydrogel sensor. As the development of these sensors depends on certain fields of knowledge such as materials science and optics, it is crucial to understand related theories and previous works from other research groups. Thus, a review of non-invasive glucose monitoring technologies which compete with minimally-invasive glucose sensors is presented in this section. The theories of optical phenomenon such as Raman, SERS, and phosphorescence lifetime, which can be used as potential sensing modalities for either minimally invasive or non-invasive glucose sensing are also presented. More importantly, the previous efforts to develop hydrogel sensors based on SERS modality are reviewed. In addition, multimodal sensing approaches containing SERS sensing are also given.

2.1. **Non-invasive biochemical sensing**

Most of commercial biosensors are based on the invasive blood sampling, which involves acute levels of pain. Initial improvements of such biosensors were focused on

either reducing the blood sample volume (about few μL) or collecting the blood samples from the body areas (i.e. hand, arm, and thigh) more susceptible to pain than finger. In case of glucose sensing, minimally invasive methods using interstitial fluids have been developed. The glucose level in the interstitial fluids has a strong correlation with that in the blood.[17] However, the use of subcutaneous electrodes in this approach still causes discomfort for the patient. To enhance patient compliance, glucose measurements need to be performed non-invasively. Non-invasive glucose sensing can be enabled by substituting blood samples with other biological fluids such as urine,[18] sweat,[19] and saliva.[20] Even though such fluids can be sampled non-invasively, these approaches are suffered by two main limitations. First, the glucose concentration in non-blood biological fluids is poorly correlated with that in blood. Second, patients are not able to continuously track their glucose levels using non-invasively collected fluids. Therefore, for continuous glucose monitoring, measurements need to be performed directly from body tissues such as skin,[21] tympanic membrane,[22] retinal tissue,[23] eye iris,[23] and oral mucosa.[24]

The techniques to continuously monitor glucose level from body tissues can be categorized into two groups: electrical techniques and optical techniques.

2.1.1. **Electrical techniques**

The intrinsic electric/dielectric property of tissues varies with the fluctuation of blood glucose level. Bioimpedance spectroscopy utilizes a low-cost LC resonance circuit to monitor glucose level from the skin by applying AC current of a low amplitude to

electrodes connected to the skin. The LC resonance circuit measures voltage changes as a function of frequency (100 to 100 MHz). The change in blood glucose level results in the variations of Na^+ and K^+ ion concentrations in the red blood cells which in turn induces a change in the membrane potential of the red blood cells.[25] Therefore, the blood glucose level can be estimated by measuring the resistivity and dielectric permittivity of the red blood cell membrane using the frequency dependent impedance spectrum. This technique was utilized in a wrist band type glucometer, named as Pendra (Pendragon Medical Inc., Zurich, Switzerland).[26] Nonetheless, this glucometer disappeared from the market due to poor reliability and long calibration time (about 60 min). Another electrical technique based on the dielectric change in blood is electromagnetic sensing. An electromagnetic sensor utilizes eddy currents to measure the conductivity variations of the blood, induced by the changes in blood glucose level. The sensor consists of two induction coils which are spatially separated in the medium. An AC voltage with a frequency of approximately 4 MHz is applied to the primary induction coil as an input signal, while the output signal is monitored at the secondary induction coil.[27] The output signal varies with the blood glucose dependent conductivity fluctuation in the medium. The glucose sensitivity of this technique can be optimized by tuning the frequency of input signal. However, such optimized frequency has a strong dependency on the temperature of the tested medium. Reverse iontophoresis is another electric technique which is not based on measuring the intrinsic dielectric parameter change in tissue but on directly measuring extracted glucose through the epidermis surface. Two electrodes (cathode and anode) are attached on the skin surface. When a DC potential is applied

between the cathode and the anode, sodium ions are attracted to the iontophoretic cathode, generating an electric current.[28] Such ion migration results in electro-osmotic flow which transports the interstitial glucose to the iontophoretic cathode where electrochemical enzymatic glucose sensor is located. This technique was adopted by the GlucoWatch (Cygnus Inc., Redwood City, CA, USA), which was clinically approved by FDA in 2001.[29] Even though the device is based on measuring interstitial glucose which is strongly correlated to blood glucose, it was withdrawn from the market due to skin irritation and long warming-up time.

2.1.2. **Optical techniques**

Near infrared (NIR) absorption spectroscopy is a well-established analytical method to quantify the glucose concentration in the tissue. The magnitude of characteristic glucose absorption peaks can be used to track the blood glucose level.[30] In this technique, a laser with wavelengths between 750 and 2500 nm is focused on the body tissues providing a penetration depth of 1-100 mm.[31] This wavelength range is selected owing to a comparably weak light absorption by water in that range. A photodetector measures the intensity variations of reflectance and transmittance in the body tissue. The absorption and scattering coefficients of the tissue are affected by the change in glucose concentration. One of main drawbacks of this method is that the glucose signal is interfered by the stronger NIR bands of skin tissue, proteins, and hemoglobin. Moreover, this method is quite limited since it is affected not only by physicochemical variables but also by environmental changes. To overcome the signal

interference issue, middle NIR (MIR) excitation source (2500 to 10000 nm) is employed.[32] When the excitation wavelength is increase to the MIR range, the scattering from interfering species diminishes while the width of glucose peak becomes narrower in comparison to the MIR range. As the penetration depth of MIR (about few micrometer) in the skin tissue is much shorter than that of NIR, transmission based measurement cannot be performed with this approach. Alternately, attenuated total reflection (ATR) is adopted to increase the light penetration through the skin tissue. The ATR is based on total internal reflection of light through a crystal. When the crystal is in physical contact with the surface of skin, the electromagnetic field induced by the reflected light interacts with the interstitial glucose in the dermis.[33] However, the glucose monitoring with MIR has a strong dependency on the water content in the skin.[34]

Thermal emission spectroscopy is another IR based non-invasive glucose sensing technique. Instead of measuring how external IR light interacts with blood glucose in the tissue, this technique measures IR radiation emitted from the body. Characteristic thermal IR radiation is affected by the change in glucose concentration in the tissue. The device structure of thermal emission spectroscopy is similar to that of a tympanic membrane thermometer. However, in the case of thermal emission spectroscopy, the IR wavelengths for characteristic glucose fingerprint (9.8 and 10.9 μm) are also added. Tympanic membrane is optimal for glucose measurement since optical path between the blood vessel and the IR detector is smaller than any other body parts. Although this technique showed good measurement reproducibility, it still suffers from the noises due to temperature fluctuation and body movements.[35-36]

Optical polarimetry is also employed to non-invasively measure glucose level in the body tissue. Optically active molecules such as glucose rotate the linear polarization vector of incident light. Nonetheless, the high scattering nature of the skin completely depolarizes the incident beam. Hence, the humor of the eye is considered as an alternate optimal target because it contains an optically clear medium. Moreover, the glucose level in the humor of the eye corresponds to that in the blood with a maximum time lag of 5 min.[37] Unlike other optical techniques, the optical polarimetry is not influenced by physiological conditions including pH and temperature.[38] This technique possesses some obstacles like optical artifacts due to the eye movement, safety concerns for light exposure to the eye, and optical noises from other optically active substances in the aqueous humor. In addition to optical polarimetry, Raman spectroscopy can be also utilized to monitor the glucose concentration in the humor of the eye. In comparison to NIR spectroscopy, the Raman spectroscopy has two main advantages: the Raman signal of water is weaker than that of Raman active analyte and the Raman vibrational band of the analyte are narrower.[39] Therefore, the characteristic Raman peaks of glucose are easily discernible from those of other substances. Lambert et al. reported successful Raman measurement of glucose in human aqueous humor using a 785 nm laser.[40] Due to the low efficiency of Raman scattering, a relatively long spectral collection time is necessary for this technique. Such a long exposure of laser may cause photothermal eye damages.

Overall, most of non-invasive glucose sensing techniques are limited by low signal-to-noise ratio (SNR). Therefore, there is a strong need to develop new transducers

and techniques to solve this problem. In addition, the miniaturization of measurement devices is essential for patients to monitor their blood glucose levels continuously.

2.2. **Raman scattering**

In 1928, Raman and Krishnan first observed the energy difference between incident photons and scattered photons from molecules in both liquid and vapor phases.[41] When light is irradiated to electrons, atoms, or molecules, it is scattered randomly in all directions.[42] The energy of photons in scattered light can be either same as or different from that of incident photons. The scattering process in which photons retain their initial energy is called Rayleigh scattering (or elastic scattering) while the other process is called Raman scattering (or inelastic scattering). The Raman scattering is categorized into two types of spectral transitions: Stokes scattering and anti-Stokes scattering. As illustrated in Figure 2-1, in the process of Stokes scattering, the incident photon interacts with a molecule at the ground state. Some energy of the incident photon is transferred to the molecule, thus elevating the energy state of the molecule. On the other hand, in case of anti-Stokes scattering, the incident photon interacts with a molecule which is already in the excited state. The energy of excited molecule is transferred to the incident photon while the molecule goes back to its ground state. The amount of energy difference in Raman scattering process (energy gain or loss) is equivalent to rotational or vibrational energy level of the molecule.[43] The population of energy states of molecules follows the Boltzmann distribution.[44] Molecules have a higher tendency to occupy the ground vibrational state than vibrationally excited states.

Therefore, the intensity of Stokes scattering is much higher than that of anti-Stokes scattering.

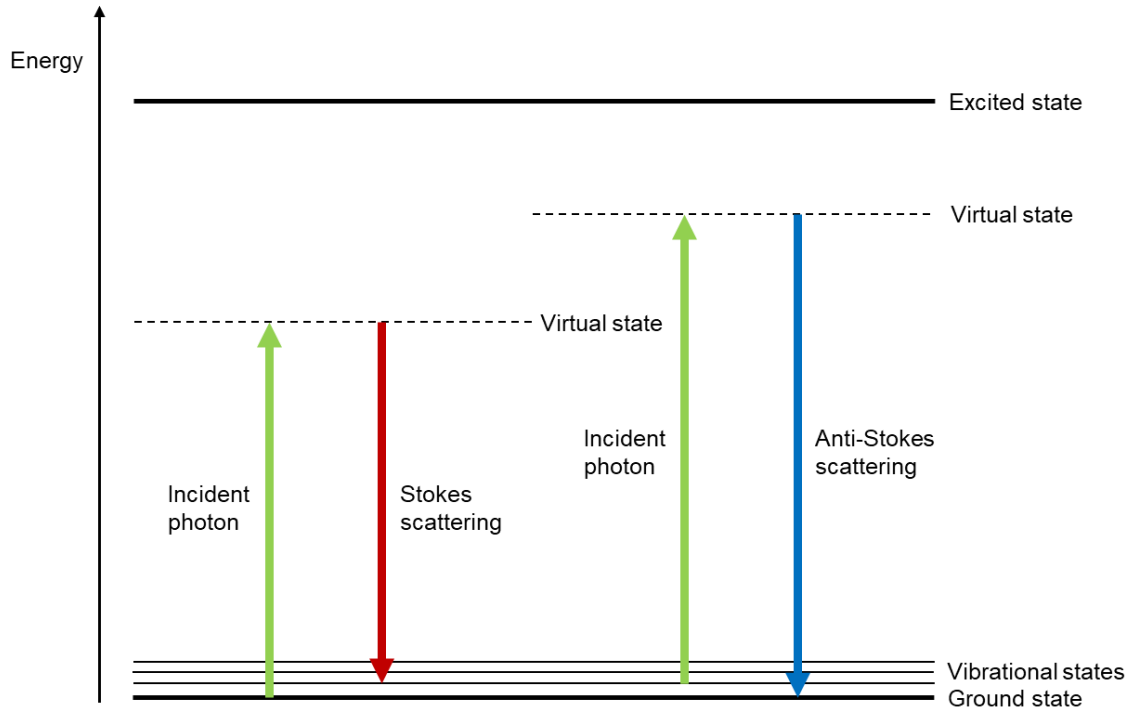

Figure 2-1. Schematic diagram of Raman scattering processes.

Raman scattering can be explained by the interaction between electromagnetic field and the polarizability of a molecule.[45] When an external electromagnetic field (E) is applied to a molecule, an induced dipole moment is created on the molecule ($\mu_{induced}$) which is proportional to the polarizability of the molecule ($\alpha_{molecule}$):

$$\mu_{induced} = \alpha_{molecule} E$$

The polarizability of the molecule in this equation indicates the degree of distortion of electron cloud around the molecule. A molecular vibrational band is Raman active only if there is a change in polarizability during the vibration:

$$\left(\frac{d\alpha}{dq}\right)_0 \neq 0$$

where q and 0 represent the normal coordinates for the molecular motion of a normal vibration and equilibrium state, respectively.[46] The symmetry of a molecule is another parameter that determines whether a molecular vibrational band is Raman active or not. If a molecule has a symmetric center, any normal vibrational mode of the molecule cannot be both Raman and IR active.[47] Vibrational modes that involve polarizability modulation is Raman active while those with dipole moment modulation is IR active.

Raman scattering is much less intense than Rayleigh scattering since only one in $10^6 – 10^8$ scattered photons takes part in the Raman scattering process.[48] The intensity of Raman scattering can be depicted as:

$$\mathrm{I} = Kl\alpha^2\omega^4$$

where K is the speed of light, l is the power of incident light, α is the electron polarizability in a molecule, and ω is the frequency of the incident light.

2.3. **Surface enhanced Raman spectroscopy (SERS)**

In 1977, Jeanmaire and Van Duyne first discovered SERS phenomenon.[49] They showed that the Raman signal from molecules that are absorbed on the roughened silver surfaces was extremely amplified. Since then, many other groups have reported the

SERS effect with various SERS substrates such as roughed metallic electrodes,[50-51] plasmonic nanoparticles,[52-53] plasmonic nanoshells,[54-55] metal film over nanospheres (MFONs),[56-57] nano-patterned plasmonic structures.[58-60] When a molecule is held in the vicinity of a SERS substrate surface, Raman signal of the molecule is extremely enhanced. Such signal enhancement can be understood by two mechanisms: chemical enhancement and electromagnetic enhancement.

Chemical enhancement, also known as charge transfer enhancement, occurs when molecules absorb directly on the SERS active surface. The formation of adsorbate-metal complex elevates molecular polarizability due to the interaction between molecular orbitals of the molecules and conduction band electrons of metal.[61] In this case, an electron in the Fermi level of the metal transfers to the lowest unoccupied orbital (LUMO) of the molecules. Such an electron transfer is in a resonance with the frequency of incident photon. Then the electron in the LUMO level of the molecule relaxes back to the Fermi level of the metal. This whole electron transfer process results in the enhancement of Raman signal due to the increase in molecular polarizability. The enhancement factor for chemical enhancement process was calculated to be $10^0 – 10^2$ both theoretically and experimentally.[62]

In order for the molecule to experience electromagnetic enhancement, two requirements need to be satisfied. First, the molecule needs to be located within close proximity to a metal surface. Second, there needs to be a coupling between a metal nanoparticle and incident light.[63] Collective oscillation of conduction electrons of the metal nanoparticle upon light incidence occurs when the oscillation frequency is in

resonance with the frequency of incident light. Such a resonance is referred as localized surface plasmon resonance (LSPR). When an electromagnetic field is applied to a spherical metal nanoparticle, the electromagnetic field at the surface of the metal nanoparticle can be expressed as

$$E_r = E_0 cos\theta + g\left(\frac{r^3}{d^3}\right) E_0 cos\theta$$

where E_0 is the total electromagnetic field at a distance d from the metal nanoparticle surface, r is the radius of the metal nanoparticle, θ is the angle relative to electromagnetic field direction, and g is a constant which is a function of the frequency of incident light. g can be described by

$$g = \left(\frac{\varepsilon_1(\omega_L) - \varepsilon_0}{\varepsilon_1(\omega_L) + 2\varepsilon_0}\right)$$

where ω_L represents the frequency of incident light. ε_0 and ε_1 denote dielectric permittivities of the medium surrounding the metal nanoparticle and of the metal nanoparticle, respectively.[48] At the plasmon resonance frequency, ε_1 becomes close to -2 resulting in the maximum of g. Therefore, at that frequency, the surface plasmon excitation enormously enhances the local electromagnetic field around the surface of the metal nanoparticle. The electrons in the molecules present at the vicinity of metal nanoparticle surface are more polarized by the enhanced local electromagnetic field. Such intensified polarization results in the amplification of Raman scattering of the molecule. The enhancement factor of electromagnetic enhancement was reported to be 10^4 - 10^8, which is much higher than that of chemical enhancement.[64]

2.4. **Phosphorescence lifetime**

When a molecule absorbs a photon, it is excited from the ground state (S_0) to high energy singlet states (either S_1 or S_2) as shown in Figure 2-2. A molecule at any higher vibrational level in S_1 loses energy through vibrational relaxation process to reach the lowest vibrational level of S_1. A molecule in state S_2 undergoes vibrational relaxation to its lowest vibrational level in state S_2 and then transits to the highest level in S_1 through internal conversion process. The molecule then reaches the lowest level of S_1 after several steps of vibrational relaxation. Both vibrational relaxation and internal conversion are nonradiative processes. Two main emission processes from S_1 to the ground state (S_0) are fluorescence and phosphorescence. In the fluorescence, the molecule at S_1 state relaxes back directly to S_0 state, releasing a photon of energy equal to the energy difference between those two states. Fluorescence has a high chance of occurrence compared to phosphorescence since there is no change in the spin multiplicity. The fluorescence lifetimes are about 1 to 100 ns.[65] In the case of phosphorescence, the molecule at the lowest level in the S_1 state transfers to the highest level of triplet state (T_1) by nonradiative intersystem crossing. This transition is less probable since it involves a change in the spin multiplicity. The molecule then goes through vibrational relaxation until it reaches the lowest level of T_1. The energy state of T_1 is lower than that of S_1 and the molecule in the T_1 state returns to the ground state (S_0) by emitting a photon. This molecular transition from T_1 to S_0 is forbidden.[66] Thus, phosphorescence lifetime is much longer than fluorescence lifetime (approximately from 1 μs to 10 s). Such long lifetimes allow phosphors to interact with other molecules. For

instance, the phosphorescence of oxygen sensitive phosphor can be collisionally quenched by molecular oxygen. Since collisional quenching is a diffusion-limited reaction, it can be described by the Stern-Volmer relationship:[67]

$$\frac{\tau_0}{\tau} = 1 + k_q \tau_0 [O_2] = 1 + K_{SV}[O_2]$$

where τ_0 and τ represent phosphorescence lifetime in the presence and absence of the molecular oxygen, respectively, k_q denotes the bimolecular quenching constant, K_{SV} is the Stern-Volmer quenching constant, and $[O_2]$ is molar oxygen concentration. In case of diffusion-controlled quenching, k_q can be further expressed by Smoluchowski equation:[68]

$$k_q = \frac{4\pi N_A f_q}{1000}(R_P + R_Q)(D_P + D_Q)$$

N_A is Avogadro's number, fq is the efficiency of collisional quenching, R_P and R_Q are the radii of phosphor and quencher, respectively, and D_P and D_Q are diffusivities of phosphor and quencher, respectively. With the fixed experimental condition, bimolecular quenching constant (k_q) is constant and reflects quenching efficiency or the accessibility of oxygen to phosphor.

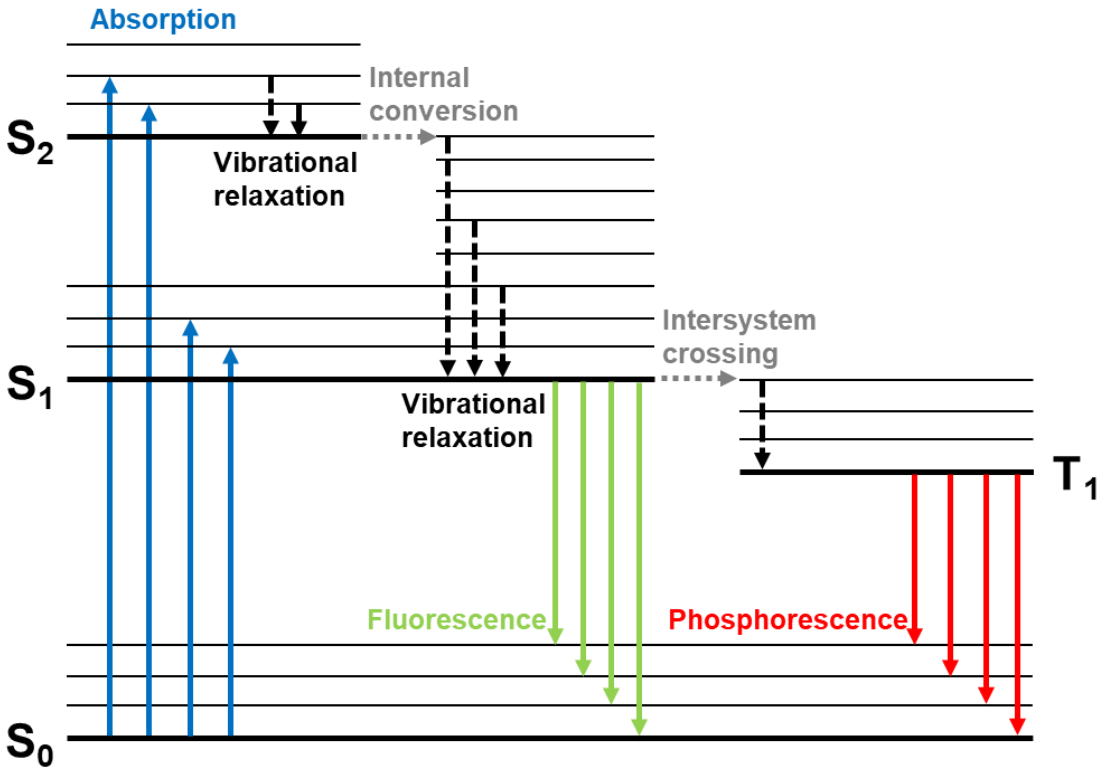

Figure 2-2. Jablonski diagram.

2.5. **Direct SERS sensing**

Direct SERS sensing is based on the intrinsic Raman signature of analytes. When an analyte is placed in the vicinity of a plasmonic metal surface, the Raman signal of the analyte is amplified by the strong local electromagnetic field. The intensity of the amplified Raman signal, known as SERS signal, is used to quantify the concentration of the analyte. The simplest direct SERS sensing can be performed by placing the analyte in close proximity to the unmodified SERS active substrate. The Raman active analyte can be adsorbed on the plasmonic metal surface by various molecular interactions

namely, physisorption, chemisorption, and electrostatic attraction. Most molecules are physisorbed on the surface through dipole-dipole, dipole-ion, and dispersion (London force) interactions. The molecules functionalized with either cyanide or thiol groups are chemisorbed on the plasmonic metal via covalent bonding.[69-70] Charged molecules containing ammonium and carboxyl groups tend to adsorb onto the noble metal surfaces through electrostatic interactions. Moreover, the surface of SERS substrate can be functionalized with appropriate functional groups if the molecules have low affinities to the plasmonic metal surface. For instance, in order to detect non-polar organic molecules like polychlorinated biphenyl (PCB) or polycyclic aromatic hydrocarbon (PAH), the plasmonic metal surfaces are functionalized with non-polar organic ligands.[71-72]

2.6. **Hydrogel based SERS sensors**

The immobilization of plasmonic nanoparticles in the hydrogel matrix can be an innovative solution for *in vivo* SERS sensing. Biocompatible hydrogel scaffolds possess tissue like mechanical properties. Biofouling effect can be minimized by modifying the surface functionality of hydrogels. In addition, hydrogels can protect surrounding tissues from potential toxicity of plasmonic nanoparticles. The most common synthetic method for SERS sensing hydrogels is attaching nanoparticles directly to the hydrogel matrix. For example, Kim *et al.* encapsulated gold AuNPs in semipermeable microgels which filter relatively large biomolecules allowing small analyte of interest diffuse through hydrogel matrix and then interact with SERS active AuNPs.[73] Moreover, the size-cutoff of microgels was tuned by controlling the crosslinking density of the hydrogel matrix.

This approach has the potential to provide a means of detecting Raman active small biomarkers in biological fluids without sample pre-treatment. However, the types of detectable analytes are limited since such SERS based hydrogel systems are only dependent on direct SERS sensing mechanisms. Another strategy to build SERS based hydrogel sensors is by incorporating Raman dye conjugated nanoparticles with stimulus responsive hydrogel scaffolds. Mitomo *et al.* controlled the dynamic gap of plasmonic nanomaterials in hydrogels by using salt concentration dependent hydrogel volume changes.[74] By alternatively exposing the hydrogels to DI water and NaCl solution, reversible LSPR shifts due to dynamic gap changes were also achieved. Through such reversible volume expansion of the hydrogels the trapping efficiency of relatively large target molecules in hot spots was increased significantly showing significantly improved SERS sensitivity. This approach has the advantage of sensing relatively large molecule such as biomolecules which cannot be trapped in small nanoparticle gaps. Overall, these hydrogel based sensing approaches are limited, since additional Raman background is always arising from the matrix employed. In addition, nanoparticle aggregation based assays with high target sensitivity and selectivity cannot be encapsulated in these hydrogel structures.

2.7. **Multimodal sensing**

Multimodal sensing containing a SERS modality is a relatively new field of technology and has been mainly focused on cellular imaging research.[75] One of the examples of this multimodal sensing is the fusion of SERS and fluorescence. SERS has

several advantages over fluorescence owing to narrower signal bandwidth facilitating multiplexing ability. In the other hand, fluorescence provides a faster imaging capacity with higher sensitivity compared to SERS. Therefore, by combining the advantages of both optical modalities synergistically create a powerful analytic tool. Recently, SERS-fluorescence encoded particles (SFEPs) have been developed for dual modal bio-sensing and imaging applications.[76-78] These SFEPs initially utilize fluorescence modality for rapid imaging and SERS modality for detailed multiplex imaging. There are two main structures for the SFEP. First, single metal nanoparticle core conjugated with SERS active molecules and subsequently coated with silica nanoshell. Finally, fluorophores are decorated on the silica nanoshell surface.[79] Second approach is inverse structure of the first method, where individual fluorescent up-conversion nanoparticles (UCNPs) are used as the core.[80] In this case, silica nanoshell is formed onto the UCNP, followed by attaching SERS active molecule decorated metal nanoparticles. Some of the main challenges for using the SFEP for multimodal sensing are fabrication complexity, potential fluorescence quenching by non-radiative energy transfer between fluorophore and plasmonic nanoparticle, and requirement for separate excitation sources for each optical modality.

2.8. **Summary**

Several non-invasive glucose sensing approaches have been attempted with various electrical and optical techniques. However, the major disadvantage of these approaches is that they suffer from low SNR due to interference. To mitigate this

problem, a minimally invasive approach using hydrogel implants can be used for continuous glucose monitoring. SERS provides high signal amplification due to the LSPR effect. By adopting SERS into these hydrogel implants, the continuous glucose sensing with high sensitivity can be achieved. In the following sections, the glucose sensing with SERS based hydrogel sensor will be presented. In addition, to achieve dual modal glucose sensing, phosphorescence lifetime based oxygen sensing compartment will be combined with the SERS based hydrogel sensor. Such dual modal glucose sensing hydrogels can be potentially implanted in the dermis of diabetic patients providing redundant glucose measurement for error-checking over time. Moreover, SERS sensing with aggregation based nanoparticle assay will be also explored to increase the number of potential analyte which can be detected with this SERS based hydrogel implants.

3. MULTIDOMAIN-BASED RESPONSIVE MATERIALS WITH DUAL MODE OPTICAL READOUTS

3.1. **Introduction**

Multimodal sensing refers to the coupling of multiple measurement modalities—particular methods or procedures—into a single system. By combining two methods, complementary data may be obtained from a common sample, enhancing both the quantity and quality of information collected. This concept is well known in the analytical arena, where "hyphenated techniques" typically involve the combination of a separation technique (chromatography) and a detection method (spectroscopy).[81] Multimodal imaging is also frequently referenced in the microscopy and medical arenas,[82] where combinations such as positron emission tomography and X-ray computed tomography (PET-CT) are available even as commercial instruments.[83] However, such multimodal analysis is less commonly applied to the arena of sensors and monitoring systems, where the focus is on accurate detection and/or continuous observation of one or more molecules of interest.

Chemical sensors and biosensors typically require use of specialized materials at the interface of the sample of interest and the measurement system, which act to transduce and in some cases amplify the target analyte into a measurable quantity with specific electrical, mechanical, optical features. Historically, this has been involved use of a single measurement modality because of the complexity involved with sensor development. Recently, as sensor technology has matured to enable more widespread

sensor deployment, an interest in sensor networks/fusion has led to the concept of combining measurements from an array of devices involving multiple measurement modes that together produce a pattern of response that enhances the characterization the state of the observed sample—additional properties, increased accuracy, etc. Such approaches are applies to sensor networks and sensor fusion aspects commonly found in robotics, autonomous vehicles, and smart structures.[84]

In the current sensor network/fusion paradigm, it is the individual output signals from many discrete sensors that are combined. Rarely has the concept of multimode transducers been discussed. The specific rationale for a material that serves to transduce and/or amplify multiple signals arises from the desire to improve accuracy of measurements using complementary, partially orthogonal methods. The more general rationale is simply endowing a capability for multiparametric sensing/monitoring the material environment. Some examples include combinations of multiple electrochemical modes (e.g. amperometric and stochastic)[85], and a single photonic sensor configurable as a photodetector in the absorptive mode and as a pyrodetector in the photonic sensor mode.[86]

In this paper, we describe what we believe is the first development of composite responsive materials designed to generate signals for a combination of surface enhanced Raman spectroscopy (SERS) and phosphorescence lifetime measurements of small molecule targets. These techniques are complementary in terms of interactions with samples and measurement techniques, making their combination attractive but also challenging. Since observed by Van Duyne in 1977,[87] surface enhanced Raman

spectroscopy (SERS) has been extensively studied in the fields of biomedical research owing to its exquisite sensitivity for detection of a broad class of molecules.[88-89] The extremely high measurement sensitivity is achieved using plasmonic nanosurfaces that produce a strong electromagnetic interaction with an adsorbed Raman-active molecule. [90] This phenomenon has been well-studied and is generally accepted as a means to locally amplify both the incident and inelastically-scattered light from the Raman-active molecule resulting in a signal enhancement of a factor of 10^4 or higher. Furthermore, if the Raman active molecule is located in hotspots between two plasmonic surfaces, the signal can be amplified by a factor up to 10^{15}.[91]

Measurement of Raman scattering of molecules interacting with plasmonic surfaces is considered a direct sensing approach. Indirect sensing approaches employ a Raman-active "probe" molecule which chemically reacts or interacts with the analyte of interest, and the probe is attached to the plasmonic surface. In this case, analyte-induced chemical changes of the probe molecule result in measurable Raman spectral changes for some or all of the vibrational modes. Unchanged vibrational modes may be utilized as internal references for ratiometric SERS signals, providing a robust analytical approach since it is not dependent upon the concentration and the inhomogeneity of plasmonic materials which otherwise cause a large variation of SERS intensity. The measurement of small analytes such as pH,[92-94] H_2O_2,[95] H_2S,[96] CO,[97] NO,[98] and formaldehyde[99] have been effectively demonstrated using such a ratiometric approach.

Phosphorescence lifetime measurement is another widespread spectroscopic technique in biosensing that is particularly attractive because it is not strongly affected

by photobleaching or intensity fluctuations in excitation source.[100] Similar to ratiometric SERS sensing, phosphorescence lifetime-based sensing is also largely independent of phosphor concentration and the spatial distribution of phosphor if a global average over the illuminated sample is the desired measurement.[101] Moreover, using time-domain methods, the relatively long lifetime phosphorescence lifetime signals (10s to 100s of microseconds) are readily separated from the rapidly-decaying autofluorescence background in biological samples (few nanoseconds).[102] Hence, oxygen-sensitive metalloporphyrin dyes have been successfully used to estimate dissolved oxygen in biological samples by monitoring the quenching of lifetime.[103-105] Phosphorescence lifetime- based sensing of temperature,[106] pH,[107] and CO_2[108] have also been reported.

While examples of individual and multianalyte sensors employing a single measurement mode abound, to our best knowledge a combination of ratiometric SERS and phosphorescence lifetime has not been previously discussed or demonstrated. Therefore, in this work, SERS and phosphorescence lifetime systems are merged to evaluate the potential for multimodal sensing from a single material. This was inspired by and leverages advances in separate recent work, wherein hydrogel materials endowed with either SERS or phosphorescence lifetime for sensing oxygen and pH, as well as glucose and lactate, have been reported.[109-112] These studies all employed polymeric microcapsules (MCs) that encapsulate the sensing chemistry, which were made by taking advantage of the well-established layer-by-layer (LbL) protocol.[113-114]

Here, we investigated the potential to create a single material with dual-mode transduction for SERS and phosphorescence using pH and oxygen as the measurands by

combining two different types of microdomain-bound transduction elements—those containing either pH-sensitive SERS reporters or oxygen-quenched phosphors—into the same hydrogel matrix (Figure 3-1).

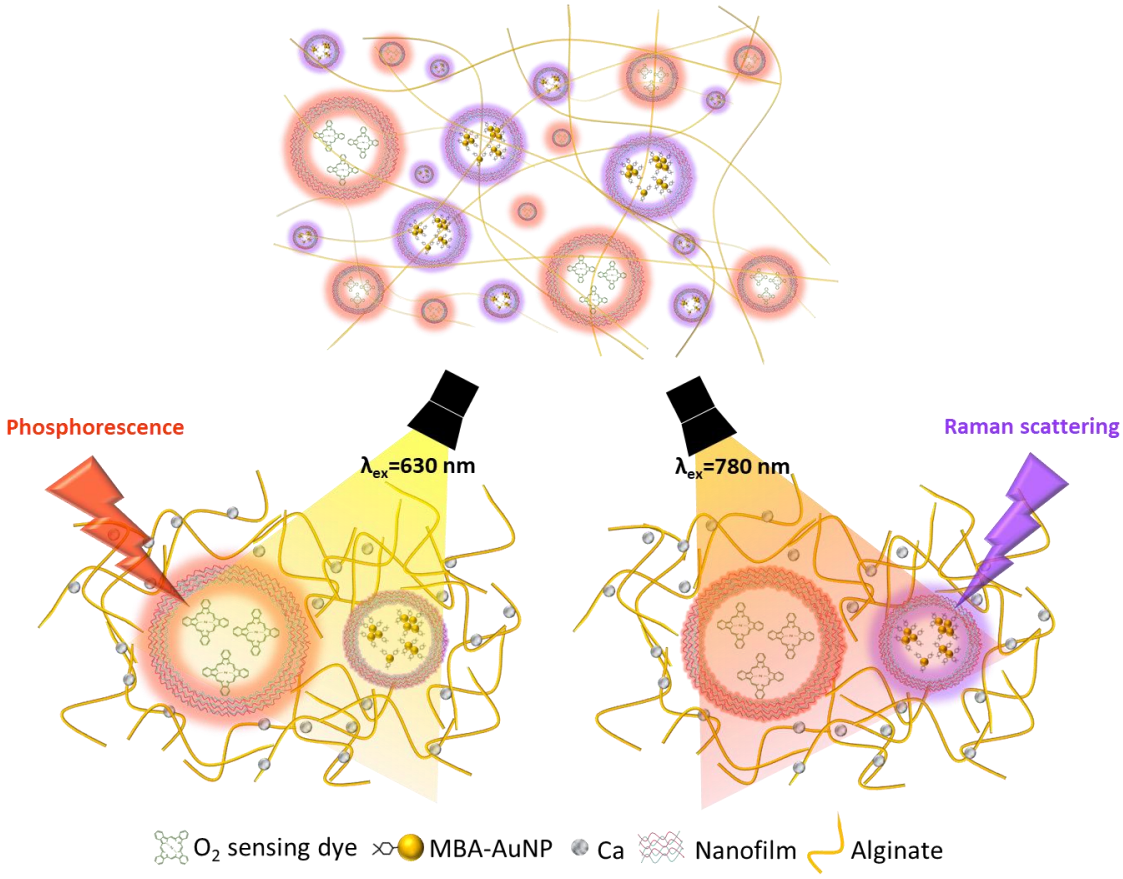

Figure 3-1. Illustration of hydrogel matrix with embedded microdomains (capsules) with random distribution. The capsules contain the chemical-optical transduction elements: oxygen-sensitive phosphors and pH-sensitive SERS reporters based on gold nanoparticles. The use of different light sources selectively induces emission from the different encapsulated components, whereas emission filters and time-gated detection enable further separation of signals.

The choice of analytes in this case is motivated by the biological importance[115] and relevance to assessing cell health[116-117] as well as the further capabilities when pH and oxygen sensing are combined with use of oxidoreductase enzymes whose byproducts are capable of changing surrounding pH, for instance, glucose oxidase (GOx) and lactate oxidase. Specifically, the enzymatic reaction of glucose catalyzed by GOx is described by the following chemical reaction:

$$Glucose + O_2 + H_2O \rightarrow Gluconic\ acid + H_2O_2$$

It is important to note that the redundant measurement of glucose can be accomplished through dual detection modes applied to monitor this single reaction. Specifically, under steady-state conditions with sufficient oxygen and glucose supply, local oxygen concentration is depleted in proportion to glucose concentration whereas gluconic acid is produced, yielding a lower surrounding pH.

3.2. **Experimental section**

3.2.1. **Chemicals**

Poly(diallyldimethylammonium chloride) (PDADMAC, average M_w 100-200 kDa), poly(sodium 4-styrenesulfonate) (PSS, average Mw 70 kDa), sodium carbonate, sodium bicarbonate, calcium carbonate, 4-mercaptobenzoic acid (MBA), sodium citrate tribasic dihydrate, gold chloride trihydrate, 2-(N-morpholino) ethanesulfonic acid sodium salt (MES), tris(hydroxymethyl)aminomethane hydrochloride (TRIS), alginic acid sodium salt (from brown algae, ~250 cps for 2 % solution at 25 ºC), dimethyl sulfoxide (DMSO), and 1-Ethyl-3-(3-dimethylaminopropyl)carbodiimide hydrochloride

(EDC) were obtained from Sigma (St. Louis, MO, USA). Calcium chloride and D-glucose anhydrous were purchased from Macron Fine Chemicals (Center Valley, PA, USA). Ethanol (200 proof), glucose oxidase (257 U/mg), Pd meso-tetra(sulfophenyl)tetrabenzoporphyrin ($PdPh_4(SO_3Na)_4TBP$), and sulfo N-hydroxysuccinimide (NHS) were obtained from Decon Labs (King of Prussia, PA, USA), BBI Solutions (Cardiff, UK), Frontier Scientific (Logan, UT, USA), and Thermo Fisher Scientific (Waltham, MA, USA), respectively.

3.2.2. **Synthesis of pH sensitive nanoparticles**

Citrate stabilized gold nanoparticles (Citrate-AuNPs, 0.35 nM) were prepared by a seed-mediated synthesis method.[109] To build a SERS based pH probe the surface of gold nanoparticles was modified with a pH-sensitive Raman dye (MBA). 1 mL of gold nanoparticle solution was placed in a 2 mL-centrifuge tube. 1 mM ethanolic MBA solution (200 µL) was quickly added into the centrifuge tube. The mixture was vortexed for 5 min and then centrifuged at 2000 g for 5 min. To eliminate excess unreacted MBA molecules, remaining surface modified nanoparticles were washed with 1 mL of ethanol. The washed MBA capped AuNPs (MBA-AuNPs) were resuspended in 200 µL of DI water.

3.2.3. **Encapsulation of sensing probes in microcapsules**

A co-precipitation method was used to entrap the pH sensing nanoparticles in $CaCO_3$ microparticles (MPs). 400 µL of MBA-AuNPs was mixed with 8 mL of 0.25 M

Na_2CO_3 in a 20 mL beaker. To this mixture, 8 mL of 0.25 M $CaCl_2$ was quickly injected under vigorous stirring. After the mixture was stirred for an additional 30 sec, precipitated $CaCO_3$ MPs were sedimented within 10 min. The sedimented $CaCO_3$ MPs were washed with 5 mM sodium bicarbonate buffer at pH 8.0. To form polyelectrolyte multilayers (PEMs) on the $CaCO_3$ MPs, the washed $CaCO_3$ MPs were redispersed in 1 mL of the buffer used for the washing step and then were sequentially exposed to PDADMAC and PSS solutions (20 mg/mL) prepared with 5 mM sodium bicaronate buffer (pH 8.00). Between each layer-deposition step, excess polyelectrolyte was removed by rinsing with 1 mL of 5 mM sodium bicarbonate buffer at pH 8.00. After 10 bilayers of (PDMAC/PSS) were deposited, 3.3 mg of PEM coated $CaCO_3$ MPs (PEM MPs) was mixed with 15 mL of 0.2 M MES buffer at pH 6.20. The mixture was incubated for 15 min with gentle nutation. This step was repeated two more times for complete $CaCO_3$ core dissolution. The resulting hollow PEM microcapsules (MCs) were suspended in 100 µL of DI. The oxygen sensing probe (400 µL of 10 mM $PdPh_4(SO_3Na)_4TBP$ solution with DMSO) was also encapsulated in PEM MCs following the same protocol described above.

3.2.4. **Microporous alginate composite (MPAC) synthesis**

MPAC hydrogels were constructed via the protocol developed by Roberts *et al.* was adopted.[118] In the cases of pH sensing hydrogel or oxygen sensing hydrogel, 100 µL of PEM MCs encapsulating a sensing chemistry was added to a mixture of 3 w/v% aqueous alginate (250 µL) and 25 µL of $CaCO_3$ solution (41.6 mg/mL). The resultant

solution was completely mixed with 0.5 M MES at pH 5.80 (125 µL). The mixture was poured into a U-shaped casting mold made of a 0.03 inch Teflon spacer sandwiched between two microscope slides as depicted in Figure 3-2. The slab of hydrogel was removed from the casting mold and then stored at room temperature in 10 mM MES buffer solution (pH 7.00) containing 10 mM $CaCl_2$.

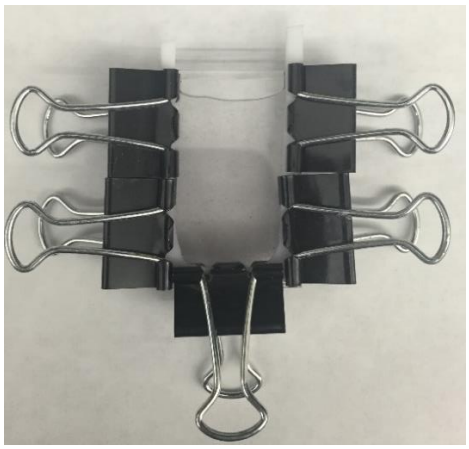

Figure 3-2. Alginate hydrogel mold consisting of a Teflon spacer compressed two glass slides.

For dual modality sensing hydrogels, the pH sensing microdomain and oxygen sensing microdomain were embedded in the same alginate hydrogel matrix. The only fabrication difference for such hydrogel was the preparation of PEM MC solution. Initially, 100 µL of pH sensing probe in embedded PEM MCs were mixed with 100 µL of oxygen sensing probe contained in PEM MCs. The mixture was centrifuged at 3500 g for 2 min. Sedimented PEM MCs in the bottom of the centrifuge tube were redispersed

in 100 µL of DI. The resultant PEM MC solution was used to fabricate the MPAC structure following the above-mentioned protocol.

Glucose sensing hydrogels were fabricated to demonstrate glucose sensing with two different optical modalities. In this case, GOx was chemically conjugated to the alginate matrix. Briefly, 10 mg of GOx was dissolved in 250 µL of alginate precursor solution by nutation at 4 ˚C overnight. The prepared alginate solution with GOx was used to construct hydrogel sensors with the same method used for the dual modality sensing hydrogel. After the hydrogel was removed from the casting mold, it was incubated in the same storage buffer solution (45 mL) containing EDC (14 mg) and NHS (40 mg) overnight to conjugate GOx to the carboxyl group in the alginate matrix. After the conjugation process, the hydrogel was washed 3 times with the storage buffer solution to remove unreacted EDC and NHS as well as reaction byproducts.

It was hypothesized that the spatial separation of sensing elements by isolating them within microdomains would minimize chemical and spectral crosstalk between the elements for generating Raman scattering and phosphorescence lifetime. To test this hypothesis, negative controls *(*hydrogels containing only SERS pH sensing units and others that containing only oxygen sensing units) were also fabricated and their sensitivities were evaluated for comparison. To further show the concept of redundant glucose sensing via dual optical modalities, glucose oxidase was chemically crosslinked into the matrix of hydrogel. The response of this hydrogel to glucose was not only tested but also the reversibility of each optical mode.

3.2.5. **Transmission electron microscopy (TEM)**

2 µL of stock solution (citrate-AuNPs or MBA-AuNPs) was diluted 50-fold using DI water. After 10 min of sonication, the diluted solution (5 µL) was placed onto a 300 square mesh Cu grid coated with C film (CF-300 Cu, Electron Microscopy Sciences, Hatfield, PA, USA). The sample loaded Cu grid was then dried overnight in a desiccator. A TEM equipped with a cold field emission gun (HF3300, Hitachi Scientific Instruments, Tokyo, Japan) was utilized to characterize AuNPs with an operation voltage of 30 kV.

3.2.6. **Zeta potential**

Zeta potential measurements were obtained using a ZetaSizer Nano Zen 3600 (Malvern Instruments Ltd, Malvern, UK). AuNP solutions were diluted with DI water by a factor of ten and then transferred to electrophoresis capillary cells (DTS 1070, Malvern Instruments Ltd, Malvern, UK) for measurements.

3.2.7. **Scanning electron microscopy (SEM) and energy dispersive X-ray spectroscopy (EDS)**

Diluted PEM MP stock solutions (by a factor of 20) or diluted PEM MC stock solutions (by a factor of 50) were dropped directly onto n-type Si wafers, whereas pieces of MPAC hydrogels were placed on a carbon tape layer attached on an n-type Si wafer. Specimens were air dried for 24 hrs and then sputter coated with 2.5 nm thick Pt/Pd alloy thin films to avoid charging under SEM operation. The backscattered electron

(BSE) images of PEM MPs, PEM MCs, and MPACs were then recorded by a field emission SEM (JSM-7500F, JEOL, Tokyo, Japan) combined with an EDS analyzer (Oxford instruments, Abingdon, UK). The working distance and acceleration voltage during the SEM operation were fixed at 8 mm and 15 kV, respectively. All EDS spectra were acquired under BSE imaging mode.

3.2.8. **X-ray diffraction (XRD)**

Vacuum dried PEM coated MPs were examined by a powder X-ray diffraction technique using Cu $K_{\alpha}1$ radiation (1.54 Å). 40 kV was applied to an X-ray tube yielding an operating current of 20 mA. X-ray intensity was recorded as a function of 2-theta (from 20 to 40 °) using a position sensitive X-ray detector (LynxEye, Bruker AXS, Karlsruhe, Germany).

3.2.9. **Instrumental neutron activation analysis (INAA)**

INAA was utilized to quantify the weight of Au in the pH sensing probe containing PEM MPs. Three replicates of PEM MPs (10 mg) were prepared by vacuum drying and were then placed in irradiation vials. As a standard material, Au plasma standard solution (Specpure, Alfa Aesar, Heysham, UK) was placed onto high purity cellulose powder in the irradiation vials followed by heat lamp drying. The samples and Au standards were sequentially exposed to a thermal neutron flux at 9.1×10^{12} neutrons/cm^2·s using the TEES Nuclear Science Center's 1 MW TRIGA reactor at Texas A&M University. Emitted gamma rays from the samples were counted by a high-

purity Ge (HPGe) detector (Ortec, Oak Ridge, TN, USA). Recorded gamma ray spectra were analyzed with the NAA software from Canberra Industries (Meriden, CT, USA). 3 aliquots of oxygen probe embedded PEM MPs (20 mg) were also examined with the same INAA method to estimate the weight fraction of Pd in the particles. In this case a Pd standard (CPI International, Santa Rosa, CA, USA) was used as a calibrator.

3.2.10. **Confocal microscopy**

Differential interference contrast (DIC) and confocal fluorescence microscopy images of oxygen sensing hydrogel were collected using an inverted confocal microscope (IX81, Olympus, Tokyo, Japan) combined with a spinning disk scanning unit (CSU-X1, Yokogawa, Tokyo, Japan). A 445 nm laser was used to excite MCs containing $PdPh_4(SO_3Na)_4TBP$ via a 40× oil immersion objective lens (NA=1.3).

3.2.11. **Hyperspectral dark field imaging**

A slab of dual modality sensing hydrogel (t = 0.01 inch) was placed on a glass slide. After 50 µL of 10 mM MES buffer with 10 mM $CaCl_2$ (at pH 7.00) was added on top of the hydrogel slab, the hydrogel was covered with a cover glass. The wet hydrogel slab was characterized using an enhanced dark field illumination optical system (CytoViva, Auburn, AL, USA) equipped with a commercial microscope (BX51, Olympus, Tokyo, Japan) and a full spectrum aluminum halogen lamp. A dark field image was captured using an oblique angle illumination method. The reflectance spectra of two different sensing chemistry materials (MBA-AuNPs and $PdPh_4(SO_3Na)_4TBP$)

were collected in the wavelength range between 430 to 830 nm with 2 nm resolution. Spectral angle mapping (SAM) was also performed to trace the location of each sensing chemistry material in the dark field image by comparing the reflectance spectrum of each pixel in the image with the measured spectrum of the material of interest.

3.2.12. **Raman measurement**

A bench top Raman system (DXR, Thermo Fisher Scientific, Waltham, MA, USA) was used to record SERS spectra. SERS active samples were excited with a 20 mW, 780 nm, laser using a 10× objective lens (NA=0.25). For MBA-AuNPs and MCs dispersed in solution, the laser was focused on the solution surface. For pH, dual modality, and glucose sensing hydrogels, the laser was focused on top of the hydrogel placed in the buffer. SERS spectra were collected for 3 sec and for each sample five spectra were averaged. Raman background signal was eliminated from each averaged spectrum using Crystal Sleuth.[119]

To evaluate the pH with SERS, MBA-AuNPs, MCs containing the pH sensing probe, pH sensing hydrogel discs, and dual modality sensing hydrogel discs (D=2 mm) were exposed to different pH conditions (pH 4.00, 5.50, 6.00, 6.50, 7.00, and 8.50). The MBA-AuNPs and the MCs were dispersed in 30 µL of 10 mM MES buffer solutions whereas the hydrogel discs were incubated in 300 µL of the same buffer solution containing 10 mM $CaCl_2$. After 30 min of incubation, the MBA-AuNPs and the MCs were directly injected into the wells of a 384-well plate. The hydrogel discs were delivered into the wells followed by the addition of the same buffer over the discs.

pH sensing hydrogel discs were also sequentially exposed to two extreme pH conditions to test the reversibility of pH sensing. Initially, SERS spectra of the hydrogel disc at pH 8.50 were collected following the protocol described above. After the SERS measurement at pH 8.50, the discs were removed from the wells and washed three times with the same type of buffer at pH 4.00. The washed discs were dipped in 300 μL of the same buffer solution for 30 min. The discs were placed into new wells of the 384 well plate with the same buffer at pH 4.00 (30 μL). This half cycle of reversibility test was repeated 10 times (total 5 cycles).

Similarly, reversible glucose sensing was tested by exposing glucose sensing hydrogel discs alternatively to two extreme glucose concentrations (0 and 400 mg/dL). Briefly, the discs were dipped in 300 μL of 1mM Tris buffer with 10 mM $CaCl_2$ at pH 7.00 for 30 min.

3.2.13. **Phosphorescence lifetime measurement**

Discs of hydrogel sensors (D=4 mm; t=0.03 inch) were inserted in a custom designed flow-through cell to evaluate their optical responses to oxygen.[120] The hydrogel discs were exposed to five different dissolved oxygen concentrations (0, 25.9, 51.7, 103.4, and 206.8 μM) at 37 ˚C. Each dissolved oxygen concentration of 10 mM Tris buffer containing 10 mM $CaCl_2$ at pH 7.00 was achieved by purging the mixture of nitrogen gas and air using a mass flow controller (1179A Mass-Flo, MKS Instruments, Andover, MA, USA). For glucose sensing, 0 and 400 mg/dL glucose solutions were prepared with 1 mM Tris buffer (pH 7.00) containing 10 mM $CaCl_2$. Glucose solutions

were pumped through the flow cell which contained the discs of glucose sensing hydrogel at a fixed dissolved oxygen concentration (206.8 μM). All samples were excited by a 630 nm LED and resultant optical signals were recorded with a lab-built time domain phosphorescence lifetime measurement system.[100]

3.3. **Results and discussion**

3.3.1. **Characterization of MBA-AuNPs**

Changes in nanoparticle size and aggregation state due to the surface modification with MBA were evaluated by TEM. Figure 3-3A depicts AuNP size distribution obtained from 309 particles in TEM images indicating the monodispersity of AuNPs. The mean diameter (43.9 ± 4.1nm) calculated from the TEM results is about 10% smaller than the diameter estimated from reported data estimated by the UV-Vis technique.[109] In addition to size determination, TEM is used to visualize the difference in particle dispersion before and after MBA capping. TEM images (Figures 3-3B and C) revealed that citrate-AuNPs are highly dispersed, whereas MBA-AuNPs (Figures 3-3D and E) exhibit dimers, trimers or larger aggregates. The colloidal stability of MBA-AuNPs was also evaluated with zeta potential. As shown in Figure 3-4, the absolute Zeta potential of nanoparticles increased from -36.5 to -46.2 mV upon MBA coating. Such increase in surface charge after MBA capping enabled nanoaggregates to retain colloidal stability even after centrifugation.

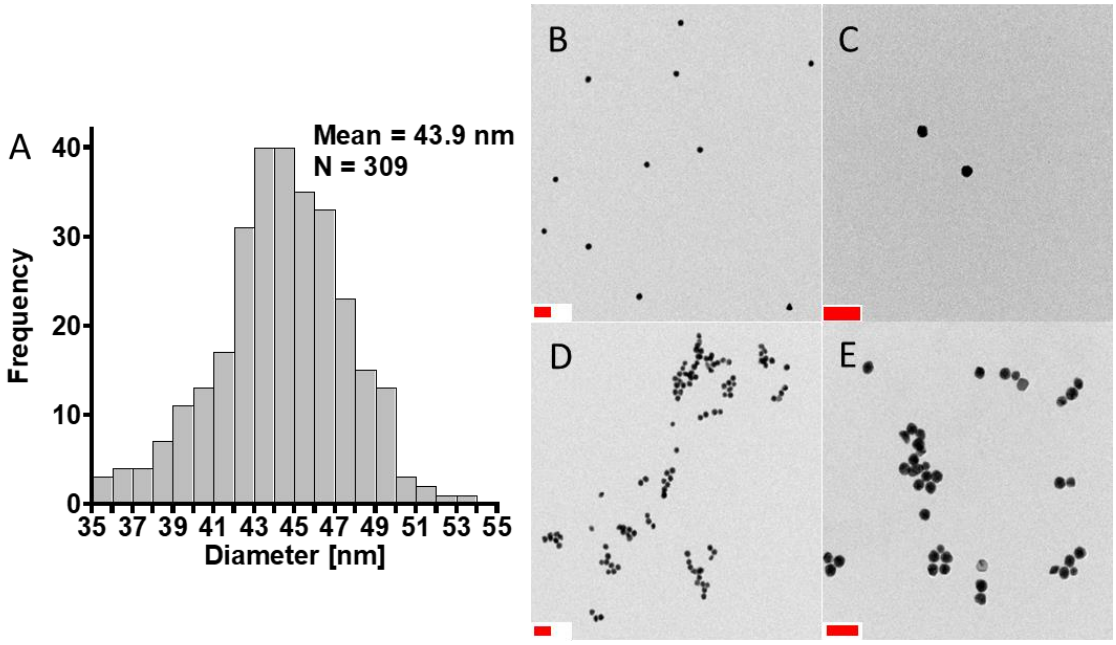

Figure 3-3. Size distribution of AuNPs calculated from TEM data (A) and TEM images of citric acid-AuNPs (B, C) and MBA-AuNPs (D, E). Scale bars represent 100 nm.

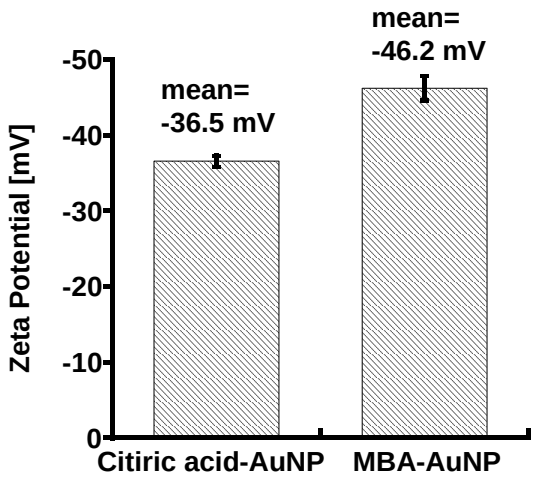

Figure 3-4. Zeta potentials of citric acid-AuNPs and MBA-AuNPs (Error bars represent one standard deviation calculated from 3 different aliquots).

3.3.2. **Physical characterization of sensing chemistry embedded microparticles, microcapsules, and hydrogels**

The pH probe containing PEM MPs, PEM MCs, and MPAC hydrogels were examined with SEM and EDS to determine AuNP loading and the formation of desired structures. In Figure 3-5A the backscattered electron (BSE) image of PEM MPs containing pH sensing probe displays spherical morphology with rough surfaces. Analysis of 77 PEM MPs from multiple SEM images gives an average diameter of 4.40 ± 0.39 μm. The spherical structure of $CaCO_3$ implies that the MPs consist of mainly hexagonal crystals of vaterite, which is easily dissolved by etchant and therefore desired for the MC formation step.[121] Apart from topographical information, the BSE mode of the SEM also provides compositional contrast to validate effective confinement of MBA-AuNP in the PEM MPs. Contrast differences were distinguished in BSE images of the PEM MPs (Figure 3-5A). The background appears uniform suggesting evenly sputtered Pt/Pd thin nanofilms deposited on the surface of the PEM MPs. Contrasting bright spots localized in the PEM MPs correspond to Au, as confirmed by Au footprints obtained from EDS spectra. These bright spots therefore correspond to the entrapment of MBA-AuNP in the PEM MPs (Figure 3-6A). The spectra (Figure 3-6A and B) also identified $CaCO_3$ (Ca/C/O), the sputtered thin film (Pt/Pd), the sample substrate (Si), and PSS (S). The BSE image of a PEM MC (Figure 2B) substantiated that 0.2 M MES buffer at pH 6.2 completely dissolved the $CaCO_3$ core resulting in hollow structures of MC. The MC showed a collapsed feature attributed to SEM sample preparation. The brighter spots in the BSE image indicated the location of MBA-AuNP in the PEM MC. EDS data

(Figures 3-6C and D) confirmed that the $CaCO_3$ core was completely dissolved and that MBA-AuNPs were retained within the MC. As illustrated in Figure 3-5C and D, PEM MC embedded alginate hydrogel showed microporous morphology on the wrinkled surface due to dehydration.[118, 120] The lack of bright spots in the alginate matrix and their apparent confinement to PEMs demonstrated effective spatial localization, eliminating SERS signals originating from interactions between MBA molecules and the alginate monomers.

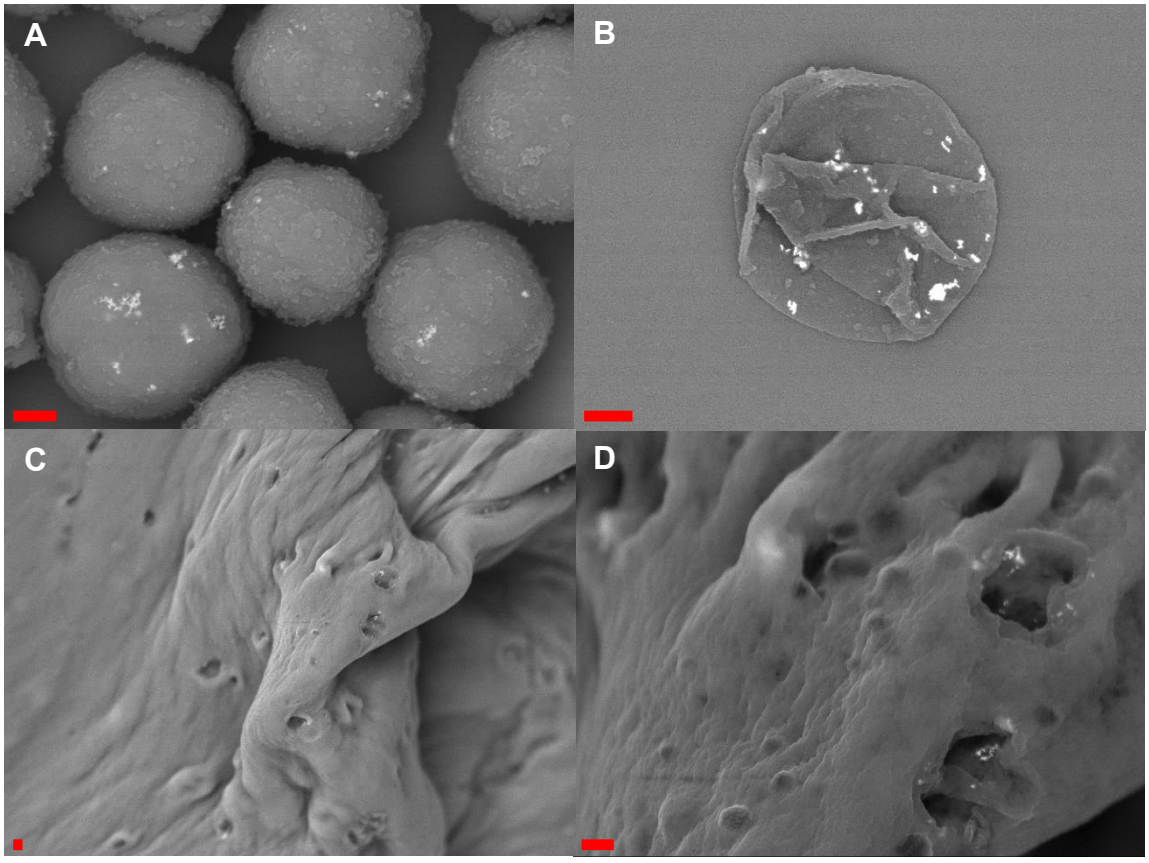

Figure 3-5. Size distribution of AuNPs calculated from TEM data (A) and TEM images of citric acid-AuNPs (B, C) and MBA-AuNPs (D, E). Scale bars represent 100 nm.

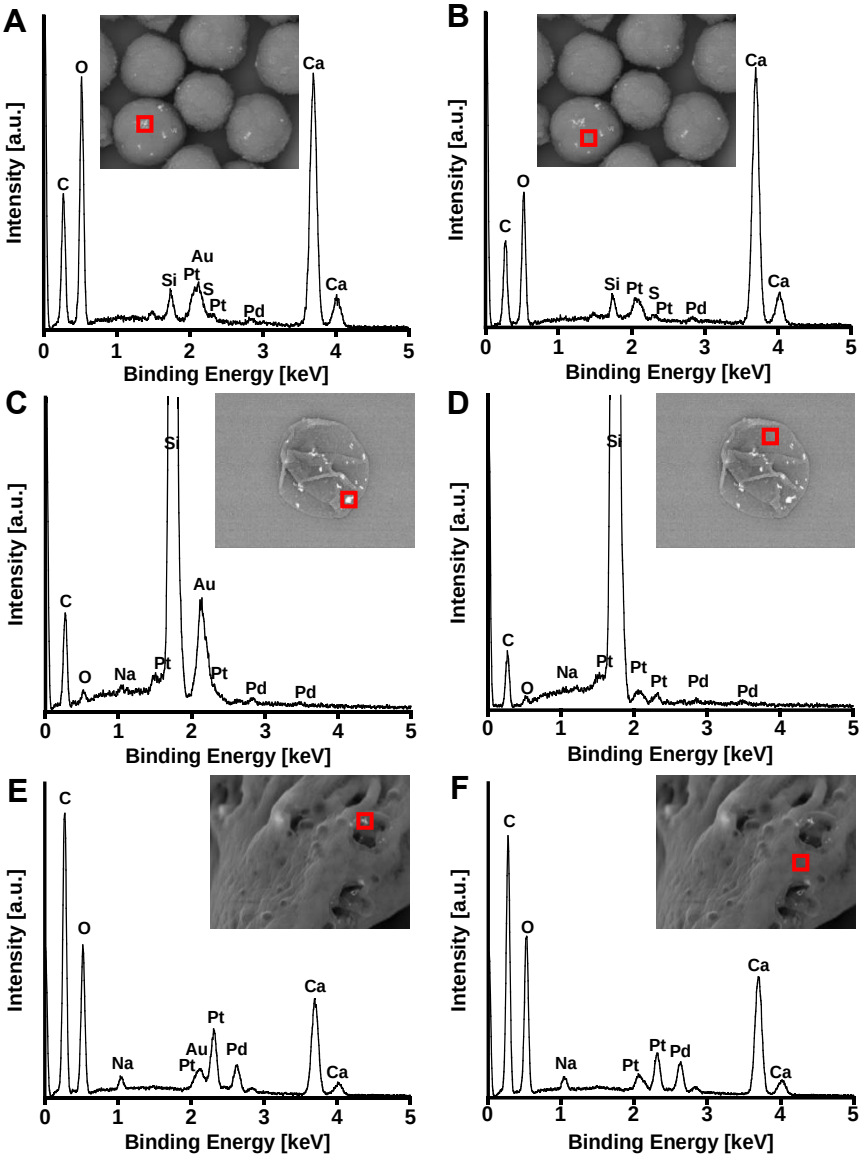

Figure 3-6. EDS spectra of a PEM MP (A: bright spot, B: dark spot), a hollow microcapsule composed of 10 bilayers of PDADMAC/PSS (C: bright spot, D: dark spot) and MPAC (E: bright spot in a MC, F: dark spot in a MC); Insets are BSE images where EDS spectra were collected in the boxed regions.

Similarly, the oxygen probe encapsulating PEM MPs, MC, and MPAC hydrogel were investigated by SEM and confocal microscopy. As shown in Figure 3-7A, spherical MPs with fuzzy surface were also formed after the co-precipitation process. The average diameter of the PEM MPs was calculated as 4.62 ± 0.42 μm from multiple SEM images. BSE images of MC and MPAC hydrogel (Figure 3-7B-D) revealed successful formations of hollow MC and microporous hydrogel as intended. Unlike the case of MBA-AuNP embedded specimens, the BSE images of $PdPh_4(SO_3Na)_4TBP$ containing samples did not show any significantly bright regimes due to the presence of Pd. Furthermore, EDS could not confirm the characteristic X-ray peak of Pd (Data not shown). Assuming the amount of Pd in the specimens was lower than the detection limit using EDS, confocal microscopy was applied to further verify the localization of oxygen sensing dyes in PEM MCs. A DIC image of the oxygen probe containing MPAC hydrogel (Figure 3-8A) showed a uniform distribution of MCs in the wet alginate matrix. In addition, a fluorescence image in Figure 3-8B revealed the successful confinement of phosphorescence dye, $PdPh_4(SO_3Na)_4TBP$, within PEM nanofilm microdomains as previously reported with RITC-BSA[118] and PdTCPP.[111-112, 120]

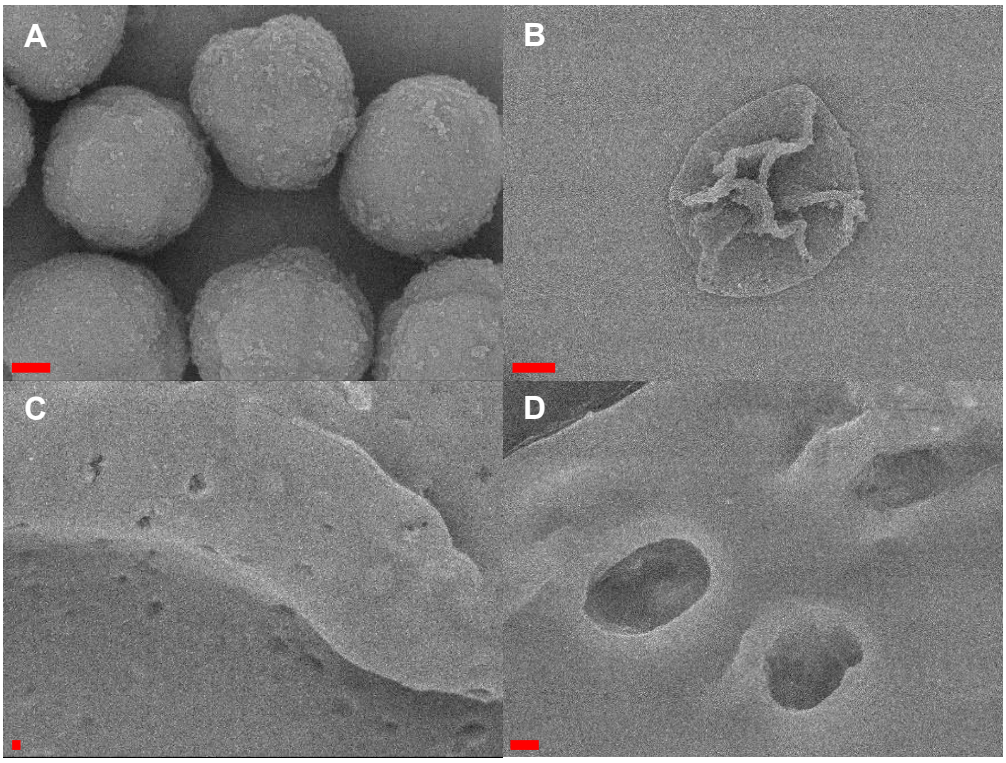

Figure 3-7. BSE images of PEM MPs (A), PEM MC (B), and MPAC hydrogel (C and D) all containing $PdPh_4(SO_3Na)_4TBP$. Scale bars represent 1 µm.

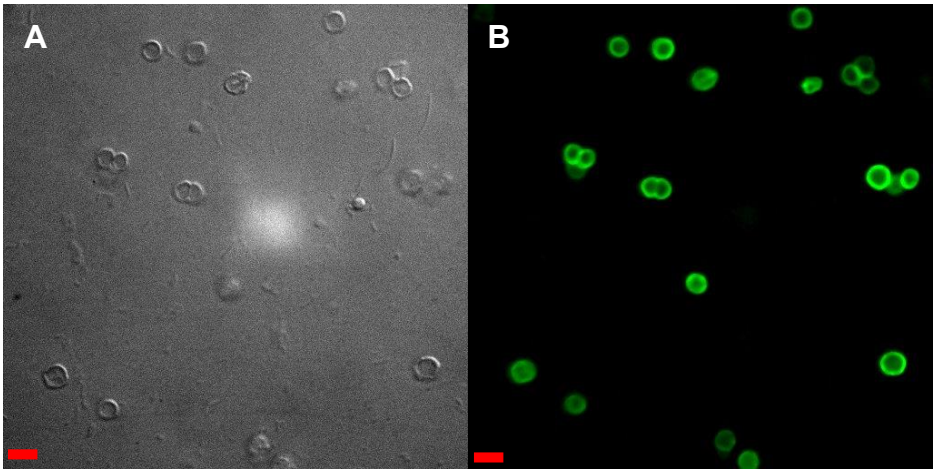

Figure 3-8. DIC (A) and fluorescence (B) images of $PdPh_4(SO_3Na)_4TBP$ containing MPAC hydrogel. Scale bars represent 5 µm.

For dual modal sensing hydrogel, darkfield microscopy equipped with hyperspectral mapping function was used for characterization to simultaneously visualize the presence of the pH sensing probe and the oxygen sensing probe. Figure 3-9A-B illustrates that two different types of MCs are dispersed throughout the crosslinked alginate matrix: MCs filled with green dots and separate microdomains filled with golden dots. To verify the origins of different colors, reflectance spectra were recorded from each color regime, as shown in Figure 3-9C. The spectrum collected from green regimes in Figure 3-9A revealed two distinct reflectance minima matching the Soret and Q bands of $PdPh_4(SO_3Na)_4TBP$.[122] On the other hand, the spectrum obtained from the golden regimes in the same image showed a surface plasmon resonance (SPR) band of AuNP at approximately 800 nm. This observed SPR peak wavelength is longer than what Mortimer *et al.* observed with 20 nm AuNP.[123] The redshift of the SPR for MBA-AuNP can be attributed to larger NPs (43.9 nm) and the formation of aggregation.[124] The SAM image (Figure 3-9B) revealed that $PdPh_4(SO_3Na)_4TBP$ and MBA-AuNP are spatially localized in discrete microdomains.

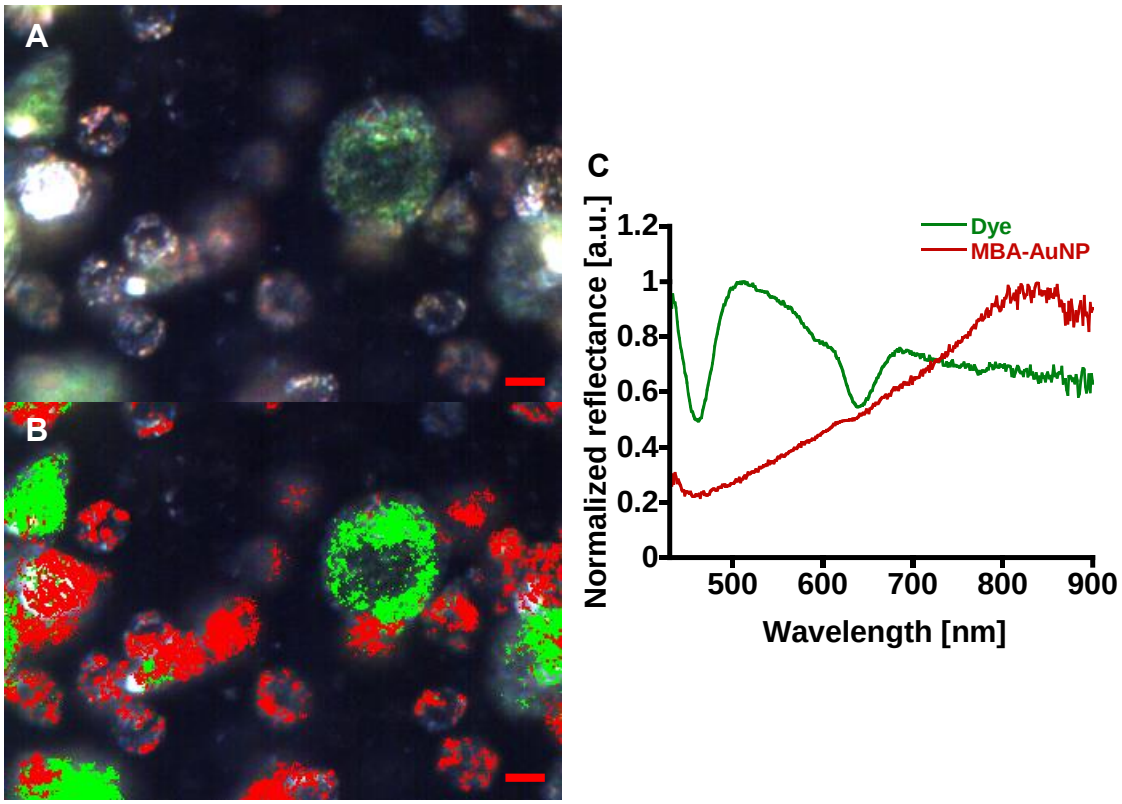

Figure 3-9. Darkfield image of dual modal sensing hydrogel (A), reflectance spectra of oxygen sensitive dye and MBA-AuNP (B), and SAM image of the same hydrogel. Scale bars represent 5 μm.

3.3.3. **Quantitative analysis of sensing chemistry encapsulation**

To evaluate the number of AuNPs, the mass of a PEM MP containing MBA-AuNP was calculated ignoring the weights of MBA-AuNPs and PEM nanofilms. The mass of the MP can be derived as

$$M_{MP} = V_{MP} \times \rho_{MP}$$

where M_{MP}, V_{MP} and ρ_{MP} represent the mass of the MP, the volume of the MP and the density of the MP, respectively. The volume of the MP (V_{MP}) was estimated as 4.46 ×

10^{-11} cm^3 from the diameter of the MP (4.40 μm) measured by SEM assuming spherical MPs. The MP density (ρ_{MP}) can be estimated using the equation

$$\rho_{MP} = \frac{m_V + m_C}{\frac{m_V}{\rho_V} + \frac{m_C}{\rho_C}}$$

where m_V and m_C are the weight fractions of vaterite and calcite, respectively; ρ_V (2.65 g/cm^3) and ρ_C (2.71 g/cm^3) are defined as the densities of vaterite and calcite, respectively. The weight fractions of vaterite and calcite were calculated as 90.2 and 9.8 wt%, respectively, from XRD data of the MPs (Figure 3-10A) using the Rao's equation.[125] Therefore, the density of the MP (ρ_{MP}) was determined as 2.65 g/cm^3. From the calculated V_{MP} and ρ_{MP} the weight of a PEM MP containing MBA-AuNP was estimated as 1.17×10^{-10} g. The number of AuNPs in a PEM MC (N_{AuNP}) is described as

$$N_{AuNP} = \frac{M_{MP} m_{Au}}{M_{AuNP}}$$

where m_{Au} and M_{AuNP} are the weight fraction of gold PEM MCs containing MBA-AuNPs and the mass of a gold nanoparticle (8.55×10^{-16} g), respectively. INAA confirmed m_{Au} was 0.993 wt%. Consequently, the number of MBA-AuNPs in a PEM MC and encapsulation efficiency were calculated as 1373 per PEM MC and 46.0 %, respectively.

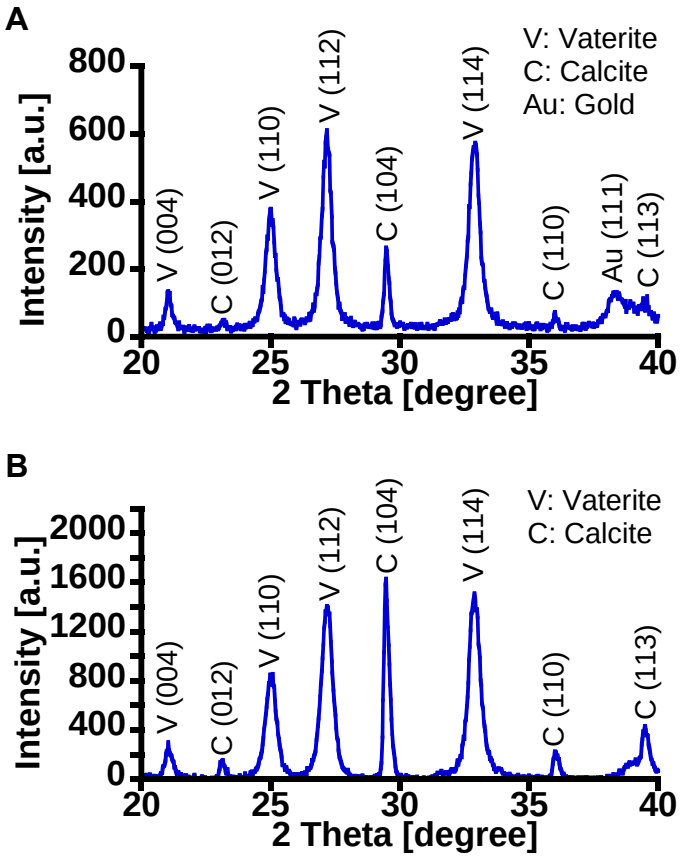

Figure 3-10. XRD data of PEM MPs containing MBA-AuNPs (A) and PEM MPs containing $PdPh_4(SO_3Na)_4TBP$.

The number of $PdPh_4(SO_3Na)_4TBP$ in a PEM MC and its encapsulation efficiency were also estimated similarly with the method described above. According to the MP diameter (4.62 µm) obtained from SEM images, V_{MP} was calculated as 5.16×10^{-11} cm^3. Based on XRD data (Figure 3-10B) m_V and m_C were determined as 78.0 and 22.0 wt%, respectively, resulting in a MP density (ρ_{MP}) of 2.66 g/cm^3. Therefore, the weight of a PEM MP containing oxygen sensitive dye (M_{MP}) was found to be 1.37×10^{-10} g. Since each oxygen sensitive dye molecule possesses only one Pd atom in its

chemical structure, the number of oxygen dye molecules in a PEM MC is equal to the number of Pd atoms per PEM MC. The number of $PdPh_4(SO_3Na)_4TBP$ molecules in a PEM MC (N_{Dye}) can be expressed as

$$N_{Dye} = \frac{M_{MP} m_{Pd}}{M_{Pd}}$$

where m_{Pd} and M_{Pd} represent the weight fraction of Pd in PEM MPs and atomic mass of Pd (1.77×10^{-22} g), respectively. m_{Pd} was estimated as 0.031 wt% from INAA results. It followed that a PEM MC contained 2.40×10^8 $PdPh_4(SO_3Na)_4TBP$ molecules and that the process yielded 24.9 % of encapsulation efficiency.

3.3.4. **SERS based pH sensing of pH probe in free solution, microcapsules, and hydrogels**

The SERS spectral changes of the MBA-AuNP in each of the distinct phases was investigated: aggregates suspended in solution, within PEM MCs, and finally within MPAC hydrogels. As MBA-AuNP was encapsulated within more complex structures, the raw spectrum of MBA had a higher baseline due to increased scattering as shown in Figure 3-11. Regardless of the environmental complexity of the SERS substrates, all SERS spectra exhibited significant Raman fingerprints for the attached MBA molecule (Figure 3-12). To evaluate spectral changes due to the different form factors, the peak frequencies of MBA Raman bands were calculated and compared (See Table 3-1). Having a spectral resolution of 3 cm^{-1}, no significant band shift was observed except in the COO^- stretching mode. The COO^- stretching mode peaks of MBA-AuNP in PEM MCs and in MPAC hydrogels were blue-shifted by 6 and 8 cm^{-1}, respectively, relative to

that of free MBA-AuNP in solution. Such blue-shifts may be due to Ca^{2+} ion-carboxyl group incorporation during the $CaCO_3$ dissolution step. The largest peak shift at the COO^- stretching mode of MPAC can be attributed to the presence of 10 mM $CaCl_2$ in buffer.

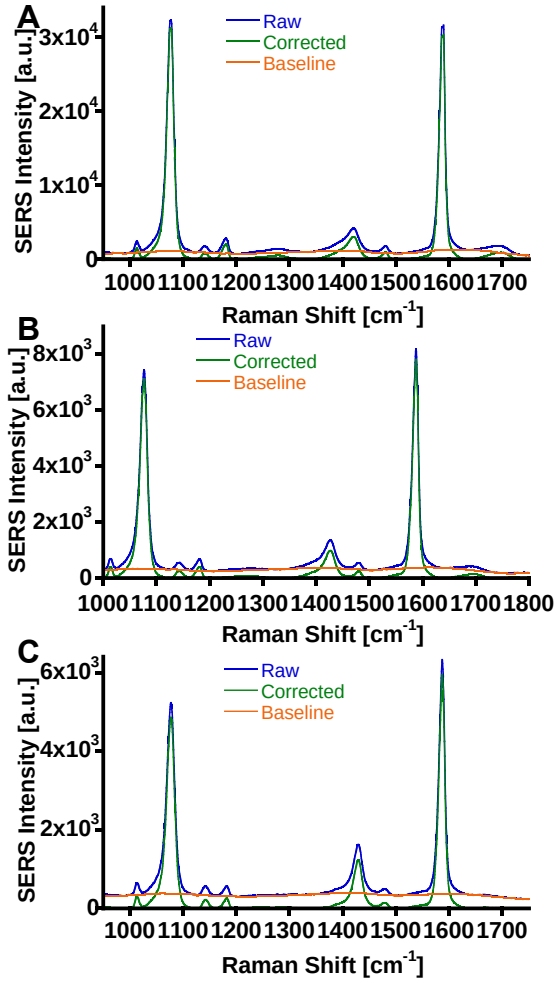

Figure 3-11. Raw, baseline and corrected spectra of MBA-AuNP (A) in free solution (B) in MCs and (C) in MPACs. All specimens were prepared with buffer solutions at pH 7.00.

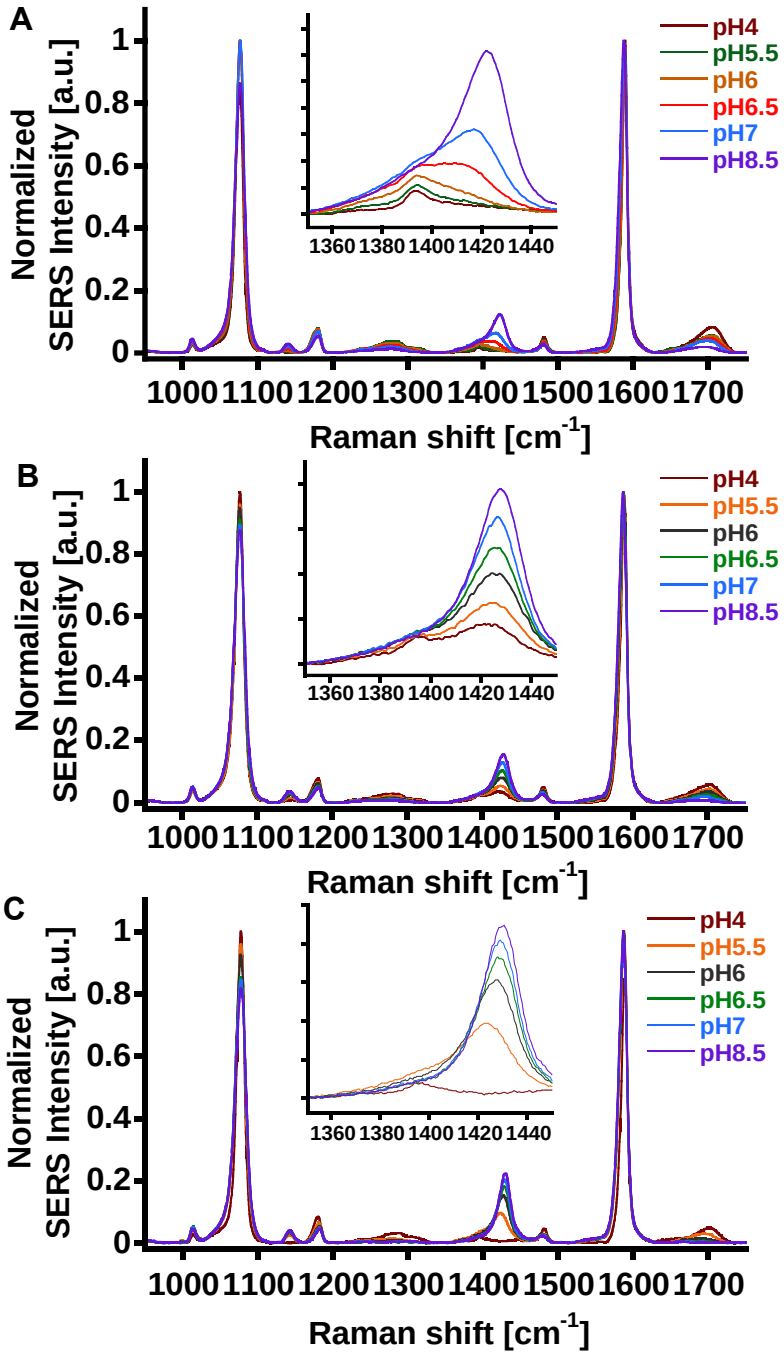

Figure 3-12. pH dependent SERS spectra of (A) MBA-AuNP, (B) PEM MCs containing MBA-AuNPs, and MPAC hydrogel containing MBA-AuNPs. Insets are magnified spectra around COO^- stretching band.

Table 3-1. Modes, average diameters, and stock concentrations of citric acid-AuNPs and MBA-AuNPs determined by NTA

MBA-AuNP ***[cm^{-1}]***	***MC*** ***[cm^{-1}]***	***MPAC*** ***[cm^{-1}]***	***Peak assignment***
1013	1013	1013	ring deformation
1077	1077	1078	ring breathing
1140	1142	1143	$CCOO^-$ stretching
1180	1181	1182	C-H in plane bending
1422	1428	1430	COO^- stretching
1481	1481	1481	C-H in plane bending
1587	1588	1587	axial deformation
1705	1702	1702	C=O stretching

To prove this postulation, the SERS peak shift of the carboxyl group related Raman band was monitored after adding different concentrations of $CaCl_2$ (1, 10, and 100 mM) to MBA-AuNPs suspended in 10 mM MES buffer (pH 7.00). For the cases of 1 mM and 10 mM $CaCl_2$ additions, COO^- peak was shifted to the higher frequency by 5 cm^{-1} (See Figure 3-13). The presence of 100 mM $CaCl_2$ resulted in 6 cm^{-1} blue-shift. Sun *et al*. reported a similar blue-shift after they added 10 mM Ca^{2+} into the MBA coated 3D-nanostructured Au array substrate incubated in DI water at pH 7.00.[126] Unlike their results, we observed an intensity increase of the COO^- stretching mode upon the addition

of Ca^{2+}. This opposite trend can be explained by the presence of buffer salt. The MES salt which has a high ionic strength reduces the electric double layer thickness on the AuNP surface. Owing to the thinner electric double layer, more Ca^{2+} ions can interact with COO^- groups resulting in an intensity increase of the COO^- stretching mode.

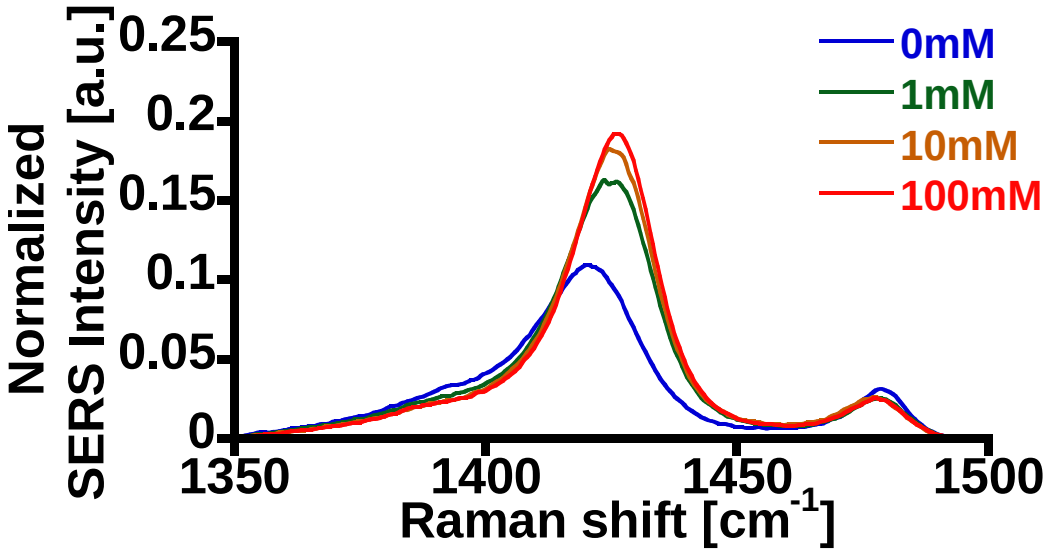

Figure 3-13. The spectral changes of COO^- stretching Raman band due to different $CaCl_2$ concentrations (0, 1, 10, 100 mM). All spectra were normalized to the intensity of axial deformation Raman band.

The response of MBA-AuNP in different form factors to varying pH were also evaluated by monitoring the SERS intensity of COO^- stretching mode relative to the axial deformation mode ($I(COO^-)/I$(axial deformation)). SERS data of five pH-sensitive samples collected from three different batches (n=3) were used to build a pH calibration

curve (See Figure 3-14A). The 3 σ method was used to calculate sensor parameters, which were summarized in Table 3-2.[109] There was no noticeable change of analytical ranges due to different form factors. Nonetheless, analytical range and pKa were shifted toward the more acidic range as environmental complexity of MBA-AuNP increased. These shifts are related to strong interaction between COO^- group of MBA and Ca^{2+} ion, which is conducive to the deprotonation of MBA carboxyl group. The pH sensitivity of MBA-AuNP was increased by approximately 11 and 72 %, as such nanoparticle was encapsulated in MCs and MPAC hydrogels, respectively. With no significant value change in analytic range due to structural complexity, such sensitivity increases can be attributed to the elevation of COO^- stretching mode intensity by Ca^{2+} ion-carboxyl group incorporation. In addition, the reversibility of pH sensing with MPAC hydrogels were tested by alternately exposing pH sensing hydrogel discs to two extreme pHs (pH 4.00 and 8.50). The pH sensing with MBA-AuNP embedded MPAC hydrogels was fully reversible within 5 cycles, as illustrated in Figure 3-14B. Base on the two-tailed t-test, relative SERS intensity of COO^- stretching mode at either pH 4.00 or pH 8.50 was not statistically significantly different within the tested cycles ($\alpha>0.05$).

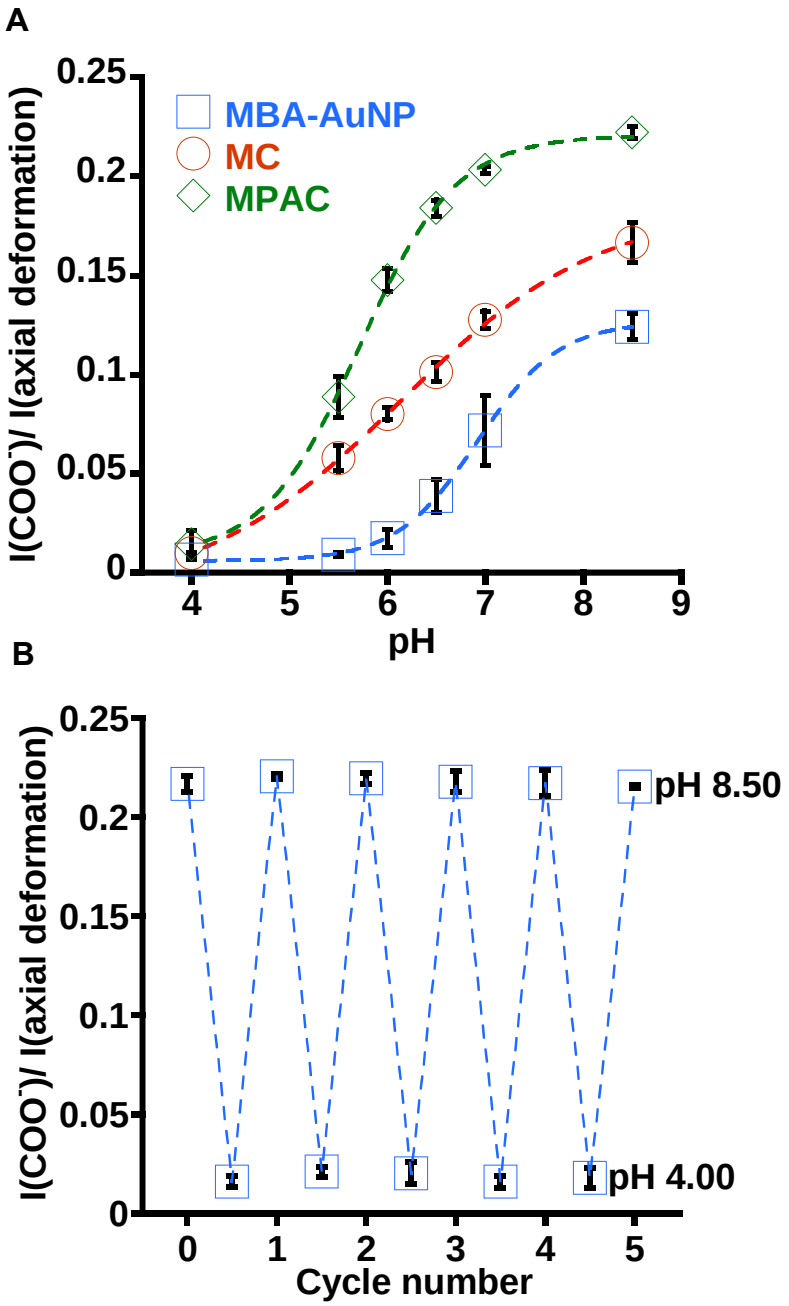

Figure 3-14. pH calibration curves of MBA-AuNP in free solution, in PEM MCs, and in MPAC hydrogels (A) and SERS ratio change of MBA-AuNP embedded hydrogels with five cyclic pH changes (between pH 4.00 and 8.50) (B). Error bars represent 95 % confidence intervals. Five samples were obtained from three different synthesis batches (n=3).

Table 3-2. Estimated sensor parameters of MBA-AuNP, PEM MCs containing MBA-AuNP, and MPAC hydrogels containing MBA-AuNP. LLOD, ULOD, and analytical range represent lower limit of detection, upper limit of detection, and ULOD-LLOD, respectively

	MBA-AuNP	***MC***	***MPAC***
LLOD [pH]	5.13	4.60	4.39
ULOD [pH]	8.38	7.80	7.53
Analytical range [pH]	3.25	3.20	3.14
pKa [pH]	6.87	6.07	5.68
Sensitivity [pH^{-1}]	0.036	0.040	0.062

3.3.5. **Optical sensing with dual modal sensing hydrogels**

The effect on SERS signal of MBA-AuNP due to the co-presence of PEM MCs containing oxygen sensitive dyes in the same hydrogel matrix was investigated with a confocal Raman system. As shown in Figure 3-15, raw SERS spectrum of dual modal sensing hydrogel showed luminescence background, which was caused by $PdPh_4(SO_3Na)_4TBP$. However, all Raman fingerprints of MBA were distinguishable over the huge Raman background. Baseline spectrum was successfully estimated using Crystal Sleuth.[127] Baseline corrected spectra were further used for data analysis. To study the effect of luminescence background on SERS based pH sensing, the pH sensitivity of dual modal sensing hydrogel was compared with that of a negative control, pH sensing hydrogel (Figure 3-16). To construct pH calibration curves, pH dependent

SERS spectra were collected from three hydrogel discs (n=3) punched from single hydrogel slab (Figure 3-17A). According to the 3 σ approach, lower limit of detection (LLOD) and upper limit of detection (ULOD) of dual modal sensing hydrogel were found at pH 4.18 and 7.21, respectively, as summarized in Table 3-3. The analytical range of dual modal sensing hydrogel was slightly decreased and shifted toward to a lower pH regime compared to that of pH sensing hydrogel. Nevertheless, there is no significant difference of pH sensitivity between those two hydrogels (0.064 pH^{-1} for pH sensing hydrogel; 0.065 pH^{-1} for dual modal sensing hydrogel) according to the two-tailed t-test (α>0.05). These results suggest that the phosphorescence of oxygen sensing dye in discrete PEM MCs does not interfere with pH dependent SERS signals.

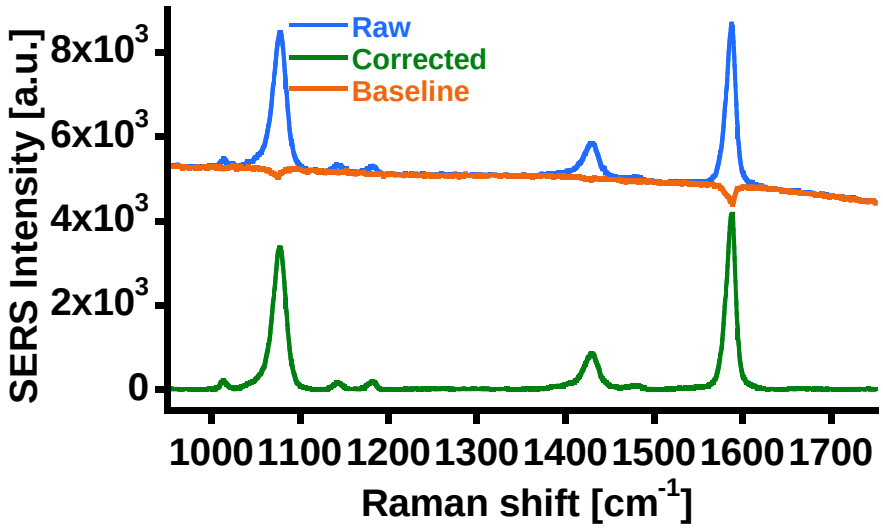

Figure 3-15. SERS spectra of dual modal sensing hydrogel incubated in 10 mM MES buffer containing 10 mM $CaCl_2$ at pH 7.00.

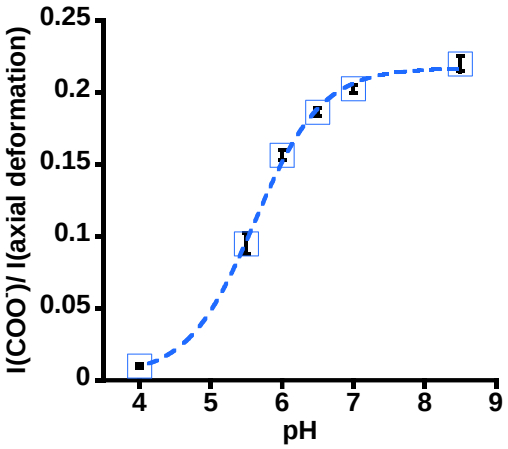

Figure 3-16. A pH calibration curve of pH sensing hydrogel. Error bars represent 95 % confidence intervals. Three different hydrogel discs were obtained from single hydrogel slab (n=3).

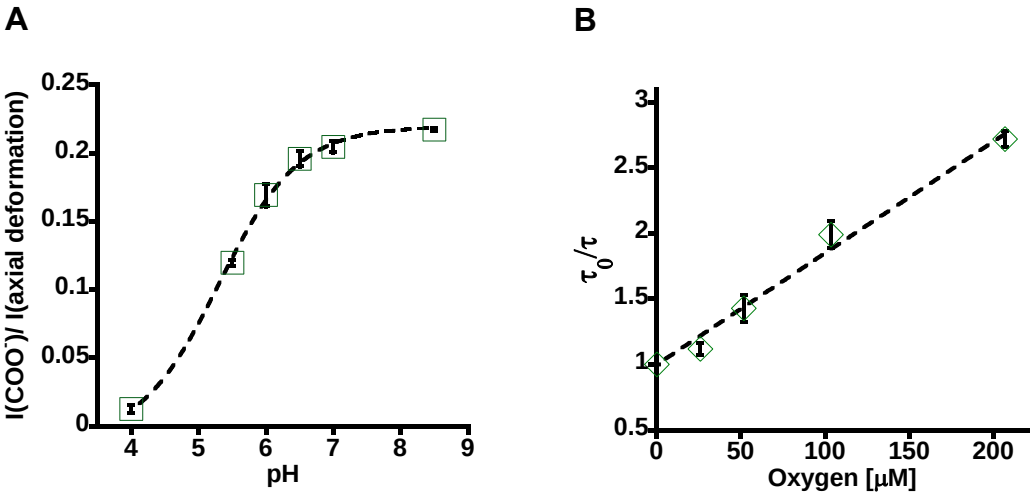

Figure 3-17. (A) A pH calibration curve of dual modal sensing hydrogel. Three different hydrogel discs were obtained from single hydrogel slab (n=3). (B) A Stern-Volmer plot of dual modal sensing hydrogel. Four different hydrogel discs were obtained from single hydrogel slab (n=3). Error bars represent 95 % confidence intervals.

Table 3-3. Estimated sensor parameters of pH sensing hydrogel and dual modal sensing hydrogel

	pH sensing hydrogel	***Dual modal sensing hydrogel***
LLOD [pH]	4.35	4.18
ULOD [pH]	7.52	7.21
Analytical range [pH]	3.17	3.03
pKa [pH]	5.60	5.36
Sensitivity [pH^{-1}]	0.064	0.065

Following the demonstration of SERS based pH sensing with dual modal sensing hydrogel, the oxygen sensing ability of such hydrogel was also evaluated by comparing its sensitivity with that of oxygen sensing hydrogel. Oxygen concentration dependent optical signal changes were quantitatively evaluated with Stern-Volmer equation:

$$\frac{\tau_0}{\tau} = 1 + K_{SV}[O_2]$$

In this relationship, τ_0 and τ are phosphorescence lifetimes with and without oxygen, respectively; K_{SV} is Stern-Volmer quenching constant and $[O_2]$ is oxygen concentration. To build Stern-Volmer plots, normalized phosphorescence lifetime (τ_0/τ) were recorded with three different discs (n=3) obtained from a slab of hydrogel by varying oxygen concentration (Figure 3-18 for oxygen sensing hydrogel; Figure 3-17B for dual modal

sensing hydrogel). The average K_{SV} values for both hydrogels were found to be 0.009 μM^{-1}. The K_{SV} values of our sensors were about three times lower than those of similar MPAC hydrogels containing Pd-meso-tetra (4-carboxyphenyl) porphine (PdTCPP).[120] However, our MPAC hydrogels did not decrease in oxygen sensitivity at higher oxygen concentrations (>100 μM) as seen with MPAC hydrogels containing PdTCPP. Moreover, from the result of two tailed t-test, it was concluded that K_{SV} of dual modal sensing hydrogel was not statistically different from that of oxygen sensing hydrogel (α>0.05). It has been reported that the SPR of plasmonic metal surface enhances the phosphorescence of porphyrin dye when the dye is located in the vicinity of the metal surface.[128-129] In the case of dual modal sensing hydrogel, the oxygen sensitivity change due to such phosphorescence enhancement was not observed. This result can be explained by the fact that the porphyrin dye in dual modal sensing hydrogel is spatially separated from AuNP aggregate by PEM nanofilms.

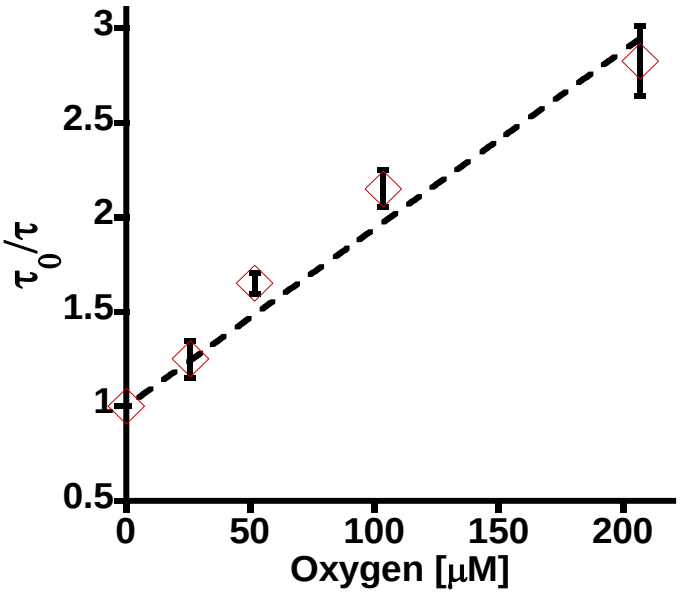

Figure 3-18. A Stern-Volmer plot of oxygen sensing hydrogel. Error bars represent 95 % confidence intervals. Three different hydrogel discs were obtained from single hydrogel slab (n=3).

To test the viability of enzymatic sensing with dual optical modes, enzyme was incorporated into the dual modal sensing hydrogel. As a proof of concept, GOx was chemically crosslinked in the matrix of alginate hydrogel whereas each sensing chemistry was embedded in discrete MCs. SERS based detection mode indirectly measures surrounding glucose concentration by monitoring local pH change in the microdomains due to gluconic acid production.[109] As illustrated in Figure 3-19, as glucose level was increased from 0 to 400 mg/dL, the relative SERS intensity of COO^- stretching mode (I(COO^-)/I(axial deformation)) decreases as a result of local pH drop in

the MCs. On the other hand, phosphorescence based detection mode allows indirect glucose measurement through estimating O_2 consumption in the MCs.[120] Phosphorescence lifetime elevated because of higher O_2 consumption (lower O_2 level) as glucose concentration was changed from 0 to 400 mg/dL (See Figure 3-19). Redundant glucose measurements from a single hydrogel can be achieved by combining these two optical modes. It is noteworthy that the dual optical modes with inverse glucose sensitivity can provide an improved accuracy and a means of sensing failure detection owing to measurement redundancy. In addition, the reversibility of glucose sensing with dual optical modes were also tested by exposing the discs of glucose sensing hydrogel alternatively to 0 and 400 mg/dL glucose. As described in Figure 3-19, both optical modes successfully tracked the changes in glucose concentration for up to 3 cycles. For each optical mode, any statistically significant difference was not observed in the optical signals at either of two glucose levels for the tested cycles ($p>0.05$).

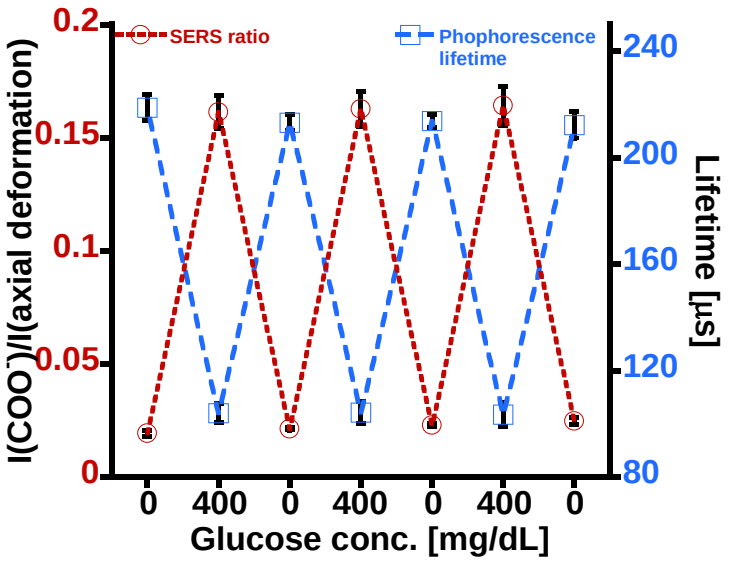

Figure 3-19. SERS ratio change of glucose sensing hydrogels (three different hydrogel discs were obtained from single hydrogel slab; n=3; red dashed line) and phosphorescence lifetime change of the same hydrogels (three different hydrogel discs were obtained from single hydrogel slab; n=3; blue dashed line) with three cyclic glucose concentration changes (between 0 and 400 mg/dL). Error bars represent 95 % confidence intervals.

3.4. **Conclusion**

Microdomain-embedded hydrogels designed to produce both ratiometric SERS and phosphorescence lifetime responses to model target analytes were demonstrated. Encapsulating pH sensing and oxygen sensing components into segregated microdomains distributed in a hydrogel matrix allowed use of the discrete domains to individually analyze pH and oxygen using the dual sensing nature of the material. The statistically equivalent response of the dual-modality materials compared to single-

modality controls indicated an absence of confounding spectral interference between the two chemo-optical transducers integrated into a matrix, suggesting potential to expand this concept to a broader scope of transduction elements. Further, the individual microcapsule sensors exhibited sensitive and reversible responses to different aspects of a localized reaction driven by an enzyme incorporated into the matrix. This supports the prospect of using such embedded components to endow materials with multiple reactive/responsive properties in a highly controlled manner. Such a capability opens up possibilities for incorporating complementarily-, redundantly, and/or orthogonally-functional elements to increase reliability, enhance efficiency, expand utility, and improve overall performance for many applications involving sensing and monitoring.

4. SERS-ACTIVE SMART HYDROGELS WITH MODULAR MICRODOMAINS: FROM pH TO GLUCOSE SENSING*

4.1. **Introduction**

The characteristic of SERS based systems is the strong wavelength dependence of the SPR, which may be controlled by varying the shape, composition, aggregation state,[130] and structural anisotropy[131] of particular importance for applications where the light must penetrate turbid samples such as biological tissue, which exhibits wavelength-dependent absorption and scattering properties. A number of different strategies have been explored both theoretically and experimentally to control and maximize the local SPR effect, including various materials and structures. These may be broadly categorized into nanoparticles and nanostructured surfaces. Nanoparticles of many compositions and 3D structures have been demonstrated as effective in enhancing intensities of Raman-active molecules; examples include gold, silver, copper and spheres, rods, stars, urchins, advantages of relatively facile and efficient solution-phase flowers, onions, etc.[88, 132-137] These nanomaterials offer typical advantages of relatively facile and efficient solution-phase synthesis, high surface area, and excellent sensitivity; by modifying their surfaces with ligands specific to target molecules (e.g. antibodies, aptamers, synthetic receptors), these become highly-selective assays based on changing

*© [2017] IEEE. Reprinted, with permission, from [You, Y. H.; Nagaraja, A. T.; Biswas, A.; Hwang, J. H.; Coté, G. L.; McShane, M. J., SERS-based Hydrogel Sensors for pH and Enzymatic Substrates, and Feb/2017]

SPR and/or SERS signals. These have been reviewed recently and need not be discussed in detail here.[138] What is important to appreciate in this context is that nanoparticle systems all suffer from the same limitations in terms of potential for use in sensor devices: they are "free-floating" colloidal suspensions that were designed as single-shot assays and, therefore, they must be physically immobilized within or on the surface of a supporting material to be used in continuous monitoring.

Nanostructured surfaces overcome some of the limitations of the nanoparticles, as these are fabricated on bulk substrates that may be continuously exposed to a sample of interest for continuous readout. Some very elegant designs have been realized to achieve excellent SERS performance. The metal film on nanospheres (MFONs) architecture is the one of the most popular for nanostructured SERS substrates. MFONs are fabricated by depositing a metal thin film on a layer of closed-packed nanoparticles.[56] Due to the periodic structure, MFONs yield a strong SERS enhancement; the enhancement factor can be engineered by controlling metal thin film thickness, nanoparticle size, and the distance between neighboring nanoparticles.[139] Moreover, the surface of MFONs can be easily modified with self-assembled layers (SAMs) to attract multiple analytes in the vicinity of the metal surface.[140] There are other approaches using nanolithography such as embossed nanostructure patterns prepared by e-beam[141] and array of nanoholes fabricated by focused ion beam (FIB).[142] Similar to MFONs, these SERS substrates provide good reproducibility and uniformity having consistent hot spots.[143] Despite these advantages, the relatively slow, complex

fabrication process and high cost act as a hurdle for this SERS substrate to be applied to many sensor applications.

When it is necessary to continuously monitor composition or sense specific analytes in aqueous media, as is the case in many real-world situations in environmental and biomedical fields, some basic requirements must be met. Such devices must provide fully-reversible behavior with low drift (i.e. low fouling), low background signals from surrounding media (high signal-to-noise ratio), and some means of selective response to the target species. Additional constraints of biocompatibility (non-toxic, non-reactive) are presented when the sample is biological in nature or influence (cell culture, ponds, living organisms, etc.). Finally, if considered for use inside of living organisms, even more stringent biocompatibility requirements hold: materials generally must be soft to match the surrounding tissue, non-immunogenic, and low-fouling and must further be designed with optical properties allowing sufficient tissue penetration (near-infrared excitation). In reviewing these needs, it becomes obvious that the available SERS platforms have some critical limitations. The particulate systems must be injected into samples, an approach that is effective for diagnostics but is not well suited for sensing and monitoring because of rapid migration, aggregation propensity[144] and potential accumulation in non-desirable locations.[145] It is also noteworthy that dispersion of nanoparticles may compromise the utility of some SERS assays, because some of their action in enhancement relies upon aggregation induced by binding the target molecules; in addition, the immobilization process often results in generation of additional background signal arising from the matrix employed. The solid substrates are better

suited for continuous analysis, as they offer a fixed point of detection. However, all current SERS systems possess substantial drawbacks related to environmental compatibility—they must not perturb the sample being analyzed. In biological systems for example, there are added concerns of mechanical mismatch,[146] interaction with immune system components and cells,[147] as well as potential toxicity.[148]

Two examples of different approaches towards meeting these requirements offer greater insight into the potential for such devices. The Van Duyne group reported an elegant approach to *in vivo* analysis: silver film over nanospheres (AgFONs) were fabricated on a planar titanium plate and a specialized mixture of self-assembled monolayers was used to selectively partition some small molecules near the plasmonic surface.[149] The device was implanted in a mouse and was found to be functional for over two weeks; nonetheless, the method involved surgical implantation, required an implanted optical window for monitoring, and presumably engendered a significant host response to the rigid Ti substrate implanted in soft tissue. Vo-Dinh's group recently reported a preliminary example of a solution for implantable SERS devices using gold nanostars in a pHEMA hydrogel.[150] They detected SERS signals of Raman reporters attached to the nanostars within devices implanted in live rats and pigs; while they observed excellent signal detection over the tissue background, they also observed that the gold nanostars magnified not only the Raman signal of Raman active dye but also that of the hydrogel. Therefore, a more efficient approach to immobilizing sensor particles is critical for practical SERS-based monitoring.

Recently, biocompatible nano-composite hydrogels were reported to effectively separate plasmonic materials from the external surroundings as well as from the matrix itself.[118] Such SERS sensing hydrogels are based on a flexible design that has three key consistent features: (1) a biocompatible hydrogel matrix; (2) microcapsules embedded in the matrix, which spatially confine the otherwise "free" SERS sensing materials to small volumes and (3) selectively SERS-active particles that generate the desired optical sensing response.

In this study, we aimed to adapt this platform into a unique modular approach to SERS sensing devices that address the limitations of previous systems noted above, particularly for use in a wide variety of conditions including implants. As illustrated in Figure 4-1, a hydrogel-based SERS sensing material combined with a Raman instrument can act as a pseudo-solid-state device to analyze various types of aqueous samples. In principle, large molecules are excluded from the hydrogel, while the microcapsules serve as a finer control over size of molecules that may interact with the plasmonic particles to generate a SERS signal.[151-153]

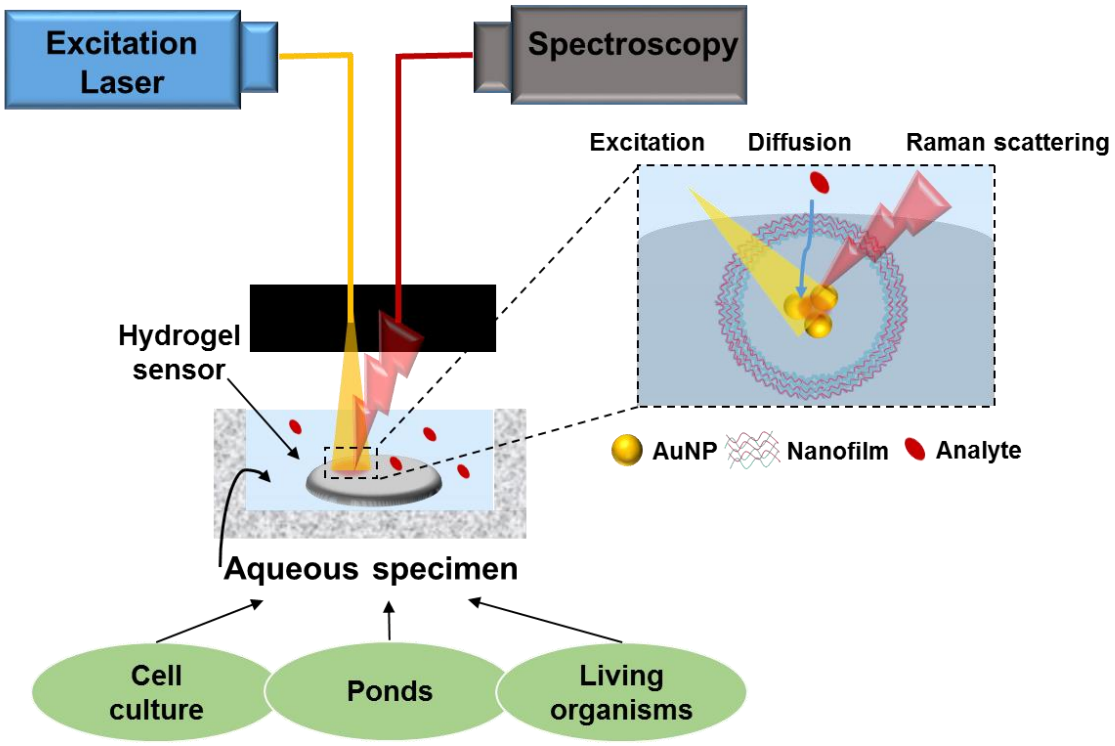

Figure 4-1. Diagram of hydrogel based SERS sensing for aqueous specimens.

4.2. **Sensor design and theory**

To prove the viability of the hydrogel-based SERS sensor, 4-Mercaptobenzoic acid (MBA) was chosen as a Raman-sensitive dye to estimate pH in alginate hydrogels. Furthermore, the potential for the pH-sensing hydrogel to track pH changes resulting from localized reactions was investigated by introducing an oxidase enzyme. Finally, the microcapsule permeability was decreased to evaluate the potential for adjusting the amount of local pH change induced by the enzymatic reaction. Specifically, as illustrated in Figure 4-2A, a pH-sensitive Raman probe (MBA) was used to establish the sensitive and fully reversible pH sensing capability of the hydrogel. By further incorporating

glucose oxidase (GOx), the pH sensing chemistry was extended to show a response with glucose. As glucose diffuses into the microdomain of hydrogel (See Figure 4-2B), it is oxidized in the presence of glucose oxidase (GOx) to produce gluconic acid. The reactions involved can be expressed as:[154]

$$\mathrm{E_o} + \mathrm{G} \underset{k_1, k_{-1}}{\longleftrightarrow} X_1 \underset{k_2}{\rightarrow} \mathrm{E_r} + \mathrm{P}$$

$$\mathrm{E_r} + O_2 \underset{k_3, k_{-3}}{\longleftrightarrow} X_2 \underset{k_4}{\rightarrow} \mathrm{E_o} + H_2O_2$$

where G and O_2 represent the glucose and oxygen substrates while P and H_2O_2 represent the gluconic acid and hydrogen peroxide products, respectively. The oxidized and reduced forms of the enzyme are represented by E_o and E_r, and the enzyme-substrate complexes are given by X_1 and X_2, respectively. The forward and reverse reaction rate constants are given by k_1, k_{-1}, k_2, k_3, k_{-3}, and k_4. From this reaction scheme, a total of six equations may be written from the standard diffusion-reaction equation as:[155-156]

$$\frac{\partial C_i}{\partial \mathrm{t}} = D_i \nabla^2 C_i - R_i$$

where the diffusivity of species *i* (i.e., glucose, oxygen, protons, etc.) is expressed by D_i, and R_i and represents a reaction term for substrate consumption (i.e., $R_G = k_1 C_G C_{E0} - k_{-1} C_{X1}$ and $R_{H+} = k_2 C_{X1}$ for glucose and hydrogen ions, respectively).

If the reaction proceeds at a rate sufficient to accumulate hydrogen ions before they can diffuse away, the diffusion-reaction balance of all constituents results in a corresponding drop in microdomain internal pH. Most importantly for substrate sensing, a constant glucose supply will result in an internal pH that will reach a steady-state value depending on the relative flux of glucose (inward) and protons (outward). Note that this

situation holds true if there is sufficient active enzyme present and supply of co-substrate oxygen.

The decreasing pH is expected to affect the pH-sensitive Raman molecule (MBA) coated on the AuNP surface by reducing the relative peak intensity ratio of the pH sensitive stock mode. It is noteworthy that similar behavior is expected for any oxidase enzyme and corresponding substrate.

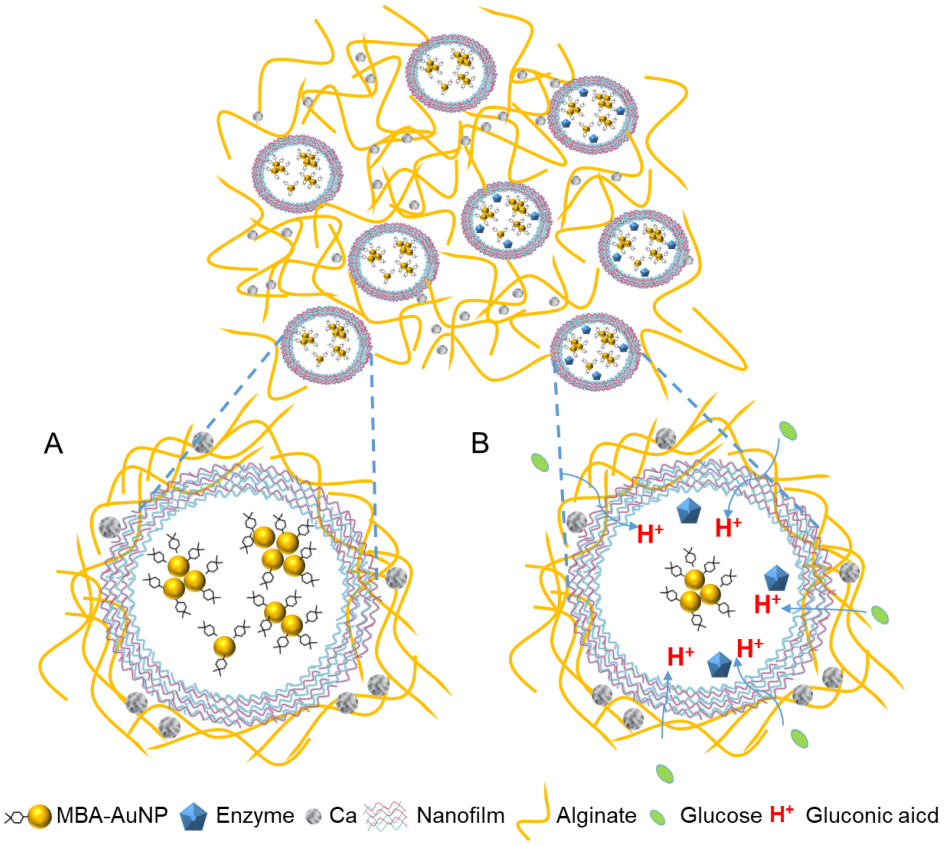

Figure 4-2. Illustration of a SERS sensing hydrogel. (Millions of microdomains encapsulating sensing chemistries are distributed throughout the hydrogel matrix.) (A) A single domain of the encapsulated nonenzymatic pH sensing system (B) A single domain of the encapsulated enzymatic glucose sensing system.

4.3. **Experimental**

4.3.1. **Materials**

Gold chloride trihydrate ($HAuCl_4 \cdot 3H_2O$), sodium citrate tribasic dihydrate, 4-mercaptobenzoic acid (MBA), sodium carbonate (Na_2CO_3), sodium bicarbonate, poly (allylamine hydrochloride) (PAH, average M_w 15 kDa) poly (diallyldimethylammonium chloride) (PDADMAC, average M_w 100-200 kDa), poly(sodium 4-styrenesulfonate) (PSS, average M_w 70 kDa), 2-(N-morpholino) ethanesulfonic acid (MES) sodium salt, alginic acid sodium salt (from brown algae, ~250 cps for 2 % solution at 25 ºC), calcium carbonate ($CaCO_3$), TRIS HCl (Tris(hydroxymethyl)aminomethane hydrochloride), and glutaraldehyde solution (grade II, 25 % in H_2O) were purchased from Sigma-Aldrich (St. Louis, MO, USA). Ethanol (200 proof, USP), calcium chloride ($CaCl_2$), D-(+)-glucono-1,5-lactone (GDL) and glucose oxidase (from *Aspergillus niger*, 257 U/mg) were obtained from Decon Labs (King of Prussia, PA, USA), Macron fine chemicals (Center Valley, PA, USA), Alfa Aesar (Ward Hill, MA, USA) and BBI solutions (Cardiff, UK), respectively.

4.3.2. **AuNP synthesis**

The seed-mediated AuNP synthesis method of Bastus *et al.*[157] was used, with minor modification. Briefly, AuNP seeds were prepared by adding 335 µL of 25 mM $HAuCl_4$ aqueous solution into a 200 mL round bottom three neck flask containing boiling 2.2 mM sodium citrate solution (50 mL). The reaction mixture was stirred and boiled under reflux for 10 min. The color of the mixture changed from transparent to

pale red, confirming the formation of AuNP seeds. To grow a gold nanoshell around the AuNP seed, the seed solution was instantly cooled down to 90 ºC followed by the sequential addition of 60 mM sodium citrate (335 µL) and 25 mM aqueous $HAuCl_4$ (335 µL) with a time delay of 2 min. The gold nanoshell coating was obtained after 30 min of further stirring at 90 ºC with refluxing. In this study, the gold nanoshell growth was stopped after the 8th deposition cycle to achieve a targeted diameter of 50 nm; this size was selected based on previous findings that 50 nm gold nanoparticles had the largest SERS enhancement in the nanoparticle size range of 17 to 80 nm.[158]

4.3.3. **Surface modification of AuNPs**

Citric acid-capped AuNPs were modified with 4-Mercaptobenzoic acid (MBA) using a slightly altered procedure of Jaworska *et al*.[159] Ethanolic MBA (200 µL of 1 mM) was quickly dropped into a 2 mL centrifuge tube containing 2 mL of AuNP suspension. The mixture was vortexed for 5 min and then centrifuged at 2000 g for 15 min. After supernatant removal, residual particles were suspended in 200 proof ethanol (2 mL) to remove excess MBA molecules. Ethanol was separated by centrifugation using the same conditions mentioned above and the remaining MBA-coated AuNPs were redispersed in 200 µL of DI water.

4.3.4. **Encapsulation of MBA-AuNPs and GOx in polyelectrolyte mutilayer coated $CaCO_3$**

MBA-AuNPs and GOx were encapsulated in calcium carbonate microparticles (MPs) via a co-precipitation method, and polyelectrolyte multilayers (PEM) were coated onto the MPs using Layer by Layer self-assembly.[160] We prepared two different types of PEM-coated $CaCO_3$ MPs: one for pH sensing hydrogels and the other for enzymatic glucose sensing hydrogels.

4.3.4.1. **pH-sensitive hydrogel sensors**

MBA coated AuNP (MBA-AuNP) solution (400 μL) was suspended with 6 mL of 0.2 M Na_2CO_3 solution. MBA-AuNP encapsulated $CaCO_3$ microparticles (MPs) were co-precipitated by the rapid injection of 0.2 M $CaCl_2$ solution (6 mL) into the suspension under vigorous stirring. After 30 sec of stirring, the solution stood for 10 min showing sedimentation of the precipitated $CaCO_3$ MPs. The $CaCO_3$ MPs were collected by 2 min of centrifugation at 200 g and then rinsed with 5 mM sodium bicarbonate buffer solution (pH 8.00). The MPs obtained from the 1 mL of MBA-AuNP containing $CaCO_3$ solution were immersed in polyelectrolyte suspensions (2 mg/mL, pH 8.00) containing 5 mM $NaHCO_3$ beginning with PDADMAC in a 2 mL centrifuge tube followed by anionic PSS. Between each coating step, MPs were rinsed with 5 mM $NaHCO_3$ buffer (pH 8.00) and then centrifuged at 500 g for 30 sec to remove excess and unbound polyelectrolyte.

4.3.4.2. **Enzymatic glucose-sensitive hydrogel sensors**

GOx (64 mg) was dispersed in 8 mL of 0.25 M Na_2CO_3 solution. 400 µL of MBA-AuNP solution and 0.25 M $CaCl_2$ solution were sequentially added into this suspension. The mixture was stirred for 30 sec and then allowed to settle for 10 min. The sedimented MPs were collected and cleaned with 5 mM sodium bicarbonate buffer solution at pH 8.00. The MPs were initially coated with 5 bilayers of PDADMAC/PSS to ensure complete surface coverage and 7 bilayers of PAH/PSS were added ($(PDADMAC/PSS)_5$-$(PAH/PSS)_7$) by the same method to reduce diffusion of glucose into the micro-domains as a means to make the system glucose-limited.[161] Apart from changing types of PEMs we also tried to crosslink the ($(PDADMAC/PSS)_5$-$(PAH/PSS)_7$) with glutaraldehyde to further limit glucose flux through the MCs. Briefly, 3.3 mg of ($(PDADMAC/PSS)_5$-$(PAH/PSS)_7$) coated MPs were incubated in 10mL of 3M glutaraldehyde solution for 15 min. Resultant MPs were washed with 5 mM $NaHCO_3$ buffer solution at pH 7.20.

4.3.5. **Synthesis of hydrogel sensors**

4.3.5.1. **pH-sensitive hydrogel sensors**

Hydrogels were prepared using a modification of our standard MPAC protocol.[118] Briefly, 250 µL of alginate solution (3 w/v%) was mixed with 125 µL of $(PDADMC/PSS)_{10}$-coated MPs (3.3 mg). To this, 125 µL of GDL solution (120 mg/mL) was quickly added and mixed well via pipetting. The mixture was then molded in a 0.03” thick Teflon spacer sandwiched between two glass slides.

4.3.5.2. **Enzymatic glucose-sensitive hydrogel sensors**

Initially, PEM microcapsules (PEM MCs) were prepared by dissolving the coated calcium carbonate templates using 0.2 M MES buffer at pH 6.10. The PEM MCs were dispersed in 75 µL of DI water and then mixed with 25 µL of $CaCO_3$ solution (1.0 mg/mL); the latter provides the source of calcium for faster alginate gelation. This slightly modified procedure was used for the glucose sensors to circumvent the otherwise very slow gelation of the alginate after crosslinking the microcapsules. This mixture was vortexed with 3 w/v% alginate solution (200 µL). Finally, the mixture was mixed with 0.5 M MES buffer at pH 5.80 (100 µL) to dissolve $CaCO_3$.and form the gel.

4.3.6. **UV-Vis spectroscopy**

A Cary 50 UV-Vis spectrophotometer (Agilent Technologies, Santa Clara, CA, USA) recorded UV-Vis extinction in the range of 400 to 800 nm. The absorbance data were collected with a scan speed of 300 nm/sec and 0.5 nm resolution. For these measurements, the citric acid-AuNP stock solutions were diluted to 1/10 with DI water, while MBA-AuNP stock was diluted with the same solvent by 1/50.

4.3.7. **Nanoparticle tracking analysis (NTA)**

Size analysis via NTA was performed using a NanoSight LM10HS (Malvern Instruments Ltd, Malvern, UK) equipped with a 405 nm laser source (65 mW). Prior to the measurement, citric acid-AuNPs and MBA-AuNPs were diluted with DI water by a factor of 4500 and a factor of 2235, respectively. Under these conditions, the NTA

system tracked the paths of more than 1000 nanoparticles with 3 min video of scattered light from recorded on a C11440-10C Orca Flash2.8 CMOS camera (Hamamatsu, Hamamatsu-city, Japan). The video was further analyzed by NanoSight 2.7 software to calculate hydrodynamic size and concentration.

4.3.8. **Transmission electron microscopy (TEM)**

Samples were prepared from 2 µL of stock solution (for MBA-AuNPs) diluted with 98 µL DI water. The diluted solution was sonicated for 10 min to minimize possible aggregation. 5 µL of the sonicated solution was then dropped onto a carbon film coated 300 square mesh copper grid (CF-300 Cu, Electron Microscopy Sciences, Hatfield, PA, USA), and the loaded copper mesh was dried for 24 hrs in atmosphere. The AuNPs were characterized using TEM (HF3300, Hitachi Scientific Instruments, Tokyo, Japan) with a cold field emission gun operating at 30 kV, with magnifications of 20000×.

4.3.9. **Raman measurement**

Hydrogel discs with 2 mm diameter were excised from the prepared slabs using a biopsy punch. The discs were washed with 300 µL of desired buffer solution three times and kept in the same buffer (300 µL) for 30 min to achieve saturated pH levels inside the micropores contained in the hydrogels prior to Raman characterization. For the non-enzymatic pH sensing hydrogels and enzymatic glucose sensing hydrogels, 10 mM MES with 10 mM $CaCl_2$ (pH 4.00, 5.50, 6.00, 6.50, 7.00 and 8.50) and 1 mM TRIS with 10 mM $CaCl_2$ (pH 7.00) were used, respectively. The discs were placed into the wells of a

384-well plate, and 30 μL of the same buffer was added over the discs; for the enzymatic glucose sensor discs, buffer with glucose was also used. Briefly, the glucose sensitivity of the enzymatic glucose sensing hydrogels containing uncrosslinked PEM microcapsules was examined by exposing discs punched from the glucose-sensitive hydrogel to 4 different glucose concentrations (0, 100, 200 and 400 mg/dL) for different incubation times (0, 60, 120, 180 and 240 min). In the case of crosslinked MC encoded glucose sensing hydrogel, glucose dependent SERS based pH sensing was monitored by incubating discs punched from the glucose-sensitive hydrogel to 5 different glucose concentrations (0, 100, 200, 300 and 400 mg/dL) for different incubation times (0, 60, 180, 240, 300 and 360 min). SERS spectra were recorded using a DXR Raman confocal microscope (Thermo Scientific, Waltham, MA, USA). A 780 nm laser with 20 mW power was utilized as the excitation source. During the measurement, the laser was focused near the surface of the discs and scattered light was collected via a 10× objective lens, as illustrated in Figure 4-3. The collection time for a single spectrum was 3 sec; five spectra were averaged for each specimen.

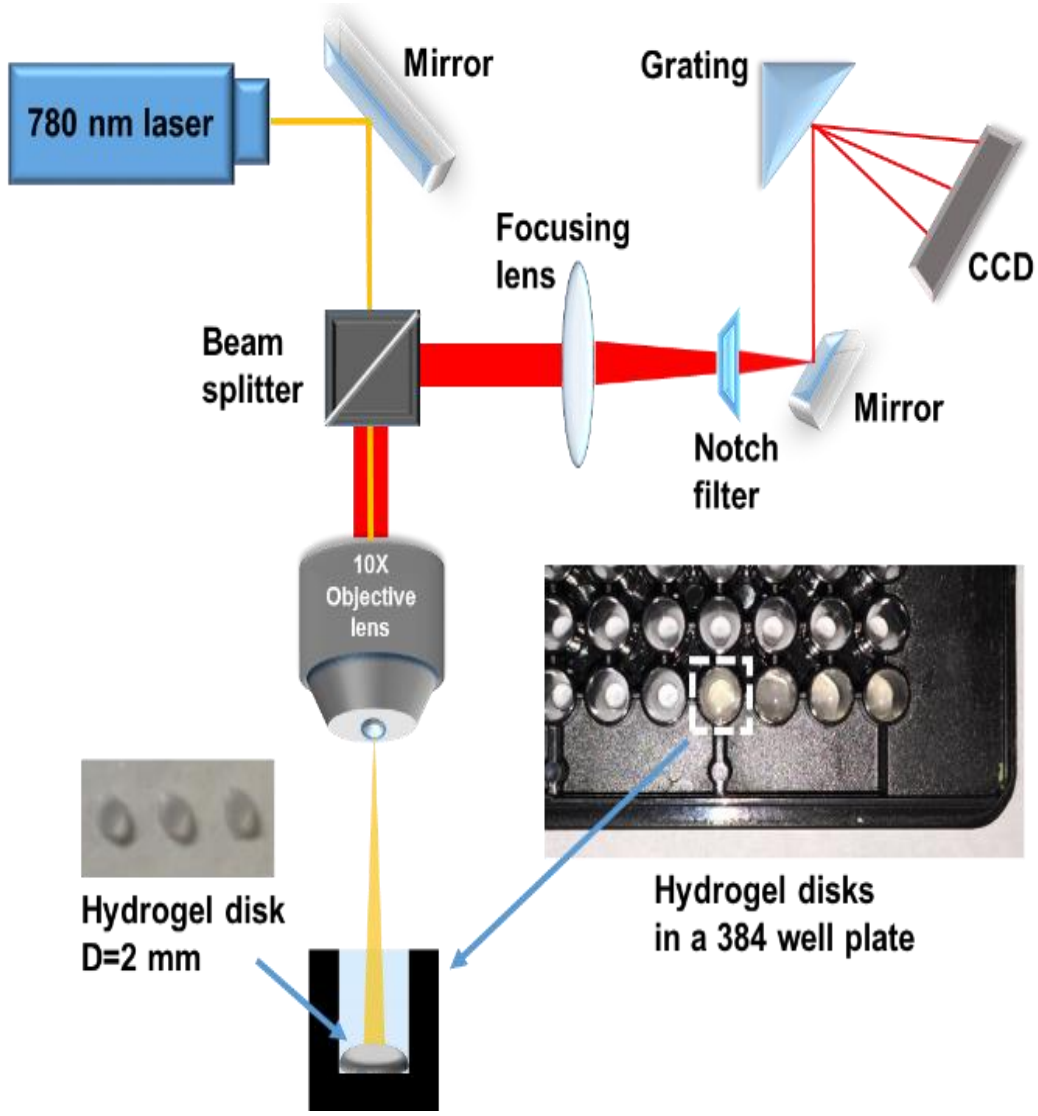

Figure 4-3. Diagram for Raman experiment set up for SERS sensing hydrogels.

4.4. **Results and discussion**

The growth of AuNP seeds and the surface modification of final AuNPs were monitored by UV-Vis extinction spectra as described in Figure 4-4A. Mie theory based UV-vis spectra analysis enabled the size estimations of seeds and final AuNPs which

were prepared by 8 steps of nanoshell growth.[162] The ratios of extinction at SPR peak to extinction at 450 nm result in estimates of 17.8 and 50.2 nm for the diameter of the seeds and the final citric acid-AuNPs, respectively. The MBA coating provides extinction intensity loss at the SPR of citric acid-AuNP and development of new band at 674 nm. The band at 674 nm can be explained by the longitudinal plasmon oscillation toward the long axis of elongated gold nanoaggregates.[163] TEM also allowed visualization of the difference in particle dispersion before and after MBA capping, from which it was observed that AuNPs formed aggregates upon ligand exchange, with a transition from fully dispersed state to dimers, trimers and higher-order aggregates (Figure 4-4B).

Quantitative analysis of the AuNP aggregation formation and particle concentration was performed using NTA. These results agree with previously-reported AuNP aggregation, with the UV-Vis spectra further supporting that MBA capping induced gold nanoaggregate formation.[130] As shown in Figure 4-4C, NTA successfully determines hydrodynamic size and concentration of both citric acid-AuNPs and nanoaggregates (MBA-AuNPs). Table 4-1 summarizes modes, mean sizes and stock solution concentrations of AuNPs before and after MBA coating. Citric acid-AuNPs yield a narrower size distribution with the mode of 54.0 nm and 1.01 nM of stock solution concentration. As AuNPs are capped with MBA, the hydrodynamic size is

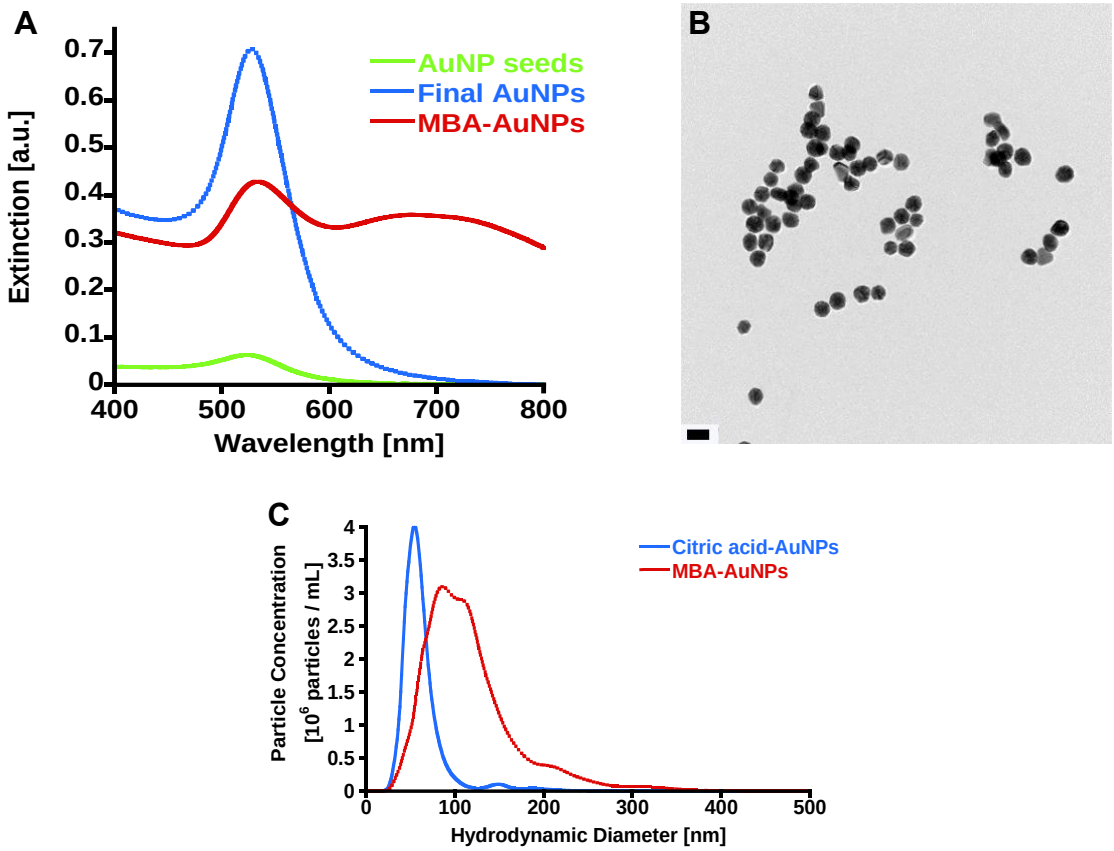

Figure 4-4. (A) UV-vis spectra of citric acid capped AuNP seeds, final citric acid capped AuNPs, and MBA capped AuNPs. (B) TEM images of MBA-AuNPs. (Scale bar represents 50 nm.) (C) Hydrodynamic size distributions of citric acid-AuNPs and MBA-AuNPs.

increased from 63.4 to 117.0 nm with the evolved distribution. Successful formation of AuNP aggregates, confirmed by the data in Figure 4-4A-C, is meaningful to SERS-based sensors; Raman "hot spots" induced by overlapping electromagnetic fields from nearby plasmonic particles are able to more effectively amplify the Raman signals of interest, thereby increasing signal to noise ratio.

Table 4-1. Modes, average diameters, and stock concentrations of citric acid-AuNPs and MBA-AuNPs determined by NTA

Sample	***Mode [nm]***	***Mean [nm]***	***Stock concentration [nM]***
Citric acid-AuNPs	54.0	63.4 ± 26.1	1.01
MBA-AuNPs	86.0	117.0 ± 52.8	1.11

The encapsulation of MBA-AuNPs in hydrogels and the possibility of these materials for use in a pH sensing platform were evaluated using Raman spectroscopy. As depicted in Figure 4-5A, the SERS spectra showed the MBA Raman peaks in the range of 1000 to 1800 cm^{-1} for each pH. This indicates that the intensity of scattered light from MBA-AuNPs is greater than that from the PEMs and the hydrogel matrix, as shown in Figure 4-5B. This higher intensity results from the localized electromagnetic field around the AuNP surface, which appears to selectively amplify the Raman signal of MBA with no observable scattering contributions from the PEMs and/or the alginate hydrogel matrix evident in spectra. Distinct MBA Raman fingerprints were confirmed at 1013, 1078, 1143, 1182, 1430, 1481, 1587 and 1702 cm^{-1}, assigned to ring deformation, ring breathing, $CCOO^-$ stretching, C-H in-plane bending, COO^- stretching, C-H in-plane bending, axial deformation, and C=O stretching, respectively.

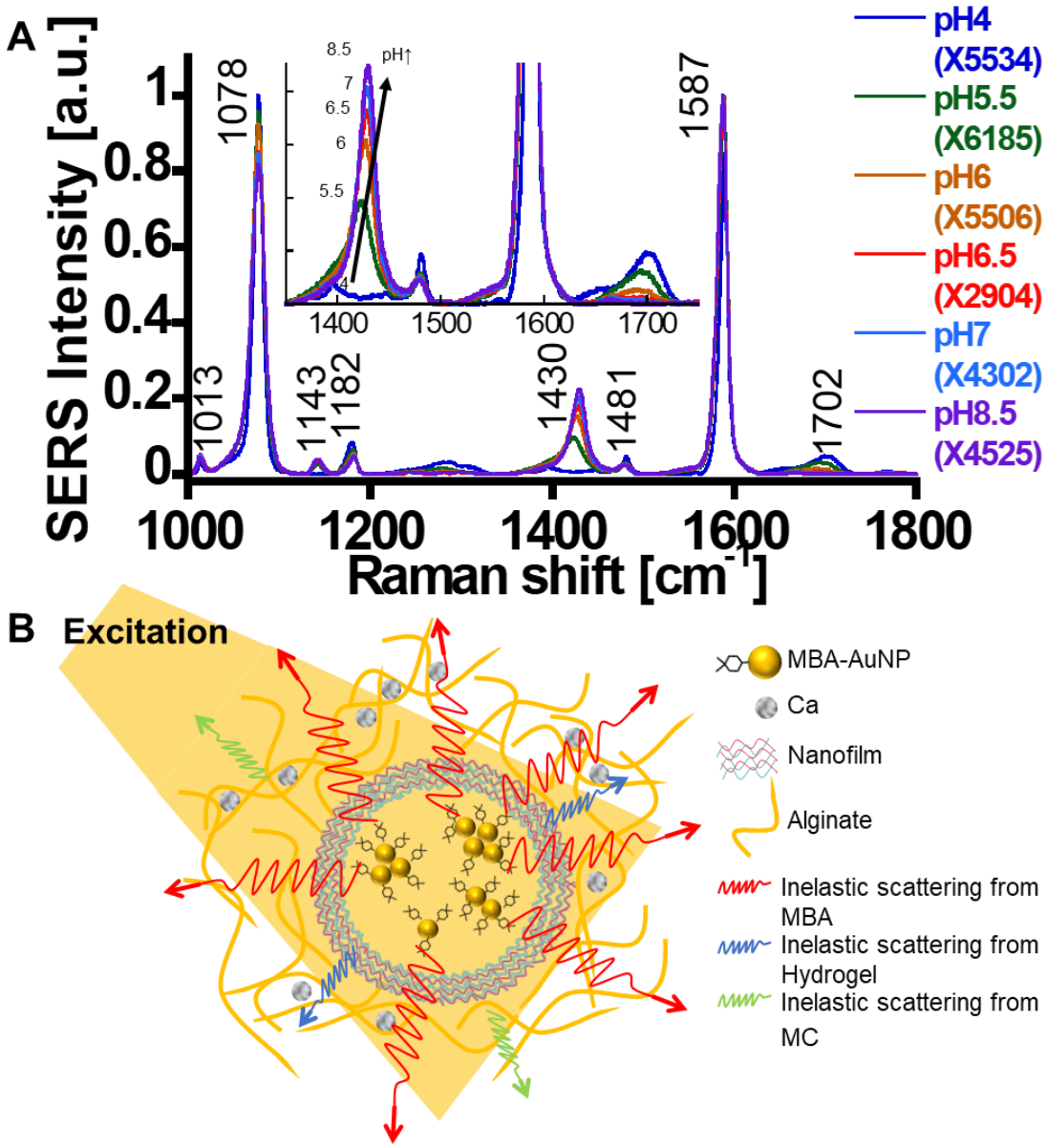

Figure 4-5. (A) Normalized SERS spectra of pH-sensitive hydrogel sensors exposed in MES buffers with various pH values. (Inset: magnified spectra centered near the axial deformation band around 1587 cm^{-1}) The legend indicates the scaling factors used to adjust spectral intensities for display on the same graph. (B) Illustration of apparent Raman scattering process in the pH-sensing hydrogel.

The MBA molecule has three significant pH-sensitive peaks from 1000 to 1800 cm^{-1}, namely: $CCOO^-$ stretching (1143 cm^{-1}), COO^- stretching (1430 cm^{-1}), and C=O stretching (1702 cm^{-1}) modes. An increase in pH around MBA-AuNPs results in the $CCOO^-$ and COO^- peak increase, whereas the C=O peak decreases. Both $CCOO^-$ and COO^- peak intensities are proportional to the number of COO^- groups in MBA molecules. If the MBA molecules are exposed to a pH above the MBA pKa value (5.80),[164] then the COOH groups of the MBA molecules are deprotonated so that both $CCOO^-$ and COO^- peak intensities become larger. On the other hand, the C=O mode intensity is related to hydrogen boding between C=O group and a proton, and/or between C=O group and a hydrogen atom in adjacent MBA molecules.[165] At a pH above the MBA pKa, the COO^- group hampers C=O from having such hydrogen bonding resulting in mode intensity fall off. As a result, C=O mode intensity is decreased with the pH increase.

Since the COO^- mode (1430 cm^{-1}) possesses the widest intensity range as a function of pH, we chose this mode to monitor pH changes in our hydrogel system. To evaluate the relationship between surrounding pH and COO^- mode quantitatively, we calculated the intensity of COO^- mode relative to the ring breathing mode (1078 cm^{-1}). A pH calibration curve was constructed using data from three different discs each from different batches of pH-sensitive hydrogel (n=3) is presented in Figure 4-6. The data points represent the relative intensity of peaks associated with COO^- and the ring breathing mode, and are plotted versus buffer pH value. The pH calibration curve was fitted with a sigmoidal function described as

$$\frac{\mathrm{I(COO^-)}}{\mathrm{I(ring\,breathing)}} = \frac{2.67 \times 10^{-5}}{9.81 \times 10^{-5} + 1.33\mathrm{e}^{(-1.99(\mathrm{pH}-1.03))}}$$

By fitting the data using a non-linear least-squares regression analysis, the pKa, lower limit of detection (LLOD), upper limited of detection (ULOD), and average sensitivity. LLOD, ULOD, and average sensitivity were calculated by a 3σ approach.[166] To obtain an estimate of random measurement error, replicate spectra were measured three times at pH 4.00. The standard deviation of relative SERS intensity ratio of COO^- to ring breathing mode were calculated for pH 4.00 (σ). LLOD and ULOD were defined as minimum intensity ratio plus 3σ, maximum intensity ratio minus 3σ, respectively. The slope of a linear line connecting LLOD and ULOD in the pH calibration curve was used to define the average sensitivity. Based on the 3σ approach, the pH sensing hydrogel yields an analytical range of pH 4.43 (LLOD) to pH 8.07 (ULOD) and the average sensitivity of 0.07 pH^{-1}. This analytical range is slightly wider and shifted to lower pH compared to a commercial fluorescence based pH sensors (pH 5.00-8.50).[167] It is noteworthy that pH drops induced by oxidoreductase enzyme reactions may be monitored within this analytical range. This result suggests that the pH of the fluid surrounding the hydrogel is successfully measurable via Raman spectra using our SERS platform.

The pKa obtained from the pH calibration curve (5.81) is smaller than what Jamieson *et al.* reported (6.00-8.00) for MBA.[168] This pKa difference can potentially be explained by interaction between Ca^{2+} ions (in buffer solution) and COO^- groups of the MBA in our case. It has been reported that the chelation of divalent metal ions by the

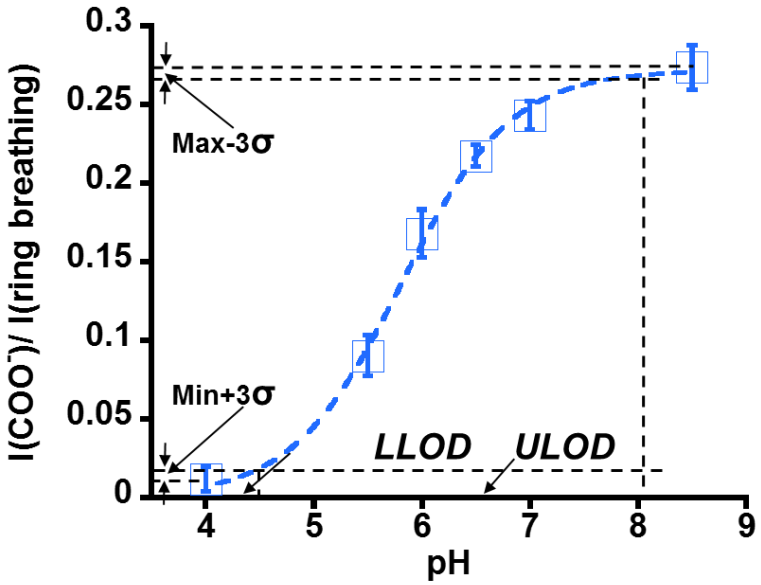

Figure 4-6. A pH calibration curve of pH-sensitive hydrogel sensors (n=3: 3 pH sensing hydrogel discs from 3 different batches; error bars represent one standard deviation of the mean).

COO^- group can elevate the SERS intensity of the COO^- peak.[126, 169] Such increase in the COO^- mode intensity can lower the pKa since the Ca^{2+} ion helps deprotonation of MBA at the lower pH regime.

The reproducibility of SERS sensing with our pH sensors was assessed by calculating relative standard deviations (RSDs) and signal to noise ratios (SNRs) of the SERS intensity at ring breathing mode (1078 cm^{-1}) and a SERS intensity ratio (I(COO)/I(ring breathing)) for 18 different samples at 6 different pH levels. The average RSDs and the average SNR of SERS intensities were estimated as 34.9 % and 2.9, respectively. In comparison, the average SERS intensity ratio had much better reproducibility (average RSD=17.1 %, SNR=5.5). Such average RSD and SNR will be

sufficient to monitor pH changes with our system. It is also noteworthy that these average values include the very low signals measured at pH 4.00, which is actually below the calculated detection limit; excluding this point, the average RSD is below 10 % (SNR>10).

We have also performed pH reversibility tests with discs taken from 5 different slabs of MPACs (5 different fabrication runs). The samples were cycled back and forth between pH 8.50 and pH 4.00 and measurements were made at 30 min after changing the solution pH. The SERS intensity ratio was found to exhibit a fully-reversible response to levels within the natural variation, indicating that the pH sensing system is able to detect the fluctuation in analyte level. More detailed study of response time, reversibility, and hysteresis is the subject of ongoing work to be reported separately.

Glucose oxidase enzyme and MBA-AuNPs were encapsulated in the same MCs to investigate the effect on the SERS signals of MBA molecules in the presence of glucose. Similar to the pH sensing hydrogel, all the Raman peaks of MBA were confirmed without any band shifts. The stock modes of GOx (1188, 1217, 1292, 1331, 1361, 1448, 1516, 1555, and 1600 cm^{-1})[170] were not detected, indicating there was no Raman signal interference by GOx in MCs. One explanation of this result could be that since both GOx and MBA are negatively charged, there may be repulsion between GOx and MBA-AuNPs. Due to this repulsion the GOx does not appear to be within the 2 nm distance from the surface of AuNPs that would allow its Raman signal to be intensified.[171] We also evaluated the pH sensing ability of the glucose-sensing hydrogels, and the corresponding analytical range was found to be pH 3.96 (LLOD) to pH 6.39

(ULOD). This analytical range was not only smaller but also shifted to a lower pH region compared to the range of the pH sensing hydrogel. The average sensitivity was slightly but significantly decreased (t-test; α=0.05), from 0.07 to 0.05 pH^{-1} by introducing GOx in the same pH sensing microdomain. The decreased sensitivity (the slop of pH calibration curve) with the presence of GOx in MCs can be explained by reduced intensity of COO^- mode relative to the ring breathing mode (the y-axis value of the pH calibration curve) due to possible electrostatic interaction between GOx and Ca^{2+} ion in buffer.[172]

To evaluate the pH change in MCs of the enzymatic glucose sensitive hydrogel induced by glucose oxidation, we monitored the SERS intensity ratio of COO^- to ring breathing mode (1078 cm^{-1}) as depicted in Figure 4-7. This intensity ratio is inversely proportional to the number of protonated COO^- groups (lower ratio=lower pH). An instant pH change was seen from neutral pH (pH 7.00) to acidic pH (pH 5.84) when the glucose sensing hydrogel sensors were subjected to 400 mg/dL glucose solution (0 min). Such an immediate pH drop by glucose implies the GOx entrapped in microdomains retains its enzyme activity. After 60 min of incubation time, the response revealed a statistically significant pH reduction from pH 7.00. For incubation times ranging from 0-120 min there was no statistical response (no sensitivity) between 100 and 400 mg/dL, suggesting that the system is either enzyme or oxygen-limited at these concentrations. When the hydrogel sensors were incubated in glucose solution for 180 min and 240 min,

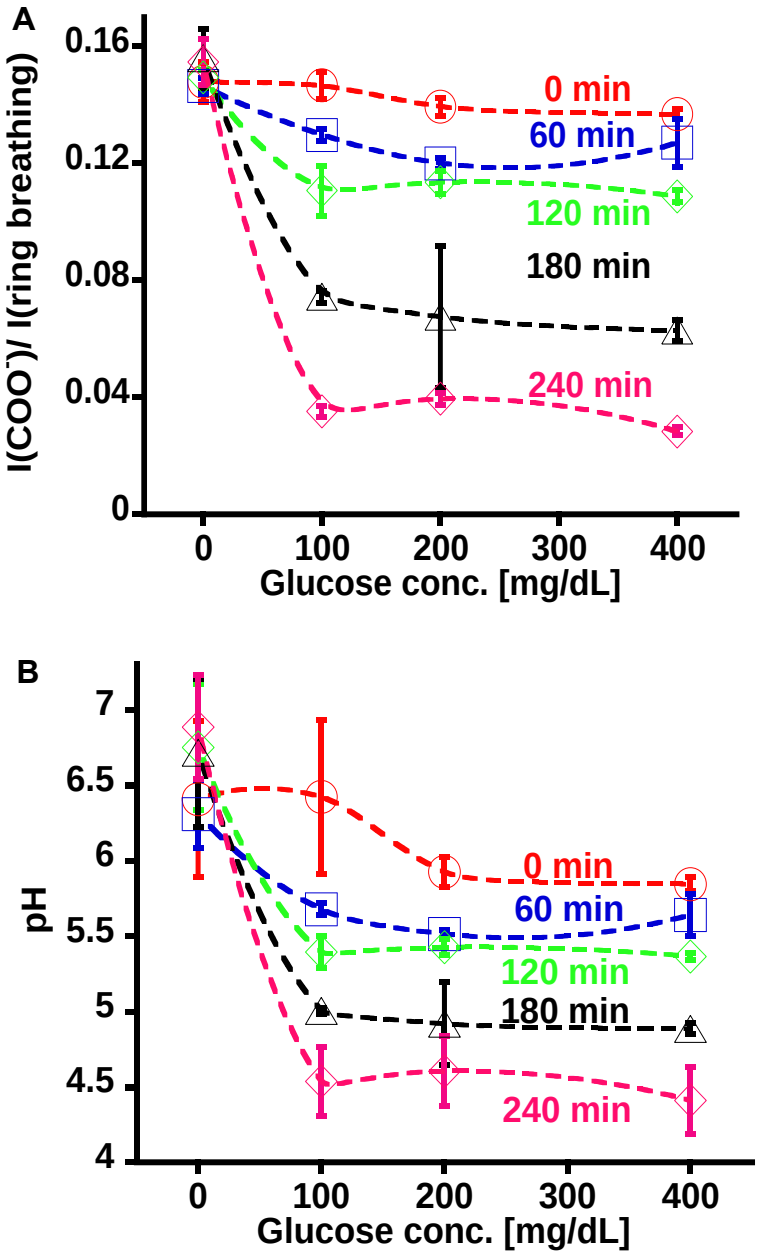

Figure 4-7. Glucose response curves of enzymatic glucose-sensitive hydrogels in 1 mM TRIS buffer containing 10 mM $CaCl_2$ with various glucose concentrations at pH 7.00 as a function of incubation time. (A) Response related to relative intensity ratio of COO- mode relative to the ring breathing mode. (B) Response related pH value in the MC. (n=3: 3 different discs punched from the same hydrogel sensor; pH value was calculated using a pH calibration curve of enzymatic glucose sensing hydrogel; error bars represent one standard deviation).

the pH values drop even further, inducing changes of -57.5 ± 0.4 % (pH 4.89) and -80.8 ± 2.1 % (pH 4.41) of the intensity ratios (relative to baseline) at 400 mg/dL, respectively.

Overall, regardless of incubation time, this embodiment did not exhibit a glucose-dependent response above 100 mg/dL. This was not unexpected, as it is well known that enzymatic reactions become substrate-controlled only under conditions where the supply via diffusion is slower than the reaction involved. In this system, the diffusion coefficient of glucose (D_c) is determined by the PEMs in the glucose sensing hydrogels, which can be described as

$$D_c = \frac{dC}{dt}\left(\frac{bV}{\emptyset}\right)$$

where dc/dt, b, V, and ϕ represent permeability of PEMs to glucose, thickness of PEM, the ratio of glucose solution reservoir volume to PEM area exposed to the solution, and the partition coefficient, respectively. We postulated that ((PDADMAC/PSS)$_5$-(PAH/PSS)$_7$) did not provide enough glucose flux reduction to balance glucose and oxygen supply over this glucose range. Due to the high glucose mass transport through the PEMs, oxygen in microcavities could be completely consumed by the reaction regardless of glucose concentration. As a result, the production rate for gluconic acid depends not on glucose concentration but on enzyme or oxygen concentration. This is consistent with the recent report from Biswas *et al*., which reported that rapid glucose diffusion through PEMs can be controlled by crosslinking ((PDADMAC/PSS)$_5$(PAH/PSS)$_7$) with glutaraldehyde.[110] In that study, the crosslinking of PEMs decreased glucose permeability (dc/dt) by approximately 87 %.

To test this concept in this system, we applied the same crosslinking method to the PEMs in the enzymatic glucose sensing hydrogels. Here, the hydrogels with crosslinked MCs required longer incubation longer to observe noticeable pH decreases. Unlike glucose sensing hydrogels containing uncrosslinked MCs, there was no significant decrease in the SERS intensity ratio of COO^- to ring breathing mode when the crosslinked MCs containing hydrogel sensors were exposed to 400 mg/dL glucose solution (0 min), which means instant pH changes in the MCs were not induced by the glucose oxidation for the hydrogels with crosslinked internal microdomains (Figure 4-8). The unchanged initial pH values suggest that the crosslinking significantly reduces glucose diffusion into the MCs. After 180 min of incubation time, the glucose response curve starts to show a more linear behavior over the entire concentration range. As incubation time is increased further, the glucose sensitivity (absolute value of the slope) becomes larger, inducing much greater drops in pH value. The glucose sensitivity of hydrogel sensors using the crosslinked MCs incubated for 360 min is not only statistically significant over entire glucose concentration (0-400 mg/dL) but also has the largest sensitivity across the entire range amongst all glucose sensing curves.

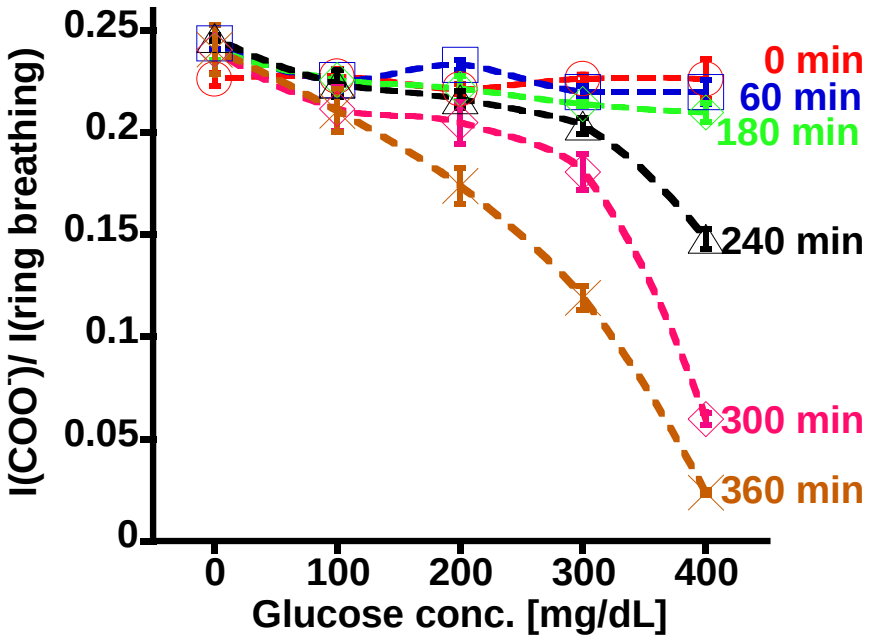

Figure 4-8. Glucose response curves of enzymatic glucose-sensitive hydrogels in 1 mM TRIS buffer containing 10 mM $CaCl_2$ with various glucose concentrations at pH 7.00 as a function of incubation time (n=3: 3 different discs punched from the same hydrogel sensor; error bars represent one standard deviation).

These glucose sensing responses imply that the crosslinked PEMs successfully decrease glucose flux, achieving glucose-limited glucose oxidation in the microcavities. It is recognized that the time periods observed in these steady-state experiments are quite long compared to what might be expected for environmental fluctuations that need to be monitored, nevertheless, these data prove the concept for SERS-based sensing hydrogels with a tunable response to target a desired concentration range, albeit a tradeoff with speed. It is expected that modifying the matrix and PEM permeability will allow optimization of the associated figures of merit. These findings provide a basis for further development and refinement of this sensing platform toward specific applications.

4.5. **Conclusion**

This work successfully demonstrates SERS based sensing via pH sensitive Raman molecule modified gold nanoparticles (MBA-AuNPs) encapsulated within hydrogels, and several important findings are reported first herein. Even when encapsulated within alginate hydrogels, the MBA Raman fingerprint spectral features were detected without signal interference from the hydrogel matrix and capsule materials. Encapsulation results in a shifting of the apparent pKa for the MBA-AuNP, which has implications for future encapsulated nanosensors: the systems cannot be expected to behave exactly as in solution phase, but must be fully characterized for altered behavior. However, the pH-sensing hydrogel still yielded an analytical range (pH 4.43-8.07) that is usable for monitoring many samples of interest, including biological samples and tissue *in vivo*. Further, incorporation of an active enzyme in the same microcavities was demonstrated using the same process, and the resulting materials were shown to effectively induce a pH decrease resulting from the presence of substrate. This proves diffusion of substrate molecules through the hydrogel matrix and into the microcapsules, catalysis (oxidation) driven by the enzyme, and "reporting" of the local pH change by the SERS nanoprobes. Finally, it was proven that crosslinking the microcapsule walls could reduce the flux of substrate into the MCs, slowing the reaction and altering the rate of pH change and, accordingly, the substrate-SERS response profile. Such control of substrate diffusion is essential to tuning enzymatic diffusion-reaction systems to function as sensors. Taken together, these findings represent several

important steps toward a novel SERS sensing platform with great versatility for sensing of aqueous type of samples in many applications.

5. SIZE SELECTIVE AND SERS ACTIVE NANOFILM CAPSULES FOR BIOLOGICAL SPECIMENS*

5.1. **Introduction**

The downside of nanoparticle-based SERS sensors is they often require complicated pretreatment processes in order to detect a biomarker in biological fluids such as urine, serum, and whole blood.[173] Without the pretreatment, proteins in the biological fluids tend to be adsorbed on the nanoparticle surface, excluding the formation of hot spots due to nanoparticle aggregation. In general, centrifugation and sedimentation are utilized to separate such proteins from biological fluids. However, these processes require a large sample volume and relatively expensive instruments. Taner *et al.* eliminated this disadvantageous pretreatment step by conjugating nanoparticles on the porous nitrocellulose matrix of a paper-fluidic device,[174] enabling the detection of glucose in whole blood samples by successfully separating proteins and blood cells. Plasmonic nanoparticles also have been encapsulated in hydrogel microparticles via microfluidic devices to avoid the complex pretreatment step.[73, 175-176] The size exclusion function of this approach was achieved by tuning the mesh size of hydrogel. Moreover, charge selectivity was enabled by varying the functional groups of hydrogel surface. However, these size selective SERS sensing approaches are limited to

*This section is reprinted with permission from "Nanoengineered capsules for selective SERS analysis of biological samples" by You, Y. H.; Schechinger, M.; Locke, A.; Coté, G.; McShane, M., 2018. Proc. Of SPIE, Vol. 10501, 1050103-1, Copyright [2018] by SPIE.

direct SERS detection since plasmonic materials are immobilized at the sensor matrix.

Size selective SERS sensing can be extended to other SERS sensing mechanism such as nanoparticle aggregation based hotspot formation by adopting polymeric capsules. The strength of polymeric capsules is that vacant space in the capsules allows mobile nanoparticles to aggregate upon target binding. In addition, the number of detectable analytes can be increased by modifying nanoparticle surface with various analyte sensitive antibodies, DNA oligomers, and aptamers.[177-179] Jia *et al.* embedded gold nanoparticles (AuNPs) in hollow liposome nanocapsules.[180] Even though porous liposome membranes with size cutoff tunability enabled direct SERS detections in blood plasma, these liposome vesicle template approach is still hindered by low *in situ* nanoparticle loading efficiency. Types of encapsulating materials is also limited with this method since metal nanoparticles are synthesized within the vesicles simultaneously. Recently, we reported the encapsulation of pH sensitive AuNPs in hollow MCs which consist of polyelectrolyte multilayers (PEMs).[109] This encapsulation method is cost effective and generates a high-throughput compared to those using microfluidic devices as well as higher encapsulation efficiency compared to the liposome vesicle template method. Various sensing chemistries has been entrapped with this PEM approach.[120, 172, 181-182] Furthermore, large proteins and blood cells can be sieved by the PEMs. The permeability of PEMs is tunable by controlling the number of multilayers and/or chemical crosslinking of PEMs.[120] In this study, we entrapped aggregation based microRNA-17 (an epigenetic biomarker associated with preeclampsia that exists freely

in the blood) sensing assays in PEM MCs to prove a hypothesis that selective SERS analysis of biological samples will be enabled using tunable permeability of MCs.

5.2. **Experimental**

5.2.1. **Chemicals**

Gold chloride trihydrate, silver nitrate, sodium citrate trihydrate, sodium hydroxide (NaOH), hydroxylamine hydrochloride, sodium carbonate, sodium bicarbonate, poly(diallyldimethylammonium chloride) (PDADMAC, average molecular weight 100-200 kDa), poly(sodium 4-styrenesulfonate) (PSS, average molecular weight 70 kDa), sodium citrate tribasic dihydrate, tris (2-carboxyethyl) phosphine hydrochloride (TCEP), 4-mercaptobenzoic acid (MBA), Rhodamine 6g (Rh6G), bovine serum albumin (BSA), methanol, Dulbecco's phosphate buffered saline (1× PBS), and ethylenediaminetetraacetic acid (EDTA) were obtained from Sigma Aldrich (St. Louis, MO, USA). Malachite green isothiocyanate (MGITC) was purchased from Life Technologies (Carlsbad, CA, USA). Calcium chloride and ethanol (200 proof, USP) were obtained from Decon Labs (King of Prussia, PA, USA). Lyophilized target microRNA-17 and DNA oligomers were synthesized and purchased from Integrated DNA Technologies (Coralville, IA, USA). Upon arrival, DI water was used to suspend the oligomers at a concentration of 100 μM and then were stored at -20 ˚C.

5.2.2. **Assay designs**

In order to detect microRNA-17 (5'-CAA AGU GCU UAC AGU GCA GGU AG-3') two different assays were designed: intensity based and ratiometric sensing assays. The intensity based sensing assay was adapted based on a previous "turn on" sandwich assay developed by Coté's group.[183] In their approach, two batches of silver nanoparticle (28 nm AgNP) were synthesized, one conjugated with Probe 1: 5'-/5ThioMC6-D//iSp18/CTA CCT GCA CTG-3' (a DNA oligomer complimentary to a half of microRNA-17) and the other with Probe 2: 5'-TAA GCA CTT TG/iSp18//iSPC3//3ThioMC3-D/-3' (a DNA oligomer complimentary to the other half of microRNA-17). The AgNP coated with Probe 1 were further functionalized with the Raman dye, malachite green isocyanate (MGITC). The detection assay was then created by mixing the two different batches of AgNPs at a molar ratio of 1:1. In the presence of microRNA-17, the DNA oligomer probes on the surface of the AgNP would bind to the target molecule, microRNA-17, forming nanoparticle aggregates. The formation of aggregates results in the "hot spots" within the narrow gap between two the AgNPs which amplifies the SERS intensity of MGITC within the hot spot. Thus, the assay can be used to determine the target concentration of microRNA-17 based on changes in the relevant SERS intensity.

Furthermore, the addition of a third type of AgNP (i.e. Reference nanoparticle) was used to develop a secondary ratiometric sensing assay (See Figure 5-1A). This new AgNP was modified with a nonspecific DNA oligomer (5'-/5ThoMC-D//iSp18/TTT TTT TTT TTT T-3') and 4-mercaptobenzoic acid (MBA) Raman dye. MBA was chosen

because its Raman bands do not entirely overlap with those of MGITC as shown in Figure 5-1B. The ratiometric sensing assay was designed such that the reference nanoparticle has no inherit binding affinity for the target molecule and thus does not form aggregates in the presence of microRNA-17. As a result, the reference particle provides a SERS signal which is independent of target concentration. The addition of this secondary sensing assay allows for analyte levels to be measured based on ratiometric changes in the SERS intensity between the assay mediated by oligonucleotide hybridization and the uninhibited reference nanoparticle.

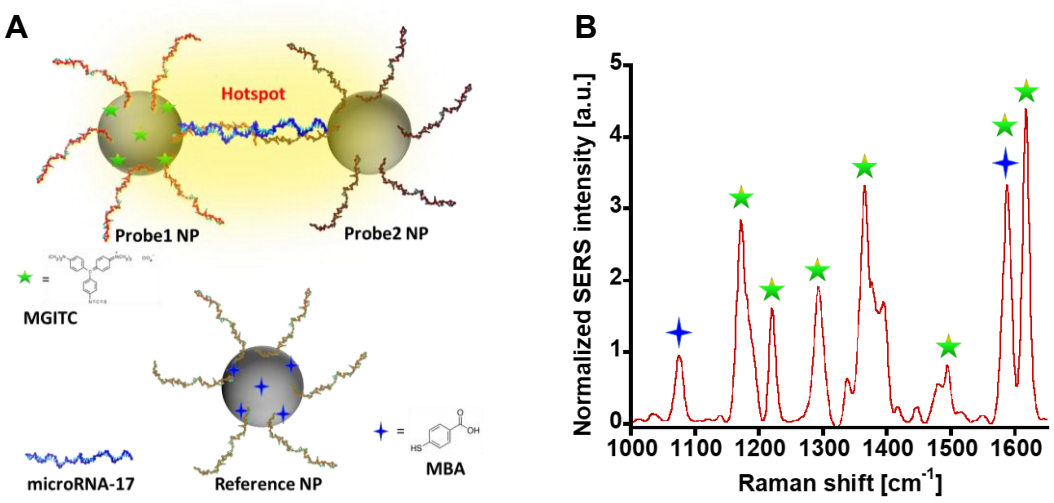

Figure 5-1. (A) Schematic diagram of ratiometric sensing assay. (B) Normalized SERS spectrum of ratiometric sensing assay.

5.2.3. **Nanoparticle synthesis**

The Hydroxylamine (HA) stabilized AgNPs, used to create the microRNA-17 sensing assay, were synthesized using a cold reduction method.[184] Using a 250 mL conical flask, previously cleaned with aqua regia, sodium hydroxide (11.9 mg) and hydroxylamine hydrochloride (10.4 mg) were dissolved in DI water under vigorous stirring. Once dissolved, 10 mM silver nitrate solution (10 mL) was added dropwise into the vortex of the mixture. The solution was kept under vigorous stirring for 15 min. Citric acid capped gold nanoparticles (citric acid-AuNPs), 50 nm in diameter, were also synthesized using a seed mediated method to show the size exclusion function of polyelectrolyte microcapsules.[109]

5.2.4. **Nanoparticle surface modification with DNA oligomers**

DNA oligomers, previously suspended in DI water and frozen for long term storage, were thawed at room temperature (RT) for 30 min. The DNA oligomers were filtered using a 3 kDa centrifugal filter (Nanosep, Pall Laboratory, Port Washington, NY, USA) that were centrifuged at 5000 g. The filtered DNA oligomers were suspended in 1× PBS (at pH 8.50). To enable nanoparticle surface modification, the DNA oligomers were designed to include thiol modifiers synthesized in an oxidized disulfide form. Prior to nanoparticle modification, the disulfide modifier was reduced using 20 mM TCEP. Equivalent volumes of DNA oligomer solution (100 µM) and TCEP (20 mM) were mixed together and then incubated at RT for 1 hr. Residual TCEP and reaction byproducts were removed through filtration using the method previously

described. Following filtration, the reduced DNA oligomers were suspended in 1× PBS at pH 7.40.

Once reduced the DNA oligomers were functionalized on nanoparticle surface by mixing 1 mL of hydroxylamine coated AgNPs with reduced DNA oligomers in a glass vial at a molar ratio of 1:1500 (AgNP to DNA oligomer). The molar ratio was adjusted to 1:3000 to avoid potential nanoparticle aggregations from nonspecific DNA oligomer conjugation. The solution was shaken for 1 hr and then left to incubate at RT overnight. After incubation, 20 µL of sodium citrate buffer (200 mM, at pH 3.00) was added to the solution to promote absorption of the DNA oligomers on the negatively charged nanoparticle surface. This was done three times adding a total of 60 µl of sodium citrate buffer. The solution was then left shaking at RT. After 20 minutes, the sample was centrifuged (20 min, 3300 g) to remove the excess salt and any unbound DNA oligomers. The supernatant containing the waste was removed and the remaining pellet comprised of AgNPs conjugated with DNA oligomer was resuspended in 1 mL of 1× PBS (at pH 7.40).

5.2.5. **Nanoparticle labeling with Raman dyes**

Nanoparticles conjugated with Probe 1 and the reference nanoparticles were further labeled with MGITC and MBA, respectively. Methanolic MGITC (100 µM) was added to 1 mL of conjugated silver nanoparticles at a molar ratio of 1:1000 (AgNP to MGITC). The solution was then left shaking for 1 hr. After which, the nanoparticles solution underwent multiple centrifugations (at 3300 g for 20 min) to thoroughly wash

the sample and remove any excess Raman dye. The sample was stored in 1 mL of 1× PBS (at pH 7.40). With respect to the reference nanoparticles, 100 µL of ethanolic MBA (10 mM) was added to 1 mL of AgNP conjugated with nonspecific DNA oligomer. The solution then underwent the same method described earlier for the solution of nanoparticles conjugated with Probe 1.

5.2.6. **Assay encapsulation in microcapsules (MCs)**

The microcapsules used to encapsulate the nanoparticles were prepared using a calcium carbonate ($CaCO_3$) co-precipitation method.[109] Briefly, 400 µL of AuNPs were mixed with 8 mL sodium carbonate solution (250 mM). Under vigorous stirring, 8 mL of calcium chloride solution (250 mM) was quickly injected into the solution to form the $CaCO_3$ microparticles (MPs). The suspension was stirred for 30 sec before it was left standing for 10 min. Sedimented MPs were collected by centrifugation at 500 g for 30 sec and cleaned with 1 mL of sodium bicarbonate buffer (at pH 8.00).

In regard to the intensity based sensing assay, 500 µL of nanoparticles conjugated with Probe 1 (4.29×10^{-13} moles) and 500 µL of nanoparticles conjugated with Probe 2 (4.29×10^{-13} moles) were encapsulated using the same $CaCO_3$ co-precipitation method described above. A third batch of encapsulated particles were synthesized using a mixture of nanoparticles conjugated with Probe 1, nanoparticles conjugated with Probe 2, and Reference nanoparticles at twice the concentration. The molar ratio of nanoparticles conjugated with Probe 1 to nanoparticles conjugated with Probe 2 to Reference nanoparticle was maintained as 1:1:2.

Following the encapsulation process, the $CaCO_3$ MPs were coated with PEMs (PDADMAC/PSS). A 1 mL volume of MPs was sequentially exposed to cationic PDADMAC suspension and anionic PSS suspension (both polyelectrolytes were dissolved in a 5 mM sodium bicarbonate buffer (at pH 8.00; at a concentration of 20 mg/mL). Between each polyelectrolyte deposition step, the MPs were rinsed with 1 mL of sodium bicarbonate buffer (5 mM). This process was repeated until 10 bilayers of PDADMAC/PSS were achieved. MCs were formed by immersing 30 µL of polyelectrolyte multilayer coated MPs in 15 mL of EDTA suspension (200 mM, at pH 7.00) for 30 min. The resultant MCs were washed with DI water three times and then suspended in 30 µL of buffer.

5.2.7. **UV-Vis measurement**

The size and colloidal stability of the nanoparticles were determined by UV-Vis extinction measurements. The synthesized solutions of citric acid-AuNPs and hydroxylamine capped AgNPs were diluted in DI water by a factor of 10 whereas the AgNPs conjugated with DNA oligomer were diluted by a factor of 10 using 1× PBS (at pH 7.40). In each case, a 100 µL volume of diluted sample solution was added to a single well of 96 well plate (UV-Star, Greiner, Kremsmuenster, Austria) and using an Infinite 200 Pro microplate reader (Tecan, Maennerdorf, Switzerland) the extinction spectra were obtained.

5.2.8. **Scanning electron microscopy (SEM) and energy dispersive X-ray spectroscopy (EDS)**

The solution containing PEM coated were diluted by a factor of 20; meanwhile, the solution containing PEM coated MC was diluted by a factor of 50. Both solutions were diluted using DI water and contained the intensity based sensing assay. 5 µL of the diluted solution was deposited onto a clean piece of Si wafer. The sample was left overnight to dry at room temperature. A DC sputter was used to deposit 2.5 nm of Pt/Pd alloy thin film onto the dried sample. A field emission SEM (JSM-7500F, JEOL, Tokyo, Japan) equipped with an EDS system (Oxford instruments, Abingdon, UK) was used to image the PEM coated MPs and MCs under backscattered electron (BSE) mode. All images and EDS spectra were collected at an acceleration voltage of 20 kV.

5.2.9. **Raman spectroscopy**

The SERS spectra were collected using a Thermo Scientific DXR Raman microscopy (Thermo Scientific, Waltham, MA, USA). The MC size exclusion study was performed using a 780 nm laser at a power of 20 mW. The remaining SERS spectra were collected using a 532 nm laser at a power of 10 mW with the exception of paper devices which used a laser power of 1mW. For all Raman recording, 10 spectra with a collection time of 1 sec were averaged.

5.2.9.1. **Evaluation of size exclusion function of MC**

The protein exclusion ability of the MCs was demonstrated by exposing the MCs which contained the citric acid-AuNPs to either a solution of Raman active Rh6G or a mixture of Rh6G and BSA. The citric acid-AuNPs solution was used as a negative control. The Raman spectra were obtained for three unique samples where each 15 µL of citric acid-AuNPs solution was separately mixed with the same volumes of 20 µM Rh6G, 2 mM BSA, and a mixture of 20 µM Rh6G and 2 mM BSA in three different wells of a 384 well plate. Additionally, 30 µL of citric acid-AuNPs solution was placed in a separate well and used as a control. The three batches of AuNPs containing MCs (30 µL) were resuspended in the same volumes of DI water, 10 µM Rh6G, and a mixture of 10 µM Rh6G and 1 mM BSA. All the solutions prepared were then incubated in the 30 µL wells for 1 hr.

5.2.9.2. **Analysis of sensing assays**

The intensity and ratiometric based sensing assays for microRNA-17 were transferred into a 384 well plate and monitored using a Raman microscopy. For the intensity based sensing assay, nanoparticles conjugated with Probe 1 were mixed with nanoparticles conjugated with Probe 2 at the ratio 1:1 for a total volume of 20 µL. Additionally, 10 µL containing various concentrations of target microRNA-17 in PBS was added to each well. The resultant microRNA-17 concentrations in 30 µL wells were 0, 1, 10, 50, 100, and 500 nM. The same experiment was then performed using the intensity based sensing assay which included 1 mM BSA. The test was performed to

examine how the presence of large protein molecules (i.e. BSA) affects the target dependent nanoparticle aggregation.

The ratiometric sensing assay was prepared by mixing nanoparticles conjugated with Probe 1, nanoparticles conjugated with Probe 2, and Reference nanoparticles for a total volume of 22.5 µL. The 22.5 µL of the ratiometric sensing assay was put into a 30 µL well along with 7.5 µL of target solution resulting previously mentioned microRNA-17 concentrations. Furthermore, 30 µL of previously synthesized MCs were also combined with a solution of microRNA-17 and PBS. All the SERS spectra were obtained after 1 hr of incubation.

5.2.9.3. **Analysis of sensing assays with paper devices**

A paper device was fabricated by adhering a circular nitrocellulose membrane (3 mm diameter; 0.45 µm pore size; Amersham Protran, GE Healthcare Life Science, Marlborough, MA, USA) to a sheet of blotting absorbent paper (Mini Trans-Blot filter paper, Bio-Rad, Hercules, CA, USA) using double sided adhesive tape. The sensing assay was prepared by adding 30 µL of the previously synthesized solution of MCs containing the ratiometric sensing assay (total number of nanoparticles encapsulated in MPs: 1.20×10^{-12} moles) to a solution of microRNA-17 (30 µL; tested concentrations: 0, 1, 10, 50, 100, and 500 nM) with or without 1mM BSA. The resultant sample solution was then incubated for 1 hr. Following the incubation, 2 µL of MCs sample solution was deposited onto the paper device previously described. Due to the size of the MCs in relation to the pore size of the nitrocellulose membrane (0.45 µm), the MCs accumulated

on the surface of nitrocellulose membrane while the remainder of the solution was absorbed by the blotting paper (Figure 5-2). The paper device was dried at room temperature for 10 min.

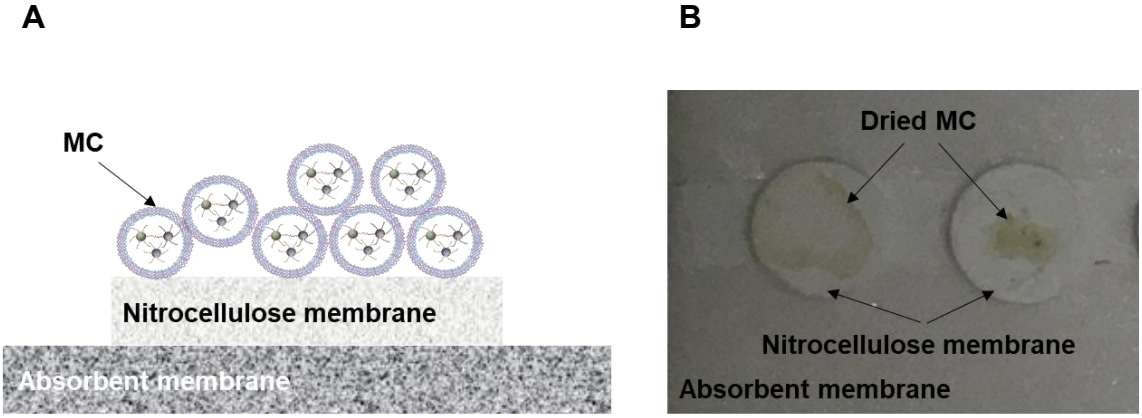

Figure 5-2. (A) Schematic diagram of paper device cross-section and (B) Top view image of paper device.

5.3. **Results and discussion**

5.3.1. **Characterization of nanoparticles**

The SPR wavelength (λ_{max}) of AuNP was located at 529 nm. The size of AuNP was calculated as 50 nm (diameter) based on a method developed by Haiss *et al* [185]. Based on the extinction coefficient at λ=450 nm (9.92×10^9 $M^{-1}\cdot cm^{-1}$), the AuNP concentration calculated using Beer-Lambert's Law was 1.40 nM. The calculated AuNP concentration corresponded to concentration obtained with UV-Vis data.[109] The diameter of the hydroxylamine coated AgNPs (28 nm) was estimated from SPR wavelength (λ_{max}, 405 nm). The silver nanoparticle concentration as 0.85 nM based on the extinction

coefficient of 28 nm, citric acid capped AgNPs (1.15×10^{10} $M^{-1}\cdot cm^{-1}$).[186] The SPR wavelengths for the nanoparticles conjugated with Probe 1, nanoparticles conjugated with Probe 2, and Reference nanoparticles were redshifted to 407 nm, 406 nm, and 408 nm, respectively, due to the DNA oligomers functionalized on the nanoparticle surface (See Figure 5-3A). The use of multiple washing steps during the DNA oligomer conjugation process, reduced the extinction maximums by a factor of 2.5. As seen in Figure 5-3B, there was no shift in SPR following the conjugation of Raman dyes on the nanoparticle surface for both nanoparticles conjugated with Probe 1 and the Reference nanoparticles. Additionally, the absence of secondary surface plasmon resonance peaks in NIR region indicates the solutions of AgNPs conjugated with DNA oligomers are colloidally stable due to the lack of aggregates.

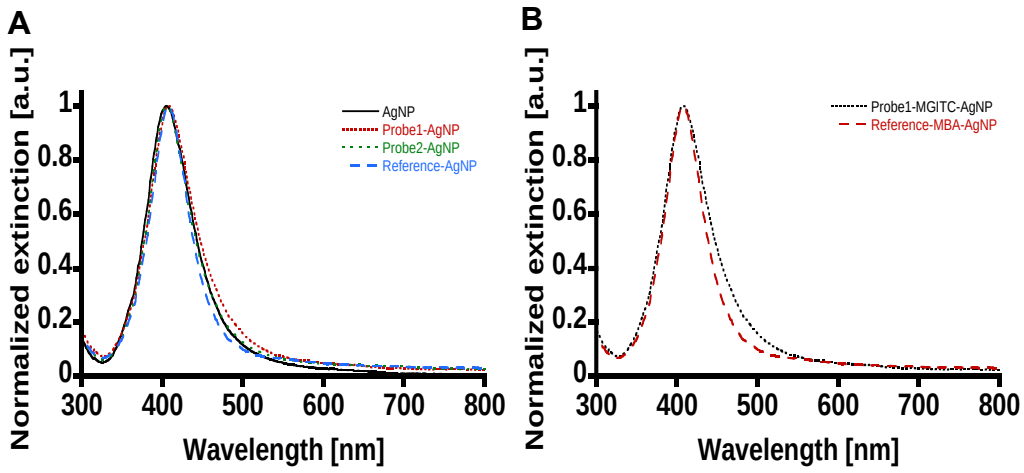

Figure 5-3. (A) UV-vis extinction spectra of hydroxylamine coated AgNP, Probe 1 conjugated nanoparticle, Probe 2 conjugated nanoparticle, and Reference nanoparticle. (B) UV-vis extinction spectra of MGITC labelled Probe 1 conjugated nanoparticle and MBA labelled Reference nanoparticle.

5.3.2. **Physical characterization of nanoparticles embedded MPs and MCs**

The encapsulation of nanoparticles within microstructures was determined using SEM and EDS. The intensity based sensing assay embedded within the PEM coated MPs were observed as spherical structures with fuzzy surfaces and can be seen in Figure 5-4A. The average diameter of the PEM coated MPs was estimated as 4.38 ± 0.45 μm based on the sizing data of 125 PEM coated MPs collected from multiple BSE images (See Figure 5-4B). Successful etching of $CaCO_3$ cores using 200 mM EDTA at pH 7.00 was confirmed based on the hollow MC structures observed in Figure 5-5A. Air drying step during SEM sample preparation resulted in collapsed feature of MC. Unlike PEM coated MPs, heterogenous compositional contrast was observed for the MC when examined under BSE mode. Elements reside in bright regime scattered more backscattered electrons than those in the other regime. In other words, the atomic number of elements in the bright regime is higher than that of elements in the other regime. To specify the type of elements in the bright regime, EDS spectra of the MC were collected from two different spots: one at comparably dark regime and the other at the bright regime as illustrated in Figure 5-5B and C. Both EDS spectra confirmed the presences of PEMs (C/O/S), specimen substrates (Si), and conductive thin films (Pt/Pd) in common. Ag was identified only from EDS spectrum recorded at the bright regime. This substantiates the successful encapsulation of AgNPs within the MCs and the complete etching of $CaCO_3$ cores.

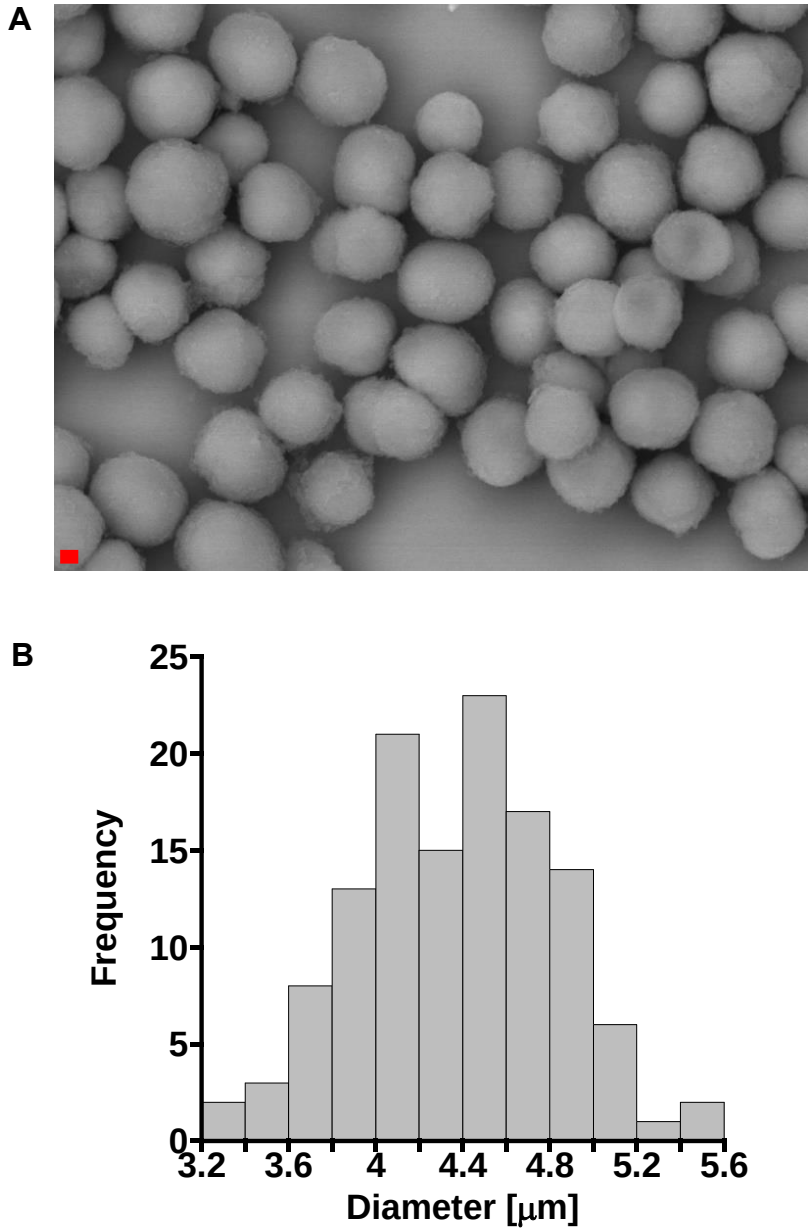

Figure 5-4. (A) BSE image of AgNPs embedded PEM coated MPs (Scale bar represents 1 μm). (B) Size distribution of the same MPs calculated from SEM data.

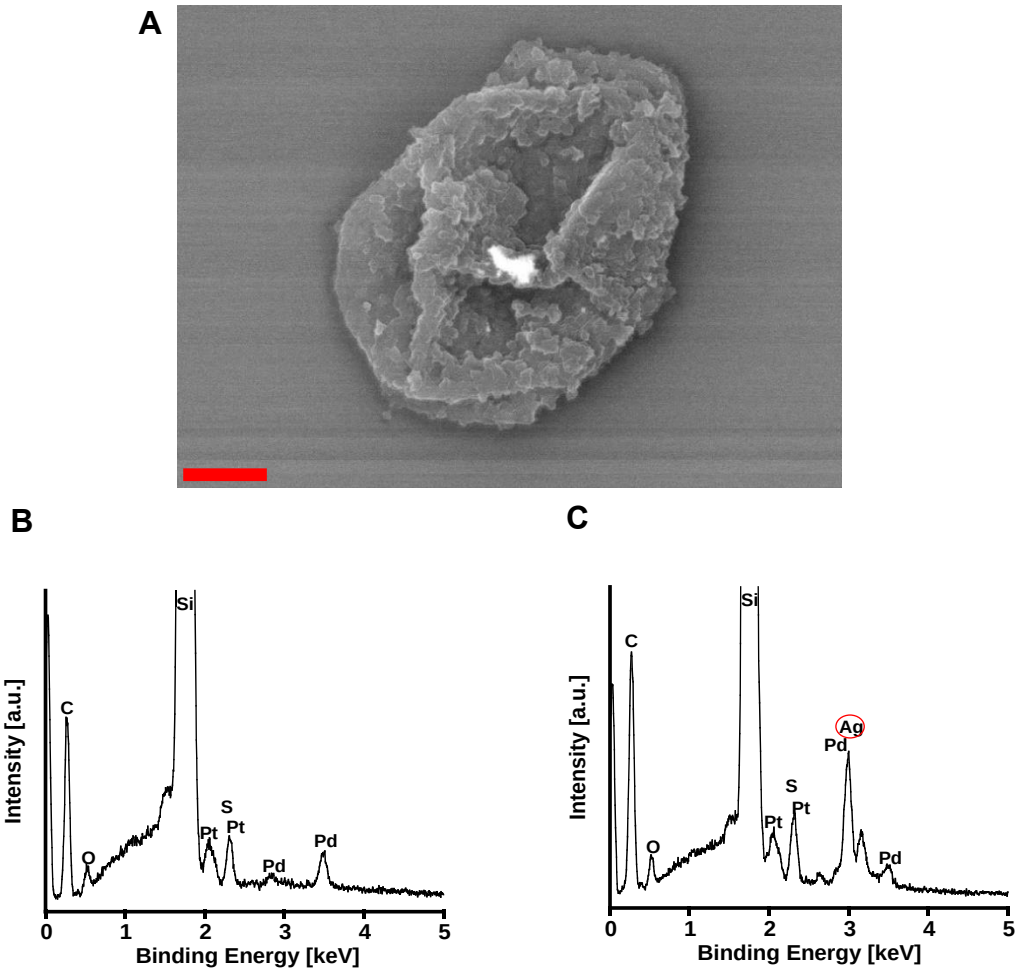

Figure 5-5. BSE image of AgNPs embedded MC (Scale bar represents 1 µm) (A) and EDS spectra of the same MC ((B): dark regime, (C): bright regime).

5.3.3. **Demonstration of size exclusion function of MCs**

The well-established SERS assay for the detection of Rh6G was used to determine the feasibility of the PEM MCs to prevent the diffusion of large protein molecules that can interfere with the SERS signal of metallic nanoparticle assays. This size selectivity function in biological complex media was demonstrated by comparing

direct SERS sensing capabilities of citric acid-capped AuNPs in solution and the same AuNPs embedded in MCs in the presence of Rh6G. As shown in Figure 6A, no significant Raman vibrational bands were detected, from either the stock solution of citric-acid AuNPs or the stock solution mixed with 1 mM BSA. Strong SERS peaks of Rh6G with citric acid-AuNPs were observed; however, those strong SERS bands disappeared with the addition of BSA. These result can be explained by "protein corona" effect.[187] BSA molecules are preferentially absorbed on the surface of metal nanoparticles thus hindering the ability of Rh6G molecules to reach the nanoparticle surface and be detected via SERS. Also, the citric acid-AuNPs embedded in MCs that were introduced to a solution of Rh6G showed noticeable SERS signal as seen in Figure 5-6B, which indicated the passive diffusion of this small molecule into the capsules and absorption on the AuNPs suspended within. However, unlike the free AuNPs, when these MCs were introduced to similar concentration of BSA, the SERS signal was still evident (Green curve in Figure 5-6B), thus indicating the selective exclusion of the larger protein from diffusing through the capsule wall and absorbing on the NPs surface. Therefore, BSA (66.5 kDa) was filtered by PEMs while the target analyte (Rh6G, 479 Da) was able to access AuNPs in the MCs. Albumin and immunoglobulins are known as the most abundant proteins in serums.[188] Since the engineered PEM MCs successfully excluded relatively small albumin proteins, it is believed that the PEMs may protect SERS sensing assays from the interference of complex biological media.

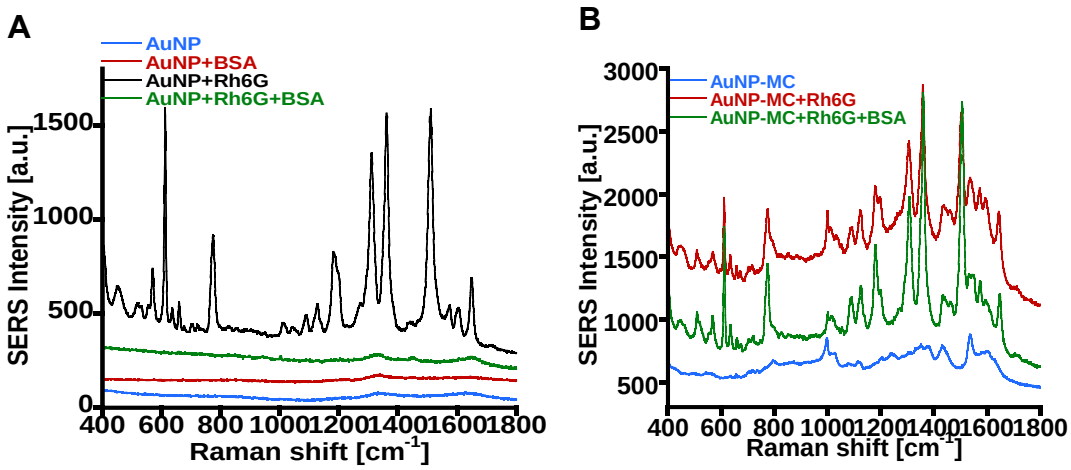

Figure 5-6. (A) SERS spectra of citric acid-AuNPs and those dispersed in an aqueous 1 mM BSA solution, an aqueous 10 µM Rh6G solution, and a mixture of 10 µM Rh6G and 1 mM BSA. (B) SERS spectra of citric acid-AuNPs encapsulating MCs suspended in DI water, an aqueous 10 µM Rh6G solution, and a mixture of 10 µM Rh6G and 1 mM BSA.

5.3.4. **Target sensing with intensity based sensing assay**

Initially, the intensity based sensing assay was tested with various microRNA-17 concentrations (0-500 nM). The characteristic SERS bands of MGITC were confirmed at 1175 cm^{-1} (In-plane ring stretching and bending), 1222 cm^{-1} (N-C stretching), 1295 cm^{-1} (In-plane C-H and C-C-H bending), 1367 cm^{-1} (Aromatic ring stretching), 1590 cm^{-1} (In-plane ring stretching and bending), and 1617 cm^{-1} (Phenyl-N and C-C stretching) from all tested target concentrations.[189] Overall, the addition of the target, microRNA-17, to the sensing assay caused an increase in SERS intensity of MGTIC. Thus, when microRNA-17 is introduced to the sensing assay it successfully undergoes hybridization with both Probe 1 and Probe 2 and forms nanoparticle aggregates as illustrated in Figure

5-7A. The quantitative capacity of the sensing assay was defined by the microRNA-17 concentration dependent calibration curve (See Figure 5-7B) calculated based on the maximum SERS intensity of the peak centered at 1617 cm^{-1}.

Overall, a bell-shaped binding curve was observed for this assay. The largest increase in the SERS intensity occurred at the microRNA-17 concentration range of 0-100 nM where it increased by a factor of 4. The SERS intensity decreased for microRNA-17 concentrations greater than 100 nM. The decreased SERS intensity at 500 nM can be explained by Hook effect which is common amongst sandwich based sensing assays.[177, 190] This effect states that microRNA-17 which exceed the Hook point, the microRNA-17 target concentration at 100 nM, hampers the formation of nano-aggregates since all the potential binding sites, i.e. Probe 1 and Probe 2, are already oversaturated with target molecules. These findings indicate that the designed assay has a specific working range between 0 – 100 nM of microRNA-17. This range can be adjusted by adjusting either the nanoparticle concentration or the ratio of Probe 1 to Probe 2 conjugated on the nanoparticle surface.

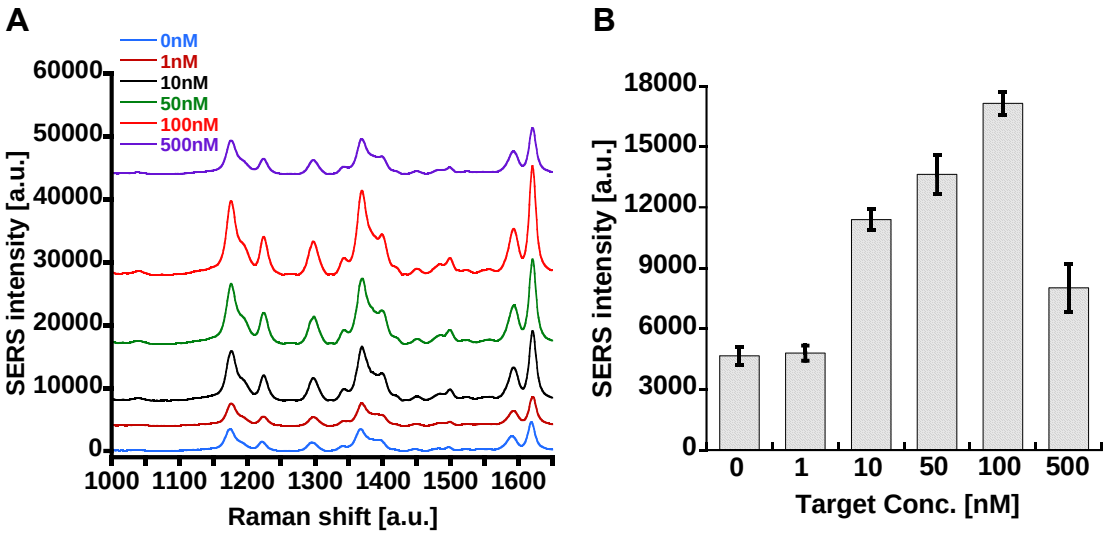

Figure 5-7. (A) SERS spectra of intensity based sensing assay exposed to various target molecule concentrations (0, 1, 10, 50, 100, and 500 nM). (B) A target level dependent calibration curve obtained from the same assay. SERS intensity was calculated at 1617 cm^{-1} (Error bars represent one standard deviations calculated from three different aliquots (n=3)).

The influence of proteins in regard to the sensitivity of the assay, was evaluated by adding BSA to the target solution. The intensity based sensing assay was also exposed to 6 different target concentrations (0, 1, 10, 50, 100, and 500 nM) containing 1 mM BSA. The results showed that with the addition of BSA, the intensity based assay was no longer sensitive to target (Figure 5-8). The BSA introduced to the sensing assay may bind to the available space on the nanoparticles surface where no DNA oligomers and Raman dyes have conjugated. Thus, loss of sensitivity may be attributable to the steric hindrance caused by the absorption of BSA on the nanoparticle surface.

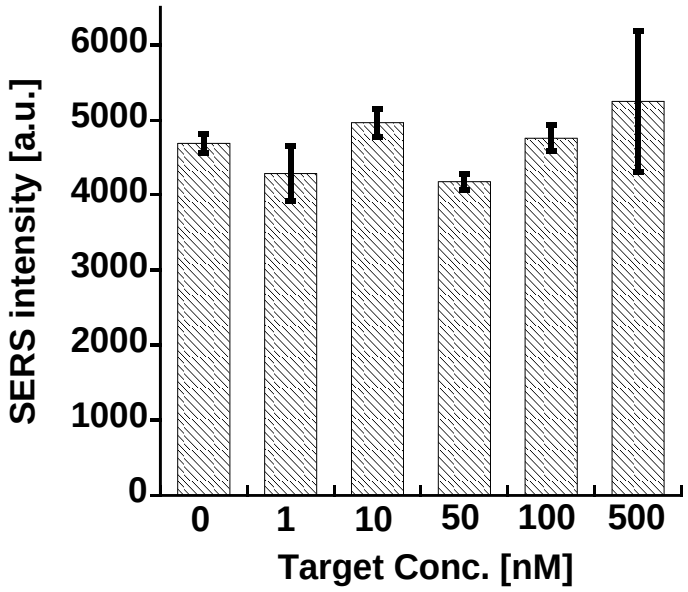

Figure 5-8. A target level dependent calibration curve obtained from intensity based sensing assay exposed to various target concentrations with 1 mM BSA (Error bars represent one standard deviations calculated from three different aliquots (n=3)).

Additional SERS characterization was carried out using the MCs containing the intensity based sensing assay. Even after the encapsulation process, all the characteristic SERS peaks for MGITC were detected from MCs dispersed in 1× PBS solution as illustrated in Figure 5-9A. This means the LSPR around the Probe 1 conjugated nanoparticles was strong enough to selectively enhance the Raman signal of MGITC. Therefore, the MGITC SERS spectra could be sensed overcoming the intensity of randomly scattered light from PEMs. The MC sensing assay also tested to determine its capacity for quantifying microRNA-17 at various concentrations. Unlike the solution

phase assays, there was no statistically significant change in the SERS intensity for the various microRNA-17 target concentrations. These results were determined using a two-tailed t-tests with 95% confidence (α=0.05) (See Figure 5-9B). Considering the diameter of the MCs is 4.38 μm, size may account for this loss in sensitivity as they quickly sedimented within the well of a 384 well plate. During the process where scattered Raman light is collected, the MC was not physically fixated within one focal plane. Thus, the SERS intensity of MGITC is dependent not only on the concentration of the target molecule but also on the mobility of the MC.

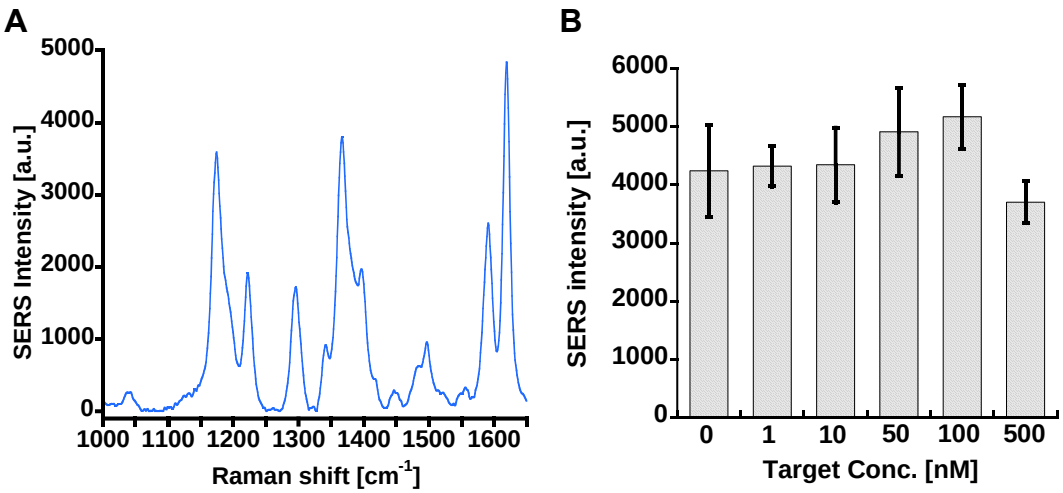

Figure 5-9. (A) A SERS spectrum of intensity based sensing assay encapsulated in MCs. (B) A target level dependent calibration curve obtained from the same MCs exposed to various target molecule concentrations (0, 1, 10, 50, 100, and 500 nM) (Error bars represent one standard deviations calculated from three different aliquots (n=3)).

5.3.5. **Target sensing with ratiometric sensing assay**

To overcome the drawback of using intensity based sensing assay with MCs, a ratiometric based sensing assay was proposed. Reference particles, which are not involved in the formation of aggregates resulting from the presence of the target molecules, were combined with the intensity based sensing assay. The SERS intensity of the Raman dye (MBA) conjugated on the surface of Reference nanoparticle is unaffected by target concentration. The ratio of the SERS intensity of the two Raman dyes (MGITC and MBA) can be used as an improved indicator of target concentration. Assuming all the nanoparticles are uniformly distributed in the MCs, the SERS intensity ratio should not be affected by the migration of the MCs during the SERS measurement. To prove this concept, the microRNA-17 sensing at the assay level was first validated. As illustrated in Figure 5-10A, the MBA conjugated on the Reference nanoparticle produced a SERS peaks at 1075 cm^{-1} that can be distinguished from the SERS spectra of MGITC.

All SERS spectra were normalized to the SERS intensity at 1075 cm^{-1} and were then used to evaluate aggregate formation due to the presence of microRNA-17. The normalized SERS intensity of MGITC increased in the presence of target molecules. A calibration curve was developed by relating the SERS intensity of the peak at 1617 cm^{-1} (Isolated from the SERs spectra for MGITC) to the maximum intensity for the peak at 1075 cm^{-1} (Isolated from the SERS spectra for MBA). The resulting calibration curve produced a similar bell shaped curve to the calibration curve obtained for intensity based sensing assay (See Figure 5-10B).

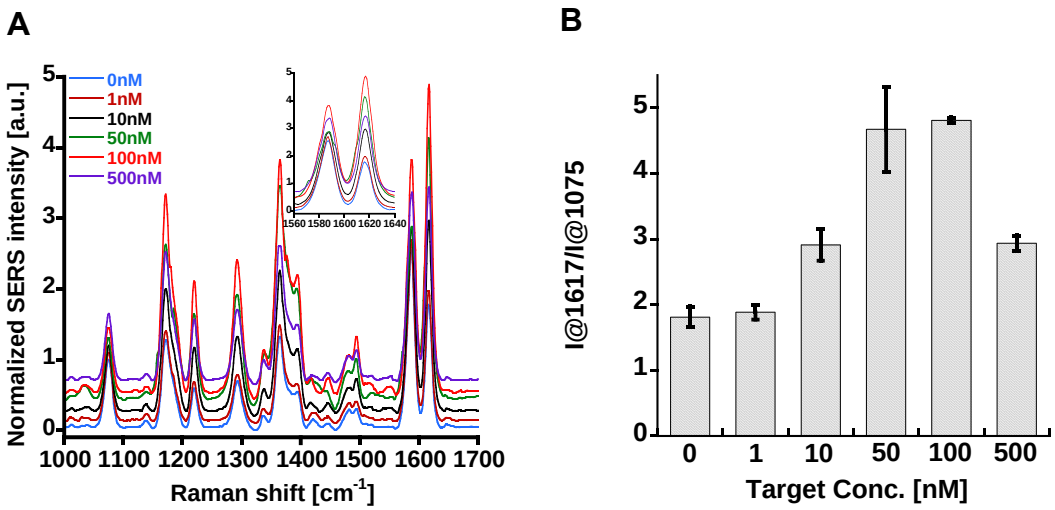

Figure 5-10. (A) Normalized SERS spectra of ratiometric sensing assay exposed to various target molecule concentrations (0, 1, 10, 50, 100, and 500 nM) (Inset: magnified spectra within 1560 to 1640 cm^{-1} range). (B) A target level dependent calibration curve obtained from the same assay. As a signal for this curve the intensity of band at 1617 cm^{-1} relatively to band at 1075 cm^{-1} was calculated (Error bars represent one standard deviation, calculated from three different aliquots (n=3)).

The SERS spectra were collected for the MCs containing the ratiometric sensing assay. The total number of nanoparticles encapsulated in MPs was 1.20×10^{-12} moles. The spectra obtained included all the SERS vibrational bands previously observed in the solution phase assay (See Figure 5-11A). The SERS intensity for the band at 1617 cm^{-1} was calculated relative to the band at 1075 cm^{-1} (I@1617/I@1075) by exposing the MCs to 6 different concentrations of microRNA-17 (Figure 5-11B). Unlike the solution phase assay, the maximum relative SERS intensity was observed with 10 nM instead of 100 nM. Moreover, based on the two-tailed t-test (α=0.05), the relative SERS ratio was only significantly different from the negative control (MCs suspended with 1× PBS solution)

at a target concentration of 10 nM (Hook point). Nikolai *et al.* found that negatively charged quantum dot nanoparticles adsorbed to the positively charged interior PEM MC through electrostatic interaction.[191] In our case, it is highly expected that some of the DNA oligomer conjugated nanoparticles encapsulated in the PEM MC are also deposited on the positively charged inner wall of the PEM MC (PDADMAC). As a result, the concentration of ratiometric assay in the PEM MC may be lower than that in suspension. Such a decrease in assay concentration after being encapsulated in the PEM MC might result in the Hook point shift to a lower target concentration (100 to 10 nM).

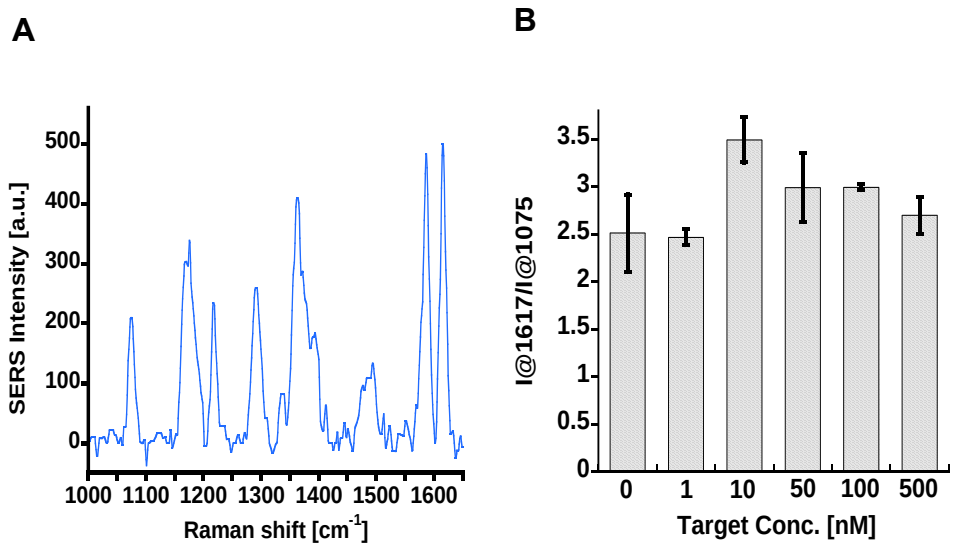

Figure 5-11. A SERS spectrum of ratiometric sensing assay encapsulated in MCs (total volume of nanoparticles encapsulated in MPs: 1050 µL) (A), target level dependent calibration curves obtained from the same type of MCs (Error bars represent one standard deviations calculated from three different aliquots (n=3)).

5.3.6. **Target sensing with paper devices**

The use of MCs to encapsulate the ratiometric sensing assay showed a slight improvement in detecting the target as compared to the MCs containing the intensity based sensing assay. However, the ratiometric sensing assay encapsulated in MCs had a smaller dynamic range compared to the solution phase ratiometric sensing assay. The sedimentation of 30 µL of the MCs in buffer solution placed in a clear well plate was observed within 5 min. This might cause a huge variation in Raman signal of the ratiometric sensing assay overtime as seen in Figure 5-11B. Therefore, we postulate that the sensing capacity of MCs containing ratiometric sensing assay is affected by the mobile nature of the MCs in the buffer solution. To overcome this problem, the MCs can be immobilized in alginate matrix as described in Sections 3 and 4. However, such hydrogel encapsulation method was not adopted for this study since Ca^{2+} ion essential for crosslinking alginate matrix causes non-specific aggregation of microRNA sensing assay. Alternatively, the MCs can be immobilized onto the filter paper substrates. Recently, highly reliable and reproducible SERS sensing with filter paper substrates have been reported.[192-194] Plasmonic nanoparticles can be attached uniformly with a high packing density onto hydrophilic paper devices.[195] In our study, a paper device was used to fixate the MCs on a single laser focal plane during the Raman spectrum measurement. Initially, a raw SERS spectrum of a dried sample of MCs on the paper device but without target was collected. The SERS spectrum was then compared alongside the same MCs dispersed in 1× PBS buffer (at pH 7.40) as well as solution phase ratiometric sensing assay. The data showed that as additional components were added to the

ratiometric sensing assay (i.e. PEMs of MC and nitrocellulose paper) the baseline of the Raman signal increased (See Figure 5-12). This increase in the Raman baseline is likely

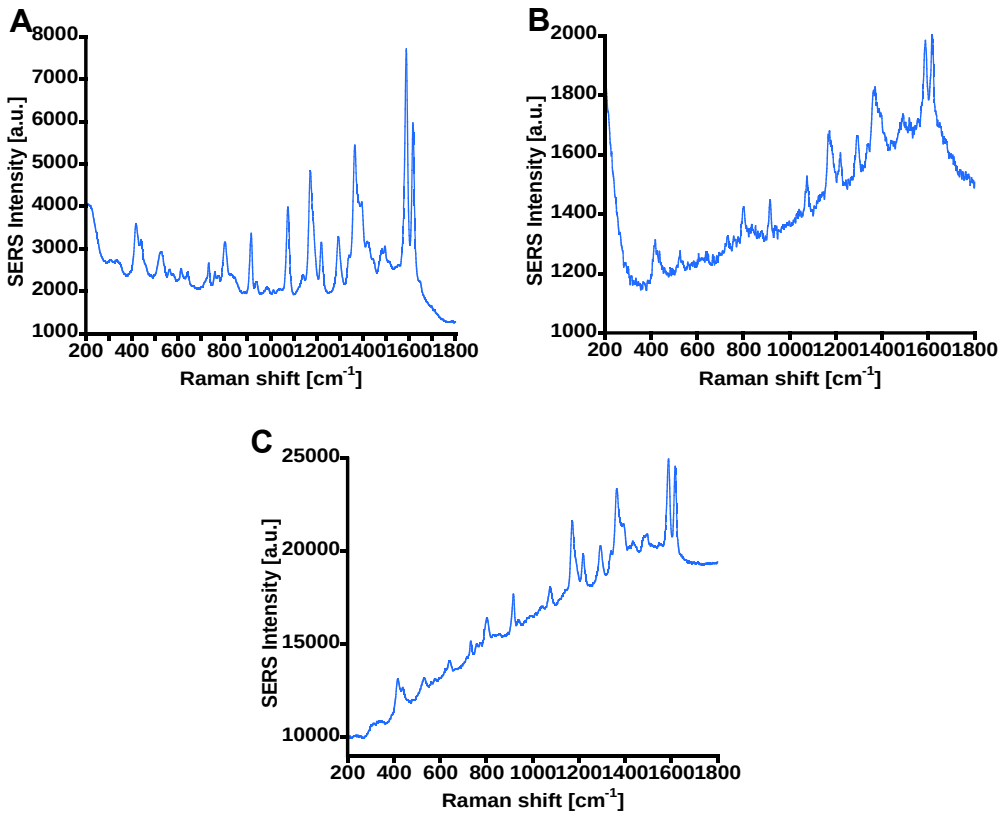

Figure 5-12. Raw SERS spectra of ratiometric sensing assay in different foam factors: free solution (A), MCs in buffer solution (B), and MCs prepared in a paper device (C) 10 mW of laser power was used for the free solution and the MCs samples whereas 1 mW of laser power was used for the paper device).

due to an increase of randomly scattered light created by the PEMs and nitrocellulose paper. Although nitrocellulose paper produces the largest Raman background signal, all

the Raman fingerprints of the ratiometric sensing assay were confirmed with the paper device. It is important to note that the SERS intensity collected using the paper device was obtained using a reduced laser power (1 mW) as compared to the solution based samples (10 mW). Thus, the MCs that were deposited onto the paper device allowed more of the SERS active probes to be exposed to the excited laser as compared to the solution based samples.

Target concentration dependent SERS signals were also collected from the dried MCs (containing ratiometric sensing assay) deposited on the paper devices. Similar to the MCs in solution, the Hook point of the MCs deposited on the paper devices was located at 10 nM (See Figure 5-13A). The results of the MCs deposited on the paper devices were further analyzed using a two-tailed t-test (α=0.05). Such statistical analysis determined that all the target concentrations tested had a relative SERS signals statistically significantly different from the negative control (0 nM of microRNA-17). This improved sensitivity compared to the MCs in solution can be attributed to immobile nature of the MCs with the aid of paper devices. The target sensing of MCs in the paper devices was also evaluated with target solution containing 1 mM BSA to mimic the situation of target sensing in biological complex solution. Figure 5-13B presents a bell shaped curve previous observed in solution phase ratiometric sensing assay. These results indicate that PEM MCs selectively excluded BSA molecules while the microRNA-17 target molecules were able to diffuse through PEM nanofilm and react with embedded ratiometric sensing assay. In the presence of protein molecules, the Hook point of the MCs deposited on paper devices shifted from 10 nM to 100 nM while the

dynamic range was increased to a range of 0 nM to 100 nM. Ladam *et al.* previously reported the interaction between human serum albumin (HAS) and polyelectrolyte multilayers.[196] They showed the formation of albumin film on the PSS terminal layer of PAH/PSS polyelectrolyte multilayers. It may be suggested that albumin layers can be formed onto the PEM MCs in the presence of 1 mM BSA. Such an albumin layer on the PEM MCs can act as a diffusion barrier for the target molecules. Therefore, the change in the dynamic range with the addition of 1 mM BSA can be explained by the decrease in the diffusion rate of target molecule into MCs. Overall, the target level dependent nanoparticle aggregations were formed in the MCs under the presence of signal interfering protein molecules.

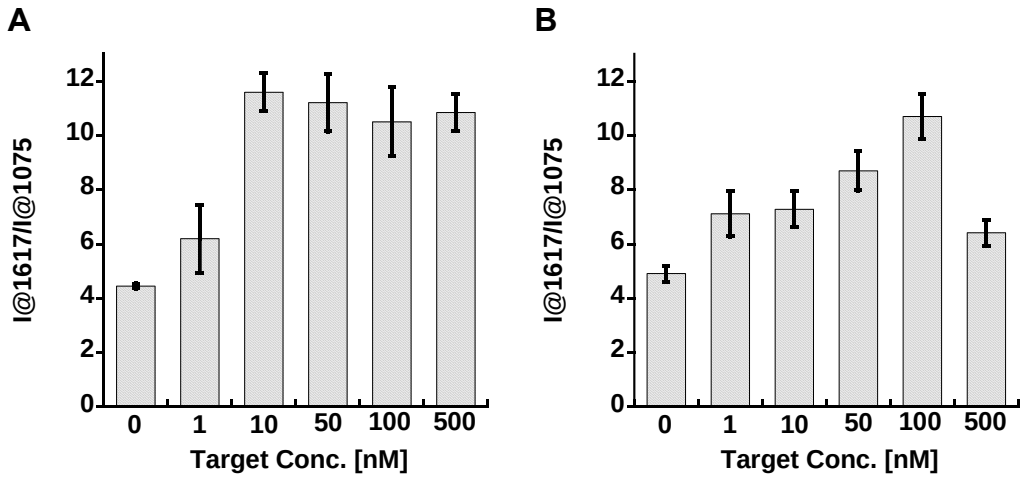

Figure 5-13. Target level dependent calibration curves obtained from MCs prepared in paper devices (without BSA (A) and with BSA (B)) (Error bars represent one standard deviations calculated from three different aliquots (n=3)).

5.4. **Conclusion**

In this work, the potential of MCs in SERS analysis for biological samples was demonstrated by showing the large protein molecule exclusion function of PEMs. This size exclusion ability of the MCs was proven with two separated approaches: direct SERS sensing and aggregation based SERS sensing. The first approach with direct SERS sensing mechanism showed that Raman signal of small Raman molecules in biological fluid can be selectively enhanced by plasmonic nanoparticles embedded in MCs. To prove viability of second approach, intensity based microRNA-17 sensing assay was chosen. This aggregation based SERS sensing assay yielded a bell-shaped calibration curve within the target concentration range of 0-500 nM. When encapsulated in the MCs, however, the assay lost sensitivity. The microRNA-17 sensitivity of MCs containing aggregation based sensing assay was significantly improved by applying ratiometric sensing and paper devices. Moreover, ratiometric sensing assay embedded MCs prepared with paper devices showed target concentration dependent relative SERS intensity changes even in the presence of large protein molecules. Such results suggest that PEM MCs provided not only size exclusion function essential for SERS sensing in biological samples but also vacant space necessary for aggregation based sensing assay to freely interact with target molecules.

6. DEVELOPMENT OF OPTIMIZED EXPERIMENTAL METHOD FOR SERS BASED ADENOSINE SENSING ASSAYS

6.1. **Introduction**

Aggregation based nanoparticle assays are an attractive approach to sense small molecules since they provide exceptional sensitivity by controlling hotspot. As nanoparticles are aggregated, the local electromagnetic field between the nanoparticles are enhanced extensively. Therefore, when a Raman active small molecule is placed in the enhanced local electromagnetic, "hot spot", the Raman signal of the molecule can be amplified by 10^6 to 10^{11}.[197] In addition, a controlled formation of hotspots can be achieved by combination of an aggregation based nanoparticle assay and the use of ligands such as antibodies,[198-199] hybridization based oligonucleotides,[179, 183] and aptamers.[200-201] Most of the previous studies on aggregation based nanoparticle assays focused on developing colorimetric sensors based on irreversible nanoparticle aggregation.[200, 202-203] However, a controlled reversible nanoparticle aggregation is essential for an implantable hydrogel platform and continuous monitoring.

To achieve this, aptamer-conjugated metal nanoparticles can be encapsulated in microdomains distributed in hydrogel matrix. The use of aptamers as a ligand for aggregation based nanoparticle assay has two main advantages. Firstly, aptamers possess a higher chemical stability compared to antibodies, which results in longer retention of target sensitivity. Secondly, with the aid of systematic evolution of ligands by exponential enrichment (SELEX),[204] the aptamers can bind to a variety of target

molecules including small molecules, macromolecules, and cells.[205-206] This means that the number of detectable analytes with hydrogel based sensors can be increased extensively as long as analyte specific aptamers are developed. The aptamer-conjugated metal nanoparticles localized in a free volume of microcapsules can be reversibly aggregated, due to conformational change of aptamers induced by aptamer-analyte binding when the analytes selectively diffuse into the microdomain (See Figure 6-1).

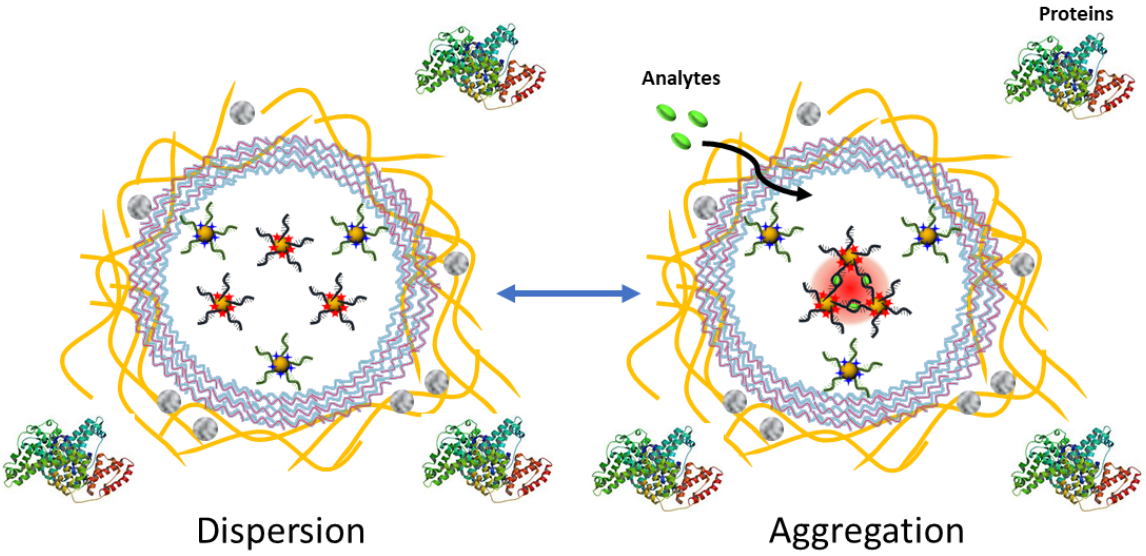

Figure 6-1. Schematic diagram of reversible aggregation of aptamer conjugated metal nanoparticles a microdomain.

Split aptamer-based sandwich assay can be a good model assay to show reversible aggregation of nanoparticle assays in the microdomains. Adoption of split aptamer in aggregation based nanoparticle assays can reduce steric hinderance and

unintended conformational changes which hamper target sensitivity and selectivity.[207] In this study, we choose adenosine sensitive split aptamers designed by Li *et al*. to build a SERS based aggregation assay.[208] We also implemented several aptamer conjugation protocols proposed by other groups to optimize the adenosine induced hot spot generation.[209-210] In addition, by testing multiple aptamer conjugation methods for the same sensing assay, we tried to explore the correlation between the analyte sensing performance and the selection of conjugation protocols.

6.2. **Experimental section**

In order to investigate the experiment of aptamer based analyte detection, we choose adenosine sensing assay developed by Li *et al*. as a model assay.[208] This assay utilizes two split aptamers which are divided from a single aptamer of adenosine. The adenosine sensing with this assay have been reproduced by other researchers such as Yang *et al*.[209] and Heo *et al*. (Lee group).[210] Initially, for aptamer conjugation, the protocol used for microRNA-17 sensing assay from Section 5 (Graham method) was adopted. Secondly, we obtained a protocol according to our understanding of the experimental section written by Heo *et al*. (Lee method). Finally, we received a modified protocol with more details directly from Lee group (Modified Lee method). Total four different aptamer conjugation methods were tested in this study.

6.2.1. **Chemicals**

Sodium citrate tribasic dihydrate, gold chloride trihydrate, tris(hydroxymethyl)aminomethane hydrochloride (Trizma HCl), sodium chloride (NaCl), tris(hydroxymethyl)aminomethane (Trizma base), sodium hydroxide (NaOH), tris(hydroxymethyl)aminomethane acetate salt (Trizma acetate), sodium acetate, sodium carbonate, sodium bicarbonate, acetic acid, tris (2-carboxyethyl) phosphine hydrochloride (TCEP), Dulbecco's phosphate buffered saline (1× PBS), ethylenediaminetetraacetic acid (EDTA), methanol, poly(diallyldimethylammonium chloride) (PDADMAC, average molecular weight 100-200 kDa), poly(sodium 4-styrenesulfonate) (PSS, average molecular weight 70 kDa), and glacial acetic acid were obtained from Sigma Aldrich (St. Louis, MO, USA). Ethanol (200 proof, USP), hydrochloric acid (HCl), and calcium chloride ($CaCl_2$) were purchased from Decon Labs (King of Prussia, PA, USA). Malachite green isothiocyanate (MGITC) was obtained from Life Technologies (Carlsbad, CA, USA).

6.2.2. **Aptamers**

Three types of aptamer were used for adenosine binding study. Two of aptamers were split aptamers which bind to adenosine: DNA1(5'-/5ThoMC-D/poly T spacer/ACC TGG GGG AGT AT-3') and DNA2 (5'-/5ThoMC-D/poly T spacer/TGC GGA GGA AGG T-3'). Poly T spacer was either TTT TT (T_5) or TTT TTT TTT T (T_{10}). The third aptamer was nonspecific aptamer (DNA3: 5'-/5ThoMC-D/TTT TTT TTT T-3') which was designed for nanoparticle stability improvement.

Aptamers used with Graham and Lee methods were purchased from Integrated DNA Technologies (Coralville, IA, USA). As received, the aptamers were suspended DI water at a concentration of either 100 µM (Graham method) or 1 mM (Lee method) and then were frozen at -20 ˚C for long term storage. Aptamers used with modified Lee method were obtained from Bioneer (Daejeon, South Korea). As synthesized, the aptamers were purified via high performance liquid chromatography (HPLC). Upon arrival, aptamer container was centrifuged at 10 kg for 1 sec to collect residual aptamers absorbed on the container wall. The pallet of aptamer at the bottom of container were dissolved in DI water at a concentration of 1 mM. The aptamer solution was incubated at 90 for 1 hr to unfold aptamer stands. The incubated solution was cooled down at RT and then stored at 4 ˚C.

6.2.3. **Instrumentations**

We recorded extinction spectra via an Infinite 200 Pro microplate reader (Tecan, Maennerdorf, Switzerland). The solution samples for extinction measurement were prepared in the wells of UV clear 96 well plate (total volume of 100 µL). We collected SERS spectra using either a bench top Raman system (DXR Raman, Thermo Scientific, Waltham, MA, USA) or a held hand Raman system (IDRaman mini 2.0, Ocean Optics, Largo, FL, USA) equipped with a raster orbital scanning mode. Adenosine sensing assays for SERS measurements were injected into the wells of a 384 well plate. A 532nm laser with a laser power of 10 mW was used for the bench top Raman system whereas the portable Raman system utilized a 632 nm laser with a laser power of 50

mW. SERS spectra with 3 sec of collection time were recorded five times and then averaged.

6.2.4. **Nanoparticle synthesis**

We synthesized gold nanoparticles (AuNPs) with two different diameters (14 and 45 nm) using citric acid reduction method. 14 nm AuNPs were synthesized using a modified Frens method.[211] Briefly, Aqua regia was poured in a 250 mL three neck flask with a triangular magnetic stirring bar. The solution was kept stirring for 5 min and then the flask was rinsed with DI water 10 times. 100 mL of 1 mM gold chloride trihydrate was placed in the cleaned three neck flask. The solution was heated with the heating mantle with refluxing. As soon as bubbles come out, 38.8 mM sodium citrate tribasic dihydrate (10 mL) was injected into the solution. After 10 min of stirring, the flask was taken out from the heating mantle. The solution was cooled down at RT and then stored at 4 ˚C. 45 nm AuNPs were synthesized using the same seed mediated method described in Sections 3, 4, and 5. In this study, gold nano-shell coating was stopped after 45 nm diameter was achieved.

6.2.5. **AuNP surface modification with aptamers**

6.2.5.1. **Graham method**

Frozen 100 µM aptamer solution was thawed at RT for 30 min. Using a 3 kDa centrifugal filter solution media was changed from DI to 1× PBS at pH 8.50 as described in Section 5. To reduce disulfide groups in aptamers (5ThoMC-D), 100 µL of aptamers

in PBS was mixed with the same volume of 20 mM TCEP solution followed by 1 hr of incubation at RT. We removed reaction byproducts and residual TCEP by filtering reduced aptamer solution with the same centrifugal filter used for buffer change (centrifugation speed: 5000 g). The resultant aptamers were washed with DI water three times and then resuspended in 100 µL of 1× PBS at pH 7.40. The reduced aptamer solution was heated in the water bath (90 ˚C) for 5 min to stretch folded aptamer strands.

In this work, two sets of adenosine sensing assay were prepared: one with nonspecific aptamer (DNA3) and the other without DNA3. 1 mL of citric acid capped AuNPs (citric acid-AuNPs) were transferred in a glass vial and further mixed with reduced adenosine sensitive split aptamers (either DNA1 or DNA2) at a molar ratio of 1:200. For the adenosine sensing assay with nonspecific aptamers, the same moles of DNA3 aptamers were added to the mixture of citric acid-AuNPs and split aptamers. The mixture was shaken for 1hr and then incubated in a dark room overnight. To increase the efficiency of aptamer chemisorption on the AuNP surface, 20 µL of 0.2 M sodium citrate tribasic solution at pH 3.00 were added into the incubated solution 3 times followed by 20 min of shaking. The nanoparticles were washed with 1× PBS at pH 7.40 via three consecutive centrifugations (16.0 kg for 15 min). The final agglomerates composed of aptamer capped AuNPs were dispersed in 1 mL of buffer (either 1× PBS at pH 7.40 or 25 mM Tris buffer at pH 8.20 containing 300 mM NaCl).

6.2.5.2. **Lee method**

We thawed 1 mM aptamer solutions at RT for 30 min. In a 15 mL centrifuge tube, 1mM adenosine sensitive split aptamers in DI (9 µL) were mixed with 0.5 M sodium acetate buffer at pH 5.20 (1 µL). Into the mixture, 3 µL of 10 mM TCEP solution was added and the mixture was further incubated for 1 hr to activate the dithiol groups in the aptamers. 3 mL of 14 nm citric acid- AuNPs was dropped into the mixture slowly, yielding a molar ratio of citric acid-AuNPs to aptamers as 1:231. The solution was stored at RT in the dark overnight. 100 µL of 1 M NaCl solution was added into the solution three times followed by 10 sec of sonication. The solution kept in the dark room for 24 hr. Final aptamer conjugated AuNPs were cleaned as mentioned in Graham method and then redispersed in 25 mM Tris acetate buffers.

6.2.5.3. **Modified Lee method**

The method that we are describing in this section is an updated aptamer conjugation protocol provided from Lee group. This method contains more experimental details and knowhows, which are quite difficult to be delivered through a research paper. Apart from unique aptamer preparation step, chemicals such as buffer solutions were specially prepared. The pH of sodium acetate buffer solution was titrated only with acetic acid. Tris acetate buffer mentioned in their paper was tris buffer solution titrated by acetic acid. The other vague experimental details from the paper was salt treatment. Before the injection of 1M NaCl solution, 30 µL of 0.5 M Tris buffer at pH 8.20 was added into the mixture of citric acid-AuNPs and aptamers. After shaking gently, the

solution was sonicated for 10 sec. After this Tris buffer addition, the solution was further treated with 1 M NaCl as described in Lee method but there was 20 min of time interval between the salt injections.

6.2.6. **AuNP surface modification with Raman dyes**

AuNPs conjugated with DNA2 prepared using modified Lee method were labeled with MGITC. Briefly, methanolic 10 µM MGITC solution was mixed with DNA2 conjugated AuNPs (1 mL) at molar ratios of 1:250 and 1:500 (AuNP to MGITC). The mixture was immediately shaken for 1 hr in a glass vial. To sperate residual methanol and excess MGITC, we washed the nanoparticles three times with DI water via centrifugation and redispersion steps.

6.2.7. **Adenosine binding test**

In case of analyte binding test for Graham, and Lee methods, 45 µL of DNA1 conjugated AuNPs were mixed with the same volume of DNA2 conjugated AuNPs in a well of a 96 well UV clear well plate. 10 µL of adenosine stock solution (0, 0.1, 0.5, 1, 5, 10, 25, and 50 mM) was added in to the solution. The mixture was pipetted multiple times in the well and then incubated for 1 hr. For adenosine binding test with the assay prepared with modified Lee method, DNA1 conjugated AuNPs (90 µL) were mixed with DNA2 conjugated AuNPs (90 µL) in a glass vial. After adding 20 µL of adenosine stock solution (0, 10, and 50 mM) into the mixture, the solution was kept in dark for either 2 or 24 hr.

6.3. **Results**

6.3.1. **Characterization of citric acid-AuNPs**

Two batches of citric acid-AuNPs were synthesized using two different methods: Frens method and seed mediated method. UV-Vis was utilized to determine their sizes and concentrations. Blue and red spectra in Figure 6-2 were recorded from citric acid-AuNPs synthesized using Frens method and seed mediated method, respectively. The SPR peaks for samples prepared using Frens method and seed mediated method were found at 518.5 and 525 nm, respectively. Based on the same size estimation method used in Sections 3 and 4, diameters of AuNPs synthesized using Frens method and seed mediated method were estimated as 14 and 45 nm, respectively. The extinction coefficients at 450 nm used for AuNP concentration calculation were 1.76×10^{8} and 7.13×10^{9} $M^{-1}cm^{-1}$ for 14 and 45 nm citric acid-AuNPs, respectively. Using Beer's law, we estimated nanoparticle concentrations of 14 and 45 nm AuNPs as 6.19 and 0.16 nM, respectively.

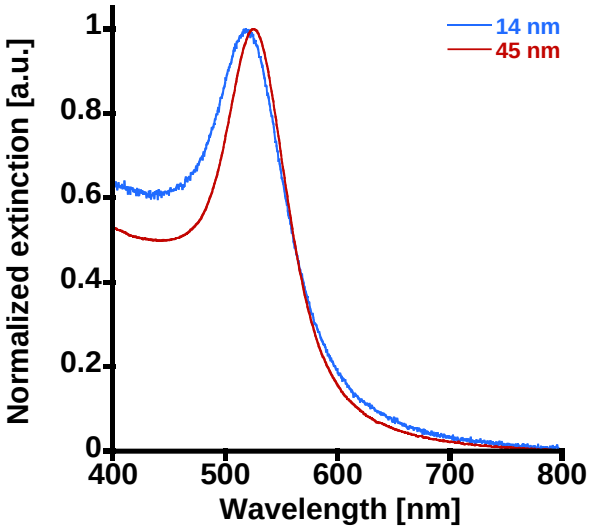

Figure 6-2. UV-vis spectra of citric acid-AuNPs synthesized with Frens (Blue curve) and seed meditated methods (Red curve).

6.3.2. **Adenosine binding test with the samples prepared with Graham method**

For this study 14 nm AuNPs were conjugated with adenosine sensitive aptamer fragments (DNA1 or DNA2) to construct a sandwich assay. Resultant AuNPs were further conjugated with DNA3 to improve colloidal stability. In the presence of adenosine, structural changes of aptamers induced the formation of aggregation between AuNPs conjugated with DNA1/DNA3 (DNA1/DNA3-AuNPs) and AuNPs conjugated with DNA2/DNA3 (DNA2/DNA3-AuNPs). Such interparticle distance change influences the optical properties of the adenosine sensing assay. For example, SPR peak is red shifted as the interparticle distance decreases. In addition, extinction in the wavelength ranging from 600 to 700 nm increases with the decrease in the interparticle distance.[212]

As shown in Figure 6-3A, the change of extinction spectrum was not observed when the mixture of DNA1/DNA3-AuNPs and DNA2/DNA3-AuNPs were exposed to various concentrations of adenosine (0 - 1 mM) in 1× PBS at pH 7.4. Even though we incubated the adenosine sensing assays with target molecules 30 min longer (total 1hr) than what Li *et al*. showed, the nanoparticle aggregation due to adenosine binding was not discernible from extinction spectra. In order to quantitatively evaluate adenosine concentration dependent nanoparticle aggregation, we calculated the ratio of extinction at 650 nm to extinction at SPR peak (A@650/A@SPR). The more degree of aggregation due to adenosine binding, the more A@650/A@SPR. Li *et al*. reported that the A@650/A@SPR increased approximately from 0.10 to 0.28 when adenosine concentration was varied from 0 to 1 mM. However, our results did not show any significant extinction ratio changes from a negative control (the extinction ratio at 0 mM) over the entire adenosine concentration range (See Figure 6-3B).

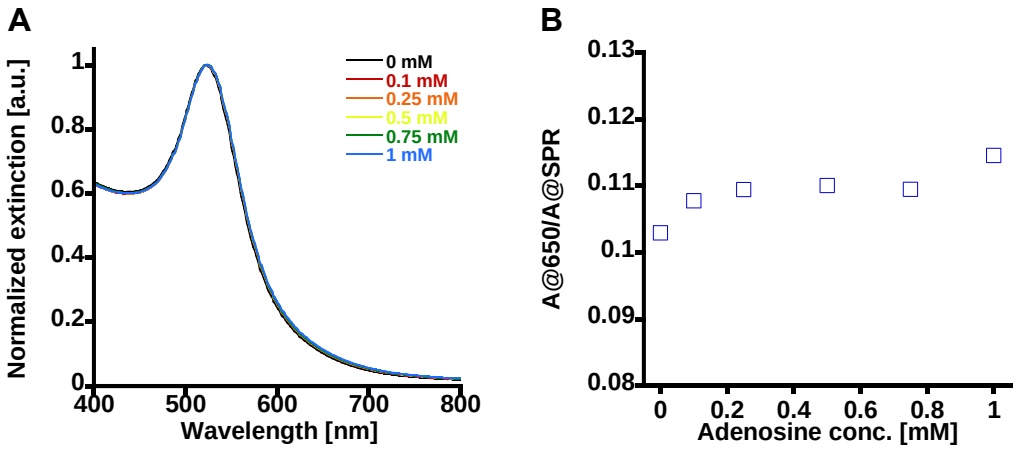

Figure 6-3. (A) UV-vis spectra of adenosine sensing assay composed of DNA1/DNA3-AuNPs and DNA2/DNA3-AuNPs as a function of adenosine concentration (0 - 1 mM). (B) A calibration curve of adenosine sensing with the same sensing assay.

To improve adenosine sensitivity, we varied several important experimental factors. Firstly, we prepared adenosine sensing assays with 25 mM Tris buffer at pH 8.20 containing 300 mM NaCl following Li *et al*.'s protocol (Figure 6-4 A and B). Secondly, the adenosine sensing assays were synthesized omitting aptamer unfolding step which Li *et al*. did not perform. Such adenosine assay was dispersed in Tris buffer solution and tested with different adenosine concentrations to study how additional heating process (unfolding) affects adenosine sensitivity (Figure 6-4 C and D). Lastly, nonspecific aptamers (DNA3) were removed from adenosine sensing assays to decrease surface charge of nanoparticle probes (Figure 6-4 E and F). We postulate that reduced electrostatic repulsion between two adenosine sensitive AuNPs facilitates the formation of nanoparticle aggregation. However, any of these experimental variables did not affect the adenosine sensitivity based on our UV-Vis studies.

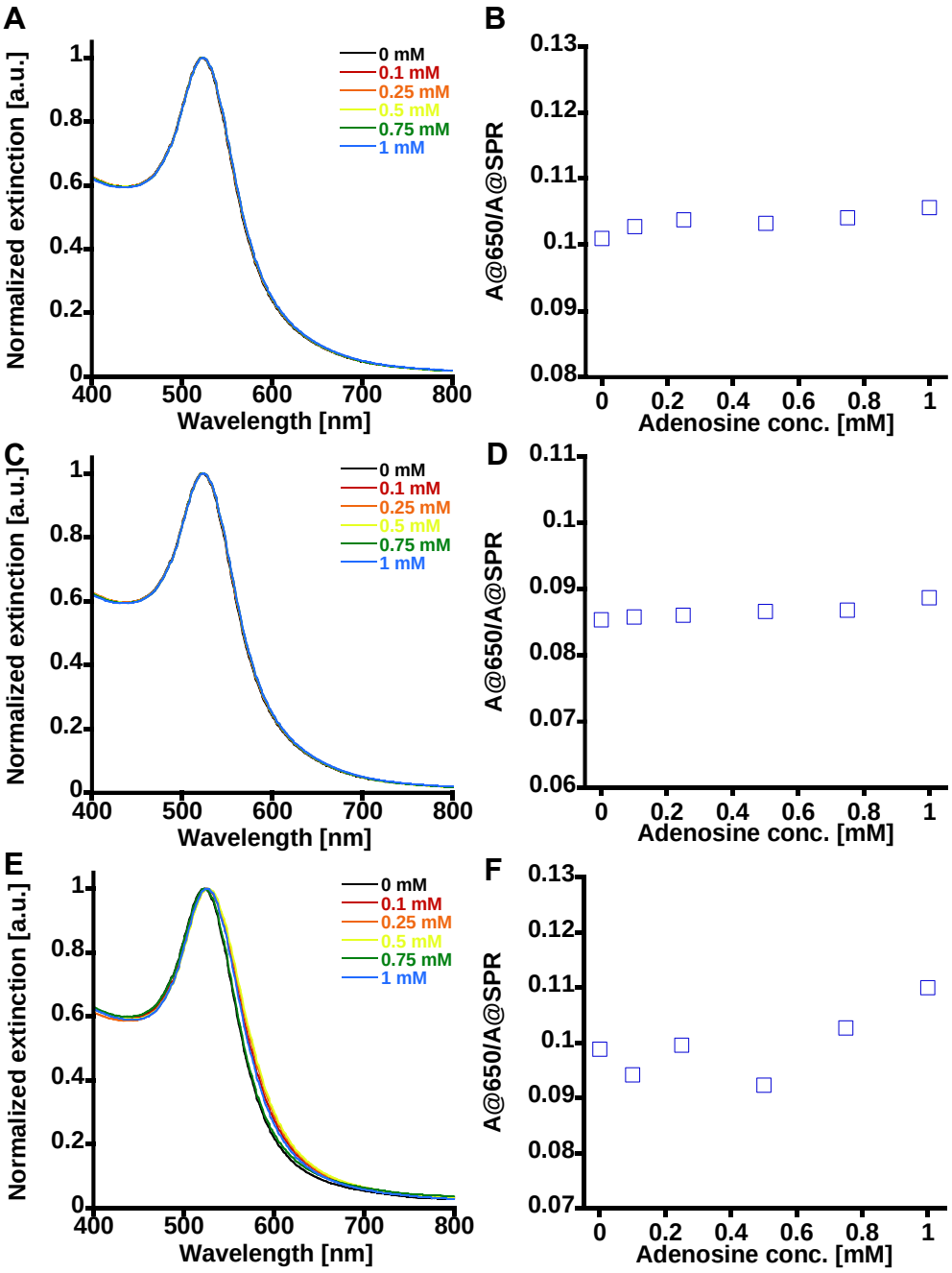

Figure 6-4. Comparison of UV-Vis spectra and adenosine concentration dependent calibration curves with tuning of experimental factors in the Graham method.

6.3.3. **Adenosine binding test with the samples prepared with Lee method**

The adenosine sensing with the assay prepared with 10T linker based aptamers using Lee method showed a similar target insensitive trend compared to our previous trials. As described in Figure 6-5, when adenosine concentration was increased from 0 to 5 mM, SPR peak was shifted from 524 to 526 nm. The range of A@650/A@SPR within tested adenosine concentrations (the extinction ratio difference between minimum and maximum target concentrations) was 0.011, which was not significantly different from the adenosine sensing data with other synthesis methods.

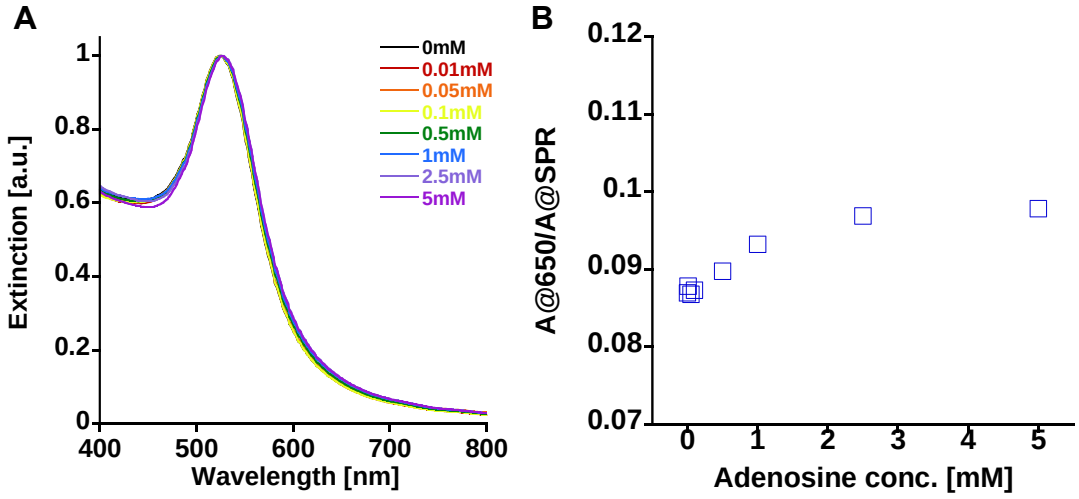

Figure 6-5. UV-Vis spectra (A) and a calibration curve (B) of adenosine sensing assays prepared with 10T linkers using Lee method.

To further investigate the effect of aptamer linker length on target sensitivity, we reduced the length of aptamer linker from 10T to 5T. Moreover, Lee group also used 5T linkers rather than 10T linkers for their aptamer assay design. The reduced linker length can decrease the degree of steric hindrance of adenosine sensitive AuNPs. When the adenosine sensitive AuNPs form aggregates in the presence of target molecules, they need to overcome steric hinderance which acts as interparticle repulsive force.[213] Therefore, the adenosine sensitivity can be ameliorated by reducing aptamer linker length. Figure 6-6A exhibits slight spectral changes with an increase in target concentration. The SPR peak location was redshifted by 5 nm with 5 mM adenosine compared to a negative control. The extinction of 600 - 700 nm was also slightly elevated, indicating the formation of AuNP aggregates. In addition, we observed an upward trend in A@650/A@SPR as adenosine concentration was increased (Figure 6-6B). The range of A@650/A@SPR for the adenosine sensing assays prepared with 5T aptamer linkers (0.023) was approximately twice as high as that for the adenosine sensing assays prepared with 10 T aptamer linkers. Such improved adenosine sensitivity achieved with Lee method was higher than any other methods used in this study. Nevertheless, we still could not reproduce the highly sensitive adenosine sensing data reported by Lee group.

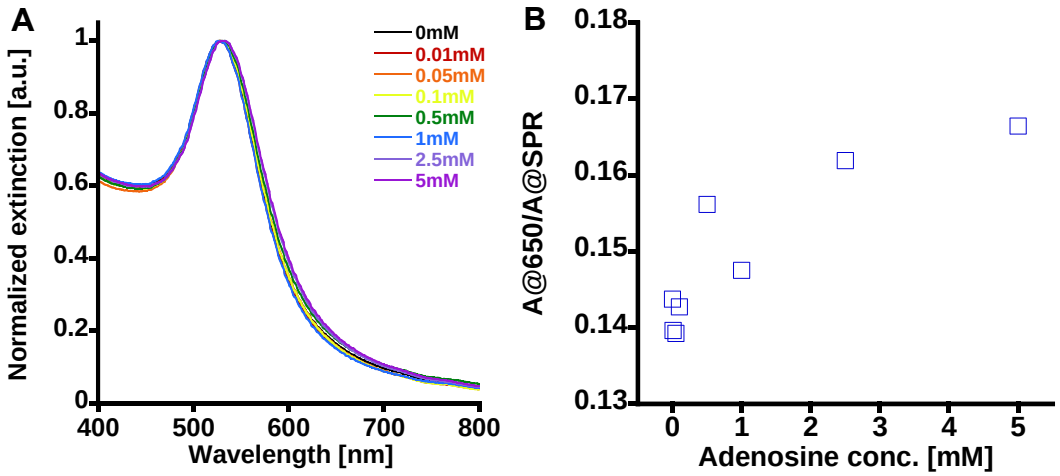

Figure 6-6. UV-Vis spectra (A) and a calibration curve (B) of adenosine sensing assays prepared with 5T linkers using Lee method.

6.3.4. **Adenosine binding test with the samples prepared with modified Lee method**

Compared to original citric acid-AuNPs, SPR peaks for both DNA1-AuNPs and DNA2-AuNPs were redshifted by 3 nm (See Figure 6-7), indicating the success of aptamer conjugation on the AuNP surface using modified Lee method. DNA1-AuNPs and DNA2-AuNPs were kept colloidal stability, even after dispersed in buffer containing high concentration of salt (300 mM NaCl).

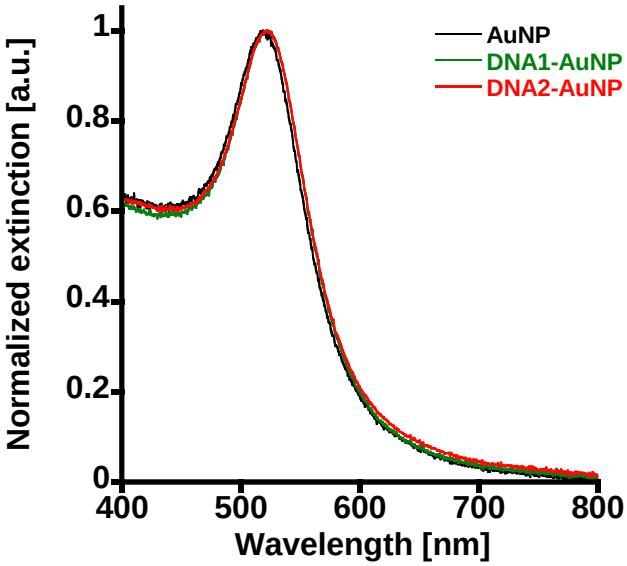

Figure 6-7. UV-vis spectra of DNA1-AuNPs and DNA2-AuNPs dispersed in 25 mM Tris buffer containing 300 mM NaCl at pH 8.2.

Following the colloidal stability test, we also characterized adenosine sensing assays prepared using modified Lee method to test the efficacy of adenosine sensing. Figure 6-8A exhibits clear extinction changes as a function of adenosine concentration. A 6 nm red shift was detected for the SPR peak at 5 mM adenosine compared to that at 0 mM adenosine. Apart from the SPR red shift, adenosine induced nanoparticle aggregation was also confirmed with the increase in A@650/A@SPR (Figure 6-8B). The range of A@650/A@SPR for the samples prepared using the modified Lee method (0.056) was about 2.4 times higher than that for the samples prepared using Lee method. The adenosine sensitivity of modified Lee method was superior to any other experimental protocols we have tried in this study.

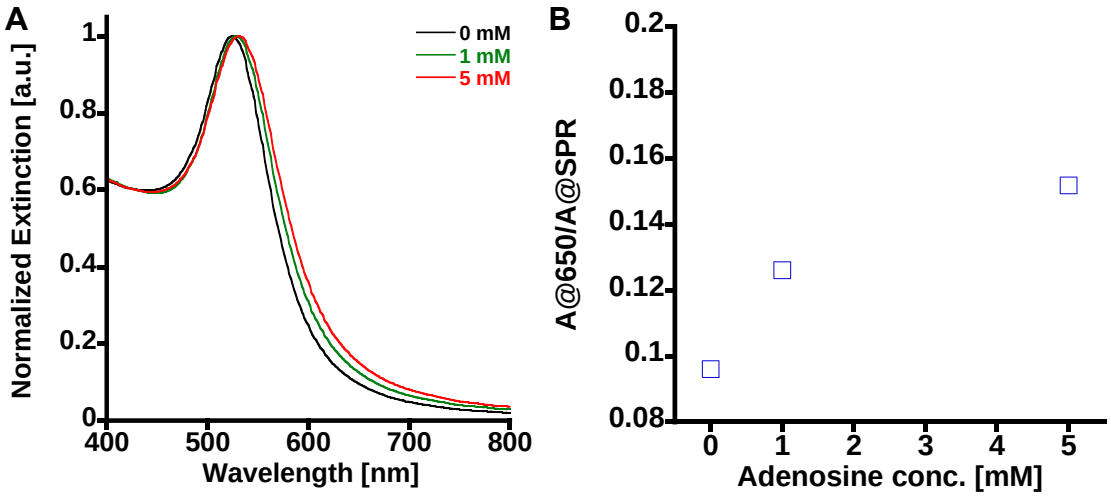

Figure 6-8. UV-Vis spectra (A) and a calibration curve (B) of adenosine sensing assays prepared using modified Lee method. The assays were incubated with three different adenosine concentrations at 18 ˚C.

Previously, Lee group showed the temperature dependency on adenosine sensitivity. The adenosine sensing assays totally lost their target sensitivity when the incubation temperature was lowered from RT to 4 ˚C. They asserted that temperature is an important parameter which governs the kinetics of adenosine binding. We speculated that the inconsistency in the results difference between our group and Lee group can be related to the incubation temperature difference. To test if incubation temperature played a role in adenosine sensing, we measured the temperatures at both group's labs. The temperatures of our lab and Lee group's lab were 18 and 29 ˚C, respectively. Therefore, we repeated adenosine binding test by incubating samples at 29 ˚C using convection oven. When the adenosine sensing assay was incubated with 5 mM adenosine, we

observed a significant AuNP color change from red to purple. The increase in incubation temperature resulted in the improvement of adenosine sensitivity as depicted in Figure 6-9. However, we could still not achieve the same adenosine sensitivity which Lee group reported. This finding suggests that there were experimentally uncontrollable variables that lead to the discrepancies.

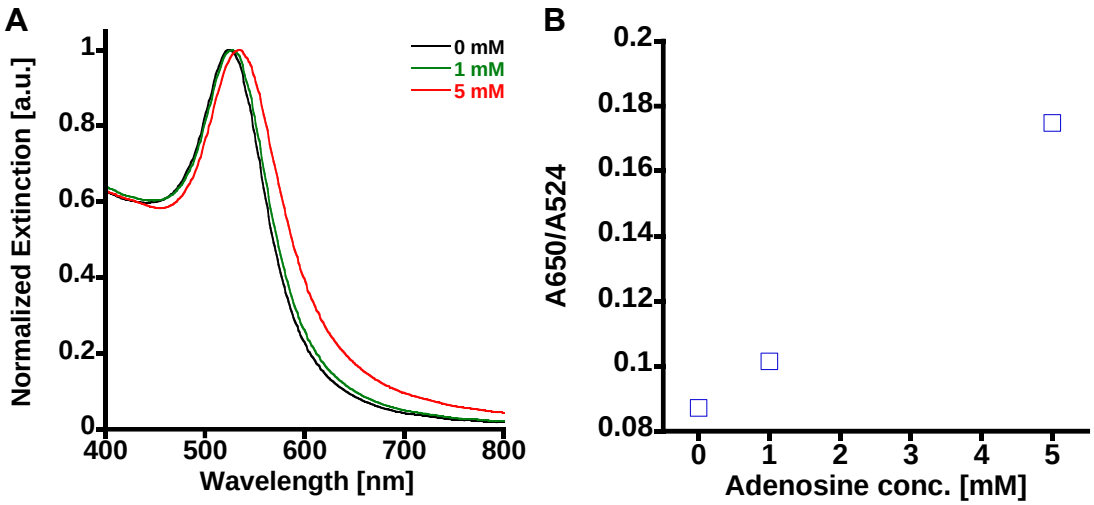

Figure 6-9. UV-Vis spectra (A) and a calibration curve (B) of adenosine sensing assays prepared using modified Lee method. The assays were incubated with three different adenosine concentrations at 29 ˚C.

The feasibility of reversible adenosine sensing was also studied with the adenosine sensing assays prepared with modified Lee method. The adenosine sensing assay was incubated with 5 mM adenosine at 29 ˚C for 2 hr to form AuNP aggregates.

Subsequently, the assay was heated at 75 ˚C for 3 min to break down the AuNP aggregates. The heated assay was washed with 25 mM Tris buffer and then redispersed in the same buffer. Initially, we monitored the change of SPR peak for each step. After the assay was exposed to 5 mM adenosine, SPR peak was redshifted from 524 to 533 nm (See Figure 6-10A), which indicates the formation of AuNP aggregation. When the AuNP aggregates were heated, we observed a 3 nm blue shift. Contrary to our expectation, SPR peak did not fully come back to 524 nm (SPR peak for control) after heat treatment. This indicates that heat associated conformational changes of aptamer did not significantly affect the aggregation state of AuNPs. We suggest that the heat treatment resulted only in breaking down hydrogen bonds between DNA1 and DNA2 whereas adenosines bound between DNA1 and DNA2. Therefore, DNA1-AuNPs and DNA2-AuNPs still form AuNP aggregates due to residual adenosines. Interestingly, as the heated AuNP aggregates were washed with Tris buffer, SPR peak was further blue shifted to 524 nm (Blue curve in Figure 6-10A), indicating that AuNP aggregates were fully de-aggregated while washing. The robust detachment of analyte from aptamer binding sites can be explained by the huge chemical potential change due to the washing step. A similar reversible trend was observed with A@650/A@SPR as shown in Figure 6-10B.

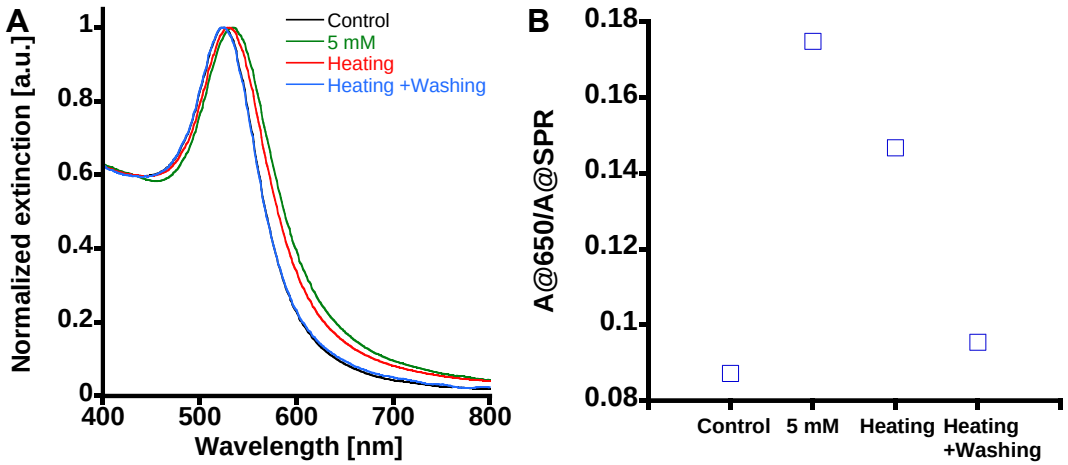

Figure 6-10. Reversible aggregation of adenosine sensing assay monitored by UV-Vis (A) and relative extinction ratio (B).

We also tried to demonstrate SERS based adenosine sensing by slightly modifying the adenosine sensing assay prepared using the modified Lee method. To induce analyte concentration dependent SERS signals, we conjugated MGITC to DNA2-AuNPs. The molar ratio of AuNP to MGITC was varied from 1:250 to 1:500. As depicted in Figure 6-11, no SPR peak shift was detected upon MGITC conjugation. However, a shoulder peak appeared approximately at 630 nm for both molar ratios. We attribute the presence of shoulder peak to MGITC on AuNP surface since the shoulder peak location was matched with the peak location of MGITC extinction spectrum.[214] MGITC conjugation on AuNPs with 1:250 did not affect the extinction of DNA2-AuNPs. Nevertheless, with 1:500 molar ratio of DNA2-AuNP to MGITC, we observed a significant extinction increase in the wavelength range from 600 to 700 nm, which was a

strong evidence of nonspecific AuNP aggregation formation. Consequently, we chose the molar ratio of 1:250 for further adenosine sensing studies.

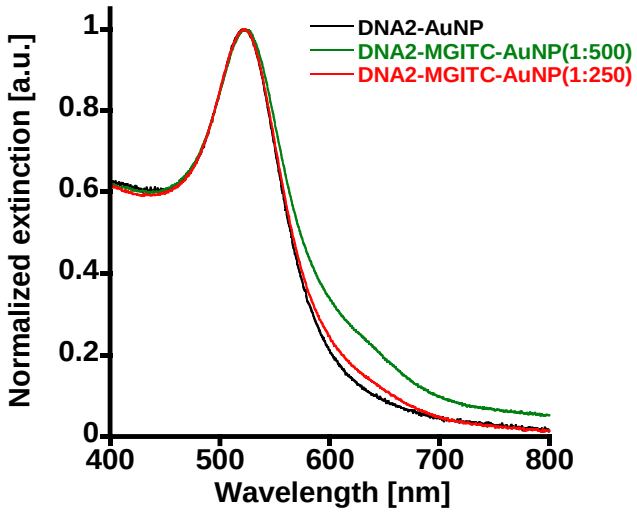

Figure 6-11. UV-vis spectra of DNA2-AuNPs MGITC conjugated DNA2-AuNPs with two different molar ratios of DNA2-AuNP to MGITC.

To investigate the correlation between MGITC conjugation to DNA2-AuNPs and adenosine sensitivity, adenosine sensing assays composed of DNA1-AuNPs and DNA2-MGITC-AuNPs were further tested with three different adenosine concentrations (0, 1, and 5 mM) with UV-Vis. Figure 6-12A exhibits adenosine concentration dependent extinction changes, indicating that aggregation formation due to adenosine-aptamer interaction was not affected by MGITC conjugation on DNA2-AuNPs. Moreover, the

range of A@650/A@SPR for adenosine sensing assay was slightly elevated after DNA2-AuNPs were conjugated with MGITC.

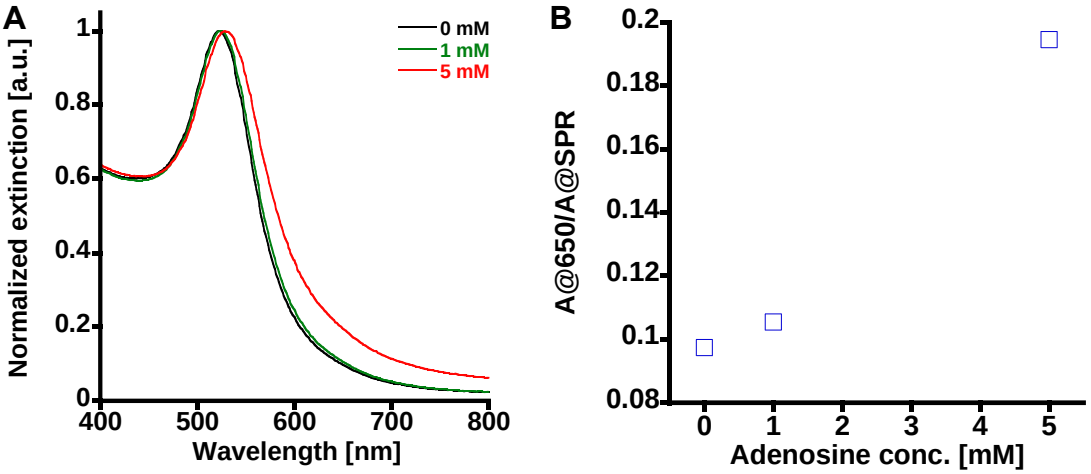

Figure 6-12. UV-Vis spectra (A) and a calibration curve (B) of adenosine sensing assays composed of DNA1-AuNPs and DNA2-MGITC-AuNPs.

We evaluated target level dependent AuNP aggregation using a hand held Raman system. Regardless of target concentration, SERS signal of adenosine sensing assay exhibited all characteristic SERS bands of MGITC as shown in Figure 6-13A. This means that even dispersed DNA2-MGITC-AuNPs were able to enhance Raman scattering of MGITC with their LSPR. To quantify the SERS signal changes as a function of target concentration, we constructed a calibration curve by plotting SERS intensity at 1616 cm^{-1} versus target concentration (See Figure 6-13B). The SERS

intensities at 1 and 5 mM were compared with a negative control (SERS intensity at 0 mM). According to two tailed t-test (α=0.05), SERS intensities at both target concentration was not significantly different.

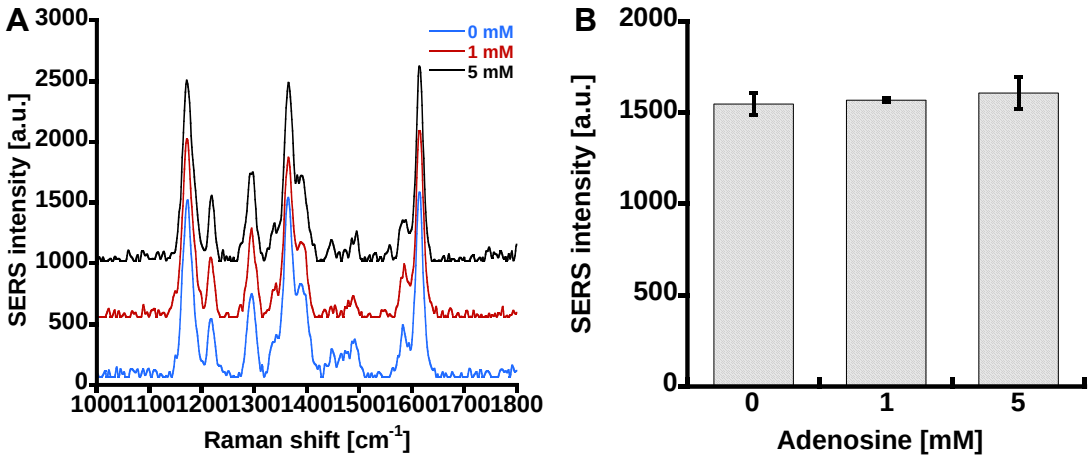

Figure 6-13. (A) SERS spectra of adenosine sensing assays at different adenosine concentrations. (B) A calibration curve of target level dependent SERS intensity at 1616 cm^{-1} (Error bars represent one standard deviations calculated from three different aliquots (n=3)).

Krpetic *et al*. reported that the change in SERS intensity of sandwich assay is influenced by nanoparticle size.[215] Similar to our SERS results, the authors did not observe any significant increase in SERS intensity from their SERS based sandwich with 14 nm AuNPs. However, they were able to achieve a much higher SERS sensitivity by increasing nanoparticle size from 14 to 45 nm. They explained this observation by the

nanoparticle size dependence on gap plasmon resonance (GPR). With the fixed interparticle gap, GPR is more redshifted as nanoparticle size increases. The larger GPR peak location, the higher SERS enhancement.

To improve SERS sensitivity of adenosine sensing assay we also adopted 45 nm AuNPs. Initially, we prepared MGITC free adenosine sensing assays with 45 nm AuNPs to investigate the effect of nanoparticle size on extinction spectrum. As shown in Figure 6-14A, adenosine sensing assays using 45 nm AuNPs provided better performance in terms of extinction spectral changes than the same assays using 14 nm AuNPs. The range of A@650/A@SPR for adenosine sensing assay was doubled by increasing nanoparticle size from 14 to 45 nm (Figure 6-14B). However, as MGITC was combined with adenosine sensing assay using 45 nm AuNPs, the sensitivity of adenosine sensing assay was dramatically diminished (See Figure 6-15).

In case of SERS based adenosine sensing, the sensitivity was significantly improved by substituting 45 nm AuNPs for 14 nm ones (See Figure 6-16). A linear trend was observed in SERS intensity increase as a function of adenosine concentration. All tested adenosine concentrations showed statistically meaningful SERS intensity increases compared to the control (0 mM adenosine) based on two tailed t-test (α=0.05).

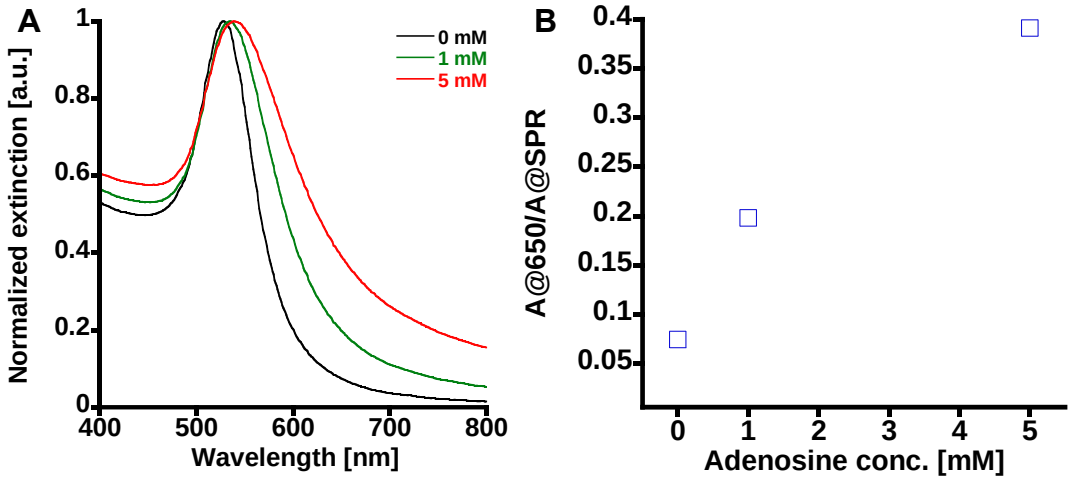

Figure 6-14. UV-Vis spectra (A) and a calibration curve (B) of MGITC free adenosine sensing assay prepared with 45 nm AuNPs.

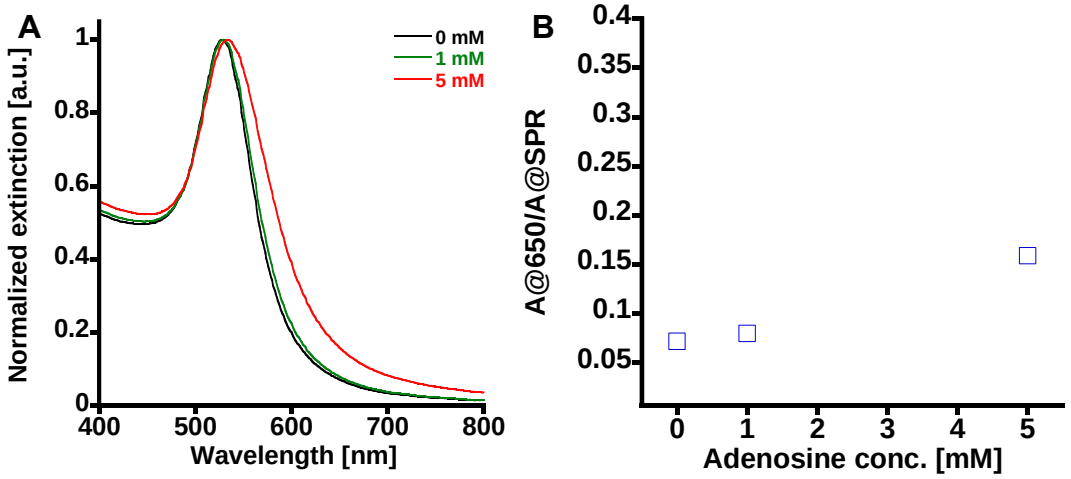

Figure 6-15. UV-Vis spectra (A) and a calibration curve (B) of adenosine sensing assay prepared with 45 AuNPs containing MGITC.

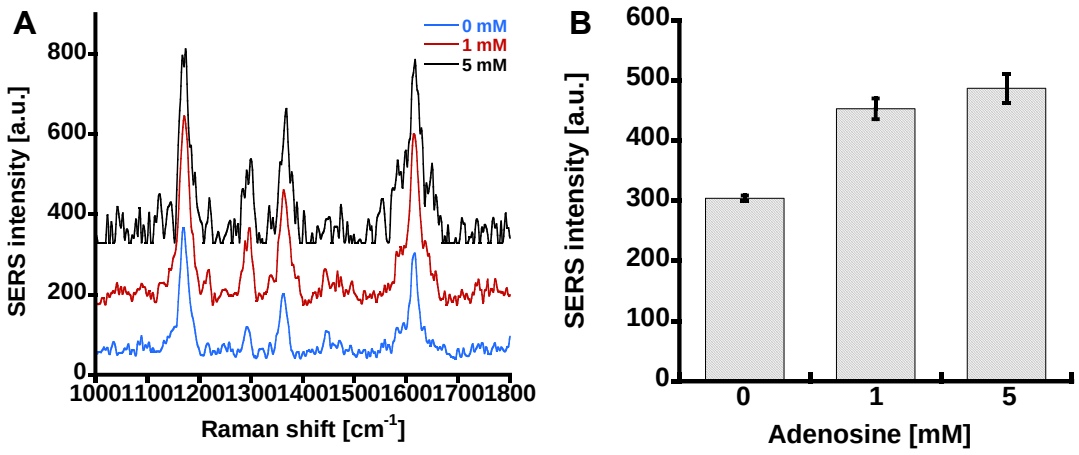

Figure 6-16. (A) SERS spectra of adenosine sensing assays using 45 nm AuNPs at different adenosine concentrations. (B) A calibration curve of target level dependent SERS intensity at 1616 cm^{-1} (Error bars represent one standard deviations calculated from three different aliquots (n=3)).

6.4. **Conclusion**

Adenosine sensing based on nanoparticle aggregations with split aptamers was tried by following several protocols that were reported in the experimental sections of multiple published journal papers. However, significant adenosine induced nanoparticle aggregation was achieved only with the detailed experimental method directly provided from the author (Lee group) who recently reported nanoparticle based adenosine sensing. This indicates that the experimental details reported in most of the published works for aptamer based nanoparticle assays cannot be easily reproduced by other research groups. We also transformed the colorimetric adenosine sensing assay (synthesized with the protocol provided by the Lee group) to utilize in SERS sensing, by

attaching a Raman active dye on the surface of aptamer conjugated nanoparticles. Future work will be focused on encapsulating this SERS active adenosine sensing assay in microdomains that are embedded in hydrogels to study reversible aggregation of nanoparticles.

7. CONCLUSIONS AND FUTURE WORKS

In this work, a novel SERS based hydrogel sensor was developed using modular microdomains. As a proof of concept, pH-sensitive SERS reporters (MBA-AuNPs) were encapsulated in polyelectrolyte multilayer microcapsules dispersed in alginate hydrogel matrix. Successful encapsulation of MBA-AuNPs in the microcapsules were confirmed with several material characterization tools such as SEM, EDS, and darkfield microscopy. Moreover, the number of gold nanoparticles per microcapsule was estimated to be 1373 per capsule. This was determined by a new proposed quantification analysis method developed by the combination of SEM, XRD, and INAA data. The pH sensitive Raman signal of the MBA-AuNPs were successfully detected overcoming random scatterings from hydrogel matrix and polymeric microcapsules materials. The SERS based pH sensing with these hydrogels was fully reversible showing a sigmoidal response curve for ratiometric intensity changes at 1430 and 1078cm^{-1}, respectively. The analytical range was pH 4.43-8.07 (pKa~5.80) with an average sensitivity of 0.07 pH^{-1}. To assess the potential for sensing enzymatic substrates, hydrogels were prepared with the MBA-AuNPs co-encapsulated with glucose oxidase. Raman spectra recorded from hydrogels exposed to physiological glucose levels (0-400 mg/dL) exhibited apparent trends of decreasing pH from pH ~6.50 to pH ~4.50 due to glucose oxidization within the microdomains. The glucose diffusion into the capsules was controlled by crosslinking the polyelectrolyte multilayers with glutaraldehyde, showing an approach to

adjust the balance of oxygen and glucose flux into the microcavities, yielding a tunable sensitivity of the glucose-proportional change at steady-state pH.

We incorporated pH sensitive and oxygen sensitive microdomains into a single alginate hydrogel that could be interrogated via SERS and phosphorescent lifetime optical modalities respectively to develop multimodal-mulitanalyte sensing hydrogel sensors. Microdomains consisted of discrete polyelectrolyte multilayer microcapsules that encapsulated MBA-AuNPs and oxygen sensitive benzoporphyrin dyes separately. The polyelectrolyte multilayer nanofilms fabricated through LbL were effective at minimizing optical interferences by spatially separating optical probes. Although the microdomain embedded hydrogels containing both SERS and phosphorescence lifetime probes (dual modal sensing hydrogel) presented a huge luminescence background, a pH sensitive SERS signal was distinguishable for all tested pH conditions. Comparison of the dual mode sensor's ability to track pH and oxygen showed no statistically significant difference when compared to separate standalone single mode pH or oxygen sensors. In addition, redundant glucose sensing through dual modalities was demonstrated by chemically crosslinking glucose oxidase in the alginate matrix of dual modal sensing hydrogel. Each optical mode showed a signal change proportional to glucose concentration with an opposite signal directionality. We also confirmed the full reversibility of glucose sensing by exposing glucose sensing hydrogels sequentially to two extreme glucose levels (0 and 400 mg/dL). These results support the feasibility of a dual modal sensing approach for continuous glucose monitoring with improved measurement accuracy due to measurement redundancy.

To demonstrate a practical continuous glucose monitoring with the dual modal hydrogels, SERS based pH sensing also needs to be performed dynamically similar to phosphorescence lifetime based oxygen sensing. The SERS based pH sensing data exhibited in this work was collected under static conditions. Future work should focus on developing a flow cell system with a portable Raman system to evaluate the materials continuously. Based on dynamic SERS based pH sensing data, enzymatic reaction in the materials can be tuned to achieve desired sensitivity and dynamic range. Eventually, the portable Raman system needs to be combined with a pre-existing portable phosphorescence lifetime system to obtain redundant measurements for continuous glucose monitoring with an error checking function.

For the future *in vivo* applications of this study, alginate hydrogel matrix can be substituted with other biocompatible hydrogel materials to minimize a potential host response. To select optimal materials, following three requirements should be satisfied: (1) low Raman scattering cross-section, (2) anti-fouling property, and (3) good diffusivity of analytes such as glucose and oxygen. For the purpose of *in vivo* SERS sensing, an implant sensor is located at a few mm from the skin surface. To increase the SNR of SERS sensing through the skin tissue, spherical nanoparticles can be replaced by other nanoparticles with different shapes which provide a much higher SERS enhancement factor. In regards to instrumentation, spatially offset Raman spectroscopy (SORS) could also be adopted to achieve a better SNR.[216]

The encapsulation of aggregation based SERS assay in microcapsules was demonstrated in this section. The aggregation based SERS assay has a great potential to

increase number of detectable analytes since several functional group (i.e. hybridization based DNAs/RNAs, aptamers, and antibodies) can be applied to this assay. The encapsulation of hybridization based microRNA-17 sensing assay was evaluated directly using microcapsules rather than using hydrogel containing encapsulated microcapsules. This was done owing to the fact that the presence of calcium ions in the alginate hydrogel can induce non-specific aggregation of the assay. The encapsulated microRNA-17 sensing assay using microcapsules exhibited target level dependent SERS signal changes. This indicated that controlled aggregation of nanoparticles proportional to target concentration can be achieved in the microdomains. In addition, the microcapsules containing the microRNA-17 sensing assay showed a target sensitivity even in the presence of large protein molecules which has the potential to induce non-specific nanoparticle aggregation. This indicated that polymeric microcapsules selectively excluded the large protein molecules allowing small analytes diffuse into the microdomains. As a future work, the microRNA-17 sensing MCs should be embedded into biocompatible hydrogels whose composition and synthesis method do not induce non-specific aggregation. After proper selection of hydrogel, this assay can be tested in a flow through system to show the concept of continuous analyte sensing through reversible nanoparticle aggregation in the microdomains.

REFERENCES

1. Bernell, S.; Howard, S. W., Use your words carefully: what is a chronic disease? *Frontiers in Public Health* **2016,** *4*, 159.

2. Alwan, A., *Global status report on noncommunicable diseases 2010*. World Health Organization: 2011.

3. Bauer, U. E.; Briss, P. A.; Goodman, R. A.; Bowman, B. A., Prevention of chronic disease in the 21st century: elimination of the leading preventable causes of premature death and disability in the USA. *The Lancet* **2014,** *384* (9937), 45-52.

4. Gerteis, J.; Izrael, D.; Deitz, D.; LeRoy, L.; Ricciardi, R.; Miller, T.; Basu, J., Multiple chronic conditions chartbook. *Rockville, MD: Agency for Healthcare Research and Quality* **2014**.

5. Medicare, C. f.; Services, M., *Chronic conditions among medicare beneficiaries*, chartbook 2012, 11, 15-21.

6. Clark Jr, L. C.; Lyons, C., Electrode systems for continuous monitoring in cardiovascular surgery. *Annals of the New York Academy of Sciences* **1962,** *102* (1), 29-45.

7. Bolinder, J.; Hagström, E.; Ungerstedt, U.; Arner, P., Microdialysis of subcutaneous adipose tissue in vivo for continuous glucose monitoring in man. *Scandinavian Journal of Clinical and Laboratory Investigation* **1989,** *49* (5), 465-474.

8. Meyerhoff, C.; Mennel, F.; Sternberg, F.; Pfeiffer, E., Current status of the glucose sensor. *The Endocrinologist* **1996,** *6* (1), 51-58.

9. Moberg, E.; Hagström-Toft, E.; Bolinder, J., Detection of hypoglycaemia by microdialysis-measurements of glucose in subcutaneous adipose tissue. *Hormone and Metabolic Research* **1997,** *29* (09), 440-443.

10. Wang, J., Glucose biosensors: 40 years of advances and challenges. *Electroanalysis* **2001,** *13* (12), 983-988.

11. Klonoff, D. C., Continuous glucose monitoring: roadmap for 21st century diabetes therapy. *Diabetes Care* **2005,** *28* (5), 1231-1239.

12. Mortellaro, M.; DeHennis, A., Performance characterization of an abiotic and fluorescent-based continuous glucose monitoring system in patients with type 1 diabetes. *Biosensors and Bioelectronics* **2014,** *61*, 227-231.

13. Kassal, P.; Steinberg, M. D.; Steinberg, I. M., Wireless chemical sensors and biosensors: a review. *Sensors and Actuators B: Chemical* **2018,** *266*, 228-245.

14. Wisniewski, N. A.; Nichols, S. P.; Gamsey, S. J.; Pullins, S.; Au-Yeung, K. Y.; Klitzman, B.; Helton, K. L., Tissue-integrating oxygen sensors: continuous tracking of tissue hypoxia. In *Oxygen transport to tissue XXXIX*, Springer: 2017; pp 377-383.

15. Abraham, A. A.; Fei, R.; Coté, G. L.; Grunlan, M. A., Self-cleaning membrane to extend the lifetime of an implanted glucose biosensor. *ACS Applied Materials & Interfaces* **2013,** *5* (24), 12832-12838.

16. Roberts, J. R.; Park, J.; Helton, K.; Wisniewski, N.; McShane, M. J., Biofouling of polymer hydrogel materials and its effect on diffusion and enzyme-based luminescent glucose sensor functional characteristics. *Journal of Diabetes Science and Technology* **2012,** *6* (6), 1267-1275.

17. Lipani, L.; Dupont, B. G.; Doungmene, F.; Marken, F.; Tyrrell, R. M.; Guy, R. H.; Ilie, A., Non-invasive, transdermal, path-selective and specific glucose monitoring via a graphene-based platform. *Nature Nanotechnology* **2018**, *13*, 504-511.

18. Park, H. D.; Lee, K. J.; Yoon, H. R.; Nam, H. H., Design of a portable urine glucose monitoring system for health care. *Computers in Biology and Medicine* **2005,** *35* (4), 275-286.

19. Lee, H.; Song, C.; Hong, Y. S.; Kim, M. S.; Cho, H. R.; Kang, T.; Shin, K.; Choi, S. H.; Hyeon, T.; Kim, D.-H., Wearable/disposable sweat-based glucose monitoring device with multistage transdermal drug delivery module. *Science Advances* **2017,** *3* (3), e1601314.

20. Zhang, W.; Du, Y.; Wang, M. L., On-chip highly sensitive saliva glucose sensing using multilayer films composed of single-walled carbon nanotubes, gold nanoparticles, and glucose oxidase. *Sensing and Bio-sensing Research* **2015,** *4*, 96-102.

21. Blank, T. B.; Ruchti, T. L.; Lorenz, A. D.; Monfre, S. L.; Makarewicz, M.; Mattu, M.; Hazen, K. In *Clinical results from a noninvasive blood glucose monitor*, Optical Diagnostics and Sensing of Biological Fluids and Glucose and Cholesterol Monitoring II, International Society for Optics and Photonics: 2002; pp 1-11.

22. Control, D.; Group, C. T. R., The effect of intensive treatment of diabetes on the development and progression of long-term complications in insulin-dependent diabetes mellitus. *New England Journal of Medicine* **1993,** *329* (14), 977-986.

23. Cameron, B. D.; Gorde, H. W.; Satheesan, B.; Cote, G. L., The use of polarized laser light through the eye for noninvasive glucose monitoring. *Diabetes Technology & Therapeutics* **1999,** *1* (2), 135-143.

24. Kajiwara, K.; Uemura, T.; Kishikawa, H.; Nishida, K.; Hashiguchi, Y.; Uehara, M.; Sakakida, M.; Ichinose, K.; Shichiri, M., Noninvasive measurement of blood glucose concentrations by analysing Fourier transform infra-red absorbance spectra through oral mucosa. *Medical & Biological Engineering & Computing* **1993,** *31* (1), S17-S22.

25. Hillier, T. A.; Abbott, R. D.; Barrett, E. J., Hyponatremia: evaluating the correction factor for hyperglycemia. *The American Journal of Medicine* **1999,** *106* (4), 399-403.

26. Wentholt, I.; Hoekstra, J.; Zwart, A.; DeVries, J., Pendra goes Dutch: lessons for the CE mark in Europe. *Diabetologia* **2005,** *48* (6), 1055-1058.

27. Gourzi, M.; Rouane, A.; McHugh, M.; Guelaz, R.; Nadi, M. In *New biosensor for non-invasive glucose concentration measurement*, Sensors, 2003. Proceedings of IEEE, IEEE: 2003; pp 1343-1347.

28. Sieg, A.; Guy, R. H.; Delgado-Charro, M. B., Noninvasive glucose monitoring by reverse iontophoresis in vivo: application of the internal standard concept. *Clinical Chemistry* **2004,** *50* (8), 1383-1390.

29. Tierney, M. J.; Tamada, J. A.; Potts, R. O.; Jovanovic, L.; Garg, S.; Team, C. R., Clinical evaluation of the GlucoWatch® biographer: a continual, non-invasive glucose

monitor for patients with diabetes. *Biosensors and Bioelectronics* **2001,** *16* (9-12), 621-629.

30. Mendelson, Y.; Clermont, A. C.; Peura, R. A.; Lin, B.-C., Blood glucose measurement by multiple attenuated total reflection and infrared absorption spectroscopy. *IEEE Transactions on Biomedical Engineering* **1990,** *37* (5), 458-465.

31. Arnold, M. A.; Olesberg, J. T.; Small, G. W., *In vivo glucose sensing.* John Wiley & Sons 2009, 357-390.

32. Vashist, S. K., Non-invasive glucose monitoring technology in diabetes management: a review. *Analytica Chimica Acta* **2012,** *750*, 16-27.

33. Thennadil, S. N.; Rennert, J. L.; Wenzel, B. J.; Hazen, K. H.; Ruchti, T. L.; Block, M. B., Comparison of glucose concentration in interstitial fluid, and capillary and venous blood during rapid changes in blood glucose levels. *Diabetes Technology & Therapeutics* **2001,** *3* (3), 357-365.

34. Brancaleon, L.; Bamberg, M. P.; Sakamaki, T.; Kollias, N., Attenuated total reflection–Fourier transform infrared spectroscopy as a possible method to investigate biophysical parameters of stratum corneum in vivo. *Journal of Investigative Dermatology* **2001,** *116* (3), 380-386.

35. Malchoff, C. D.; Shoukri, K.; Landau, J. I.; Buchert, J. M., A novel noninvasive blood glucose monitor. *Diabetes Care* **2002,** *25* (12), 2268-2275.

36. Yeh, S.-j.; Hanna, C. F.; Khalil, O. S., Monitoring blood glucose changes in cutaneous tissue by temperature-modulated localized reflectance measurements. *Clinical Chemistry* **2003,** *49* (6), 924-934.

37. Cameron, B. D.; Baba, J. S.; Cote, G. L. In *Optical polarimetry applied to the development of a noninvasive in-vivo glucose monitor*, Optical Diagnostics of Biological Fluids V, International Society for Optics and Photonics: 2000; pp 66-78.

38. Baba, J. S.; Cameron, B. D.; Cote, G. L., Effect of temperature, pH, and corneal birefringence on polarimetric glucose monitoring in the eye. *Journal of Biomedical Optics* **2002,** *7* (3), 321-329.

39. Berger, A. J.; Itzkan, I.; Feld, M. S., Feasibility of measuring blood glucose concentration by near-infrared Raman spectroscopy. *Spectrochimica Acta Part A: Molecular and Biomolecular Spectroscopy* **1997,** *53* (2), 287-292.

40. Lambert, J. L.; Pelletier, C. C.; Borchert, M. S., Glucose determination in human aqueous humor with Raman spectroscopy. *Journal of Biomedical Optics* **2005,** *10* (3), 031110.

41. Raman, C. V.; Krishnan, K. S., A new type of secondary radiation. *Nature* **1928,** *121* (3048), 501-502.

42. Bohren, C. F.; Huffman, D. R., *Absorption and scattering of light by small particles*. John Wiley & Sons 2008.

43. Kneipp, K.; Kneipp, H.; Itzkan, I.; Dasari, R. R.; Feld, M. S., Ultrasensitive chemical analysis by Raman spectroscopy. *Chemical Reviews* **1999,** *99* (10), 2957-2976.

44. Pozzi, E. A.; Zrimsek, A. B.; Lethiec, C. M.; Schatz, G. C.; Hersam, M. C.; Van Duyne, R. P., Evaluating single-molecule Stokes and anti-Stokes SERS for nanoscale thermometry. *The Journal of Physical Chemistry C* **2015,** *119* (36), 21116-21124.

45. Gersten, J.; Nitzan, A., Electromagnetic theory of enhanced Raman scattering by molecules adsorbed on rough surfaces. *The Journal of Chemical Physics* **1980,** *73* (7), 3023-3037.

46. Procházka, M., *Surface-enhanced Raman spectroscopy: bioanalytical, biomolecular and medical applications*. Springer 2015.

47. Bernath, P. F., *Spectra of atoms and molecules*. Oxford university press: 2015.

48. Smith, E.; Dent, G., *Modern Raman spectroscopy: a practical approach*. John Wiley & Sons 2013.

49. Jeanmaire, D. L.; Van Duyne, R. P., Surface Raman spectroelectrochemistry: part I. heterocyclic, aromatic, and aliphatic amines adsorbed on the anodized silver electrode. *Journal of Electroanalytical Chemistry and Interfacial Electrochemistry* **1977,** *84* (1), 1-20.

50. Albrecht, M. G.; Creighton, J. A., Anomalously intense Raman spectra of pyridine at a silver electrode. *Journal of the American Chemical Society* **1977,** *99* (15), 5215-5217.

51. Billmann, J.; Kovacs, G.; Otto, A., Enhanced Raman effect from cyanide adsorbed on a silver electrode. *Surface Science* **1980,** *92* (1), 153-173.

52. Kneipp, K.; Kneipp, H.; Itzkan, I.; Dasari, R. R.; Feld, M. S., Surface-enhanced non-linear Raman scattering at the single-molecule level. *Chemical Physics* **1999,** *247* (1), 155-162.

53. Rivas, L.; Sanchez-Cortes, S.; Garcia-Ramos, J.; Morcillo, G., Mixed silver/gold colloids: a study of their formation, morphology, and surface-enhanced Raman activity. *Langmuir* **2000,** *16* (25), 9722-9728.

54. Oldenburg, S. J.; Westcott, S. L.; Averitt, R. D.; Halas, N. J., Surface enhanced Raman scattering in the near infrared using metal nanoshell substrates. *The Journal of Chemical Physics* **1999,** *111* (10), 4729-4735.

55. Jackson, J.; Westcott, S.; Hirsch, L.; West, J.; Halas, N., Controlling the surface enhanced Raman effect via the nanoshell geometry. *Applied Physics Letters* **2003,** *82* (2), 257-259.

56. Dick, L. A.; McFarland, A. D.; Haynes, C. L.; Van Duyne, R. P., Metal film over nanosphere (MFON) electrodes for surface-enhanced Raman spectroscopy (SERS): improvements in surface nanostructure stability and suppression of irreversible loss. *The Journal of Physical Chemistry B* **2002,** *106* (4), 853-860.

57. Bello, J.; Stokes, D.; Vo-Dinh, T., Silver-coated alumina as a new medium for surfaced-enhanced Raman scattering analysis. *Applied Spectroscopy* **1989,** *43* (8), 1325-1330.

58. Haynes, C. L.; Van Duyne, R. P., Plasmon-sampled surface-enhanced Raman excitation spectroscopy. *The Journal of Physical Chemistry B* **2003,** *107* (30), 7426-7433.

59. McFarland, A. D.; Young, M. A.; Dieringer, J. A.; Van Duyne, R. P., Wavelength-scanned surface-enhanced Raman excitation spectroscopy. *The Journal of Physical Chemistry B* **2005,** *109* (22), 11279-11285.

60. De Jesus, M.; Giesfeldt, K.; Oran, J.; Abu-Hatab, N.; Lavrik, N.; Sepaniak, M., Nanofabrication of densely packed metal–polymer arrays for surface-enhanced Raman spectrometry. *Applied Spectroscopy* **2005,** *59* (12), 1501-1508.

61. Zhang, X.; Yu, Z.; Ji, W.; Sui, H.; Cong, Q.; Wang, X.; Zhao, B., Charge-transfer effect on surface-enhanced Raman scattering (SERS) in an ordered Ag NPs/4-mercaptobenzoic acid/TiO2 system. *The Journal of Physical Chemistry C* **2015,** *119* (39), 22439-22444.

62. Valley, N.; Greeneltch, N.; Van Duyne, R. P.; Schatz, G. C., A look at the origin and magnitude of the chemical contribution to the enhancement mechanism of surface-enhanced Raman spectroscopy (SERS): theory and experiment. *The Journal of Physical Chemistry Letters* **2013,** *4* (16), 2599-2604.

63. Zeman, E. J.; Schatz, G. C., An accurate electromagnetic theory study of surface enhancement factors for silver, gold, copper, lithium, sodium, aluminum, gallium, indium, zinc, and cadmium. *Journal of Physical Chemistry* **1987,** *91* (3), 634-643.

64. Cullum, B. M.; Li, H.; Hankus, M.; Schiza, M., Characterization of multilayer-enhanced surface-enhanced Raman scattering (SERS) substrates and their potential for SERS nanoimaging. *Nanobiotechnology* **2007,** *3* (1), 1-11.

65. Gewehr, P. M.; Delpy, D. T., Optical oxygen sensor based on phosphorescence lifetime quenching and employing a polymer immobilised metalloporphyrin probe. *Medical and Biological Engineering and Computing* **1993,** *31* (1), 2-10.

66. Quaranta, M.; Borisov, S. M.; Klimant, I., Indicators for optical oxygen sensors. *Bioanalytical Reviews* **2012,** *4* (2-4), 115-157.

67. Vanderkooi, J. M.; Maniara, G.; Green, T. J.; Wilson, D. F., An optical method for measurement of dioxygen concentration based upon quenching of phosphorescence. *Journal of Biological Chemistry* **1987,** *262* (12), 5476-5482.

68. Lakowicz, J. R., *Principles of fluorescence spectroscopy*. Kluwer Academic/Plenum Publishers 2004.

69. Senapati, D.; Dasary, S. S.; Singh, A. K.; Senapati, T.; Yu, H.; Ray, P. C., A label-free gold-nanoparticle-based SERS assay for direct cyanide detection at the parts-per-trillion level. *Chemistry–A European Journal* **2011,** *17* (30), 8445-8451.

70. Ulman, A., Formation and structure of self-assembled monolayers. *Chemical Reviews* **1996,** *96* (4), 1533-1554.

71. Yuan, J.; Lai, Y.; Duan, J.; Zhao, Q.; Zhan, J., Synthesis of a β-cyclodextrin-modified Ag film by the galvanic displacement on copper foil for SERS detection of PCBs. *Journal of Colloid and Interface Science* **2012,** *365* (1), 122-126.

72. Du, J.; Jing, C., Preparation of thiol modified Fe3O4@ Ag magnetic SERS probe for PAHs detection and identification. *The Journal of Physical Chemistry C* **2011,** *115* (36), 17829-17835.

73. Kim, D. J.; Jeon, T. Y.; Baek, Y.-K.; Park, S.-G.; Kim, D.-H.; Kim, S.-H., Metal nanoparticle-loaded microgels with selective permeability for direct detection of small molecules in biological fluids. *Chemistry of Materials* **2016,** *28* (5), 1559-1565.

74. Mitomo, H.; Horie, K.; Matsuo, Y.; Niikura, K.; Tani, T.; Naya, M.; Ijiro, K., Active gap SERS for the sensitive detection of biomacromolecules with plasmonic nanostructures on hydrogels. *Advanced Optical Materials* **2016,** *4* (2), 259-263.

75. Eling, C. J.; Price, T. W.; Marshall, A. R.; Viscomi, F. N.; Robinson, P.; Firth, G.; Adawi, A. M.; Bouillard, J.-S. G.; Stasiuk, G. J., A dual-modal SERS/fluorescence gold nanoparticle probe for mitochondrial imaging. *ChemPlusChem* **2017,** *82* (5), 674-680.

76. Woo, M.-A.; Lee, S.-M.; Kim, G.; Baek, J.; Noh, M. S.; Kim, J. E.; Park, S. J.; Minai-Tehrani, A.; Park, S.-C.; Seo, Y. T.; Kim, Y.-K.; Lee, Y.-S.; Jeong, D. H.; Cho, M.-H., Multiplex immunoassay using fluorescent-surface enhanced Raman spectroscopic dots for the detection of bronchioalveolar stem cells in murine lung. *Analytical Chemistry* **2009,** *81* (3), 1008-1015.

77. Kim, K.; Lee, H. B.; Choi, J.-Y.; Shin, K. S., Silver-coated dye-embedded silica beads: a core material of dual tagging sensors based on fluorescence and Raman scattering. *ACS Applied Materials & Interfaces* **2011,** *3* (2), 324-330.

78. Zong, S.; Wang, Z.; Zhang, R.; Wang, C.; Xu, S.; Cui, Y., A multiplex and straightforward aqueous phase immunoassay protocol through the combination of SERS-fluorescence dual mode nanoprobes and magnetic nanobeads. *Biosensors and Bioelectronics* **2013,** *41*, 745-751.

79. Wang, Z.; Zong, S.; Li, W.; Wang, C.; Xu, S.; Chen, H.; Cui, Y., SERS-fluorescence joint spectral encoding using organic–metal–QD hybrid nanoparticles with a huge encoding capacity for high-throughput biodetection: putting theory into practice. *Journal of the American Chemical Society* **2012,** *134* (6), 2993-3000.

80. Niu, X.; Chen, H.; Wang, Y.; Wang, W.; Sun, X.; Chen, L., Upconversion fluorescence-SERS dual-mode tags for cellular and in vivo imaging. *ACS Applied Materials & Interfaces* **2014,** *6* (7), 5152-5160.

81. Lin, S.-Y., An overview of advanced hyphenated techniques for simultaneous analysis and characterization of polymeric materials. *Critical Reviews in Solid State and Materials Sciences* **2016,** *41* (6), 482-530.

82. Kim, J.; Piao, Y.; Hyeon, T., Multifunctional nanostructured materials for multimodal imaging, and simultaneous imaging and therapy. *Chemical Society Reviews* **2009,** *38* (2), 372-390.

83. Torres, I. E., PET/CT: underlying physics, instrumentation, and advances. *Radiologia* **2017,** *59* (5), 431-445.

84. de Gea Fernández, J.; Mronga, D.; Günther, M.; Knobloch, T.; Wirkus, M.; Schröer, M.; Trampler, M.; Stiene, S.; Kirchner, E.; Bargsten, V., Multimodal sensor-based whole-body control for human–robot collaboration in industrial settings. *Robotics and Autonomous Systems* **2017,** *94*, 102-119.

85. Stefan-van Staden, R.-I.; Moldoveanu, I., Multimode sensors based on nanostructured materials for simultaneous screening of biological fluids for specific breast cancer and Hepatitis B biomarkers. *Journal of the Electrochemical Society* **2014,** *161* (4), B45-B48.

86. Nieuwoudt, M. K.; Holroyd, S. E.; McGoverin, C. M.; Simpson, M. C.; Williams, D. E. In *Rapid, sensitive and reproducible method for point-of-collection screening of liquid milk for adulterants using a portable Raman spectrometer with novel*

optimized sample well, Optical Diagnostics and Sensing XVII: Toward Point-of-Care Diagnostics, International Society for Optics and Photonics: 2017; p 1007212.

87. Van Duyne, R.; Jeanmaire, D., Surface Raman spectroelectochemistry: part1. heterocyclic, aromatic, and aliphatic Amines adsorbed on the anodized silver electrode. *Journal of Electroanalytical Chemistry* **1977,** *84*, 1-20.

88. Nie, S.; Emory, S. R., Probing single molecules and single nanoparticles by surface-enhanced Raman scattering. *Science* **1997,** *275* (5303), 1102-1106.

89. Kneipp, K.; Wang, Y.; Kneipp, H.; Perelman, L. T.; Itzkan, I.; Dasari, R. R.; Feld, M. S., Single molecule detection using surface-enhanced Raman scattering (SERS). *Physical Review Letters* **1997,** *78* (9), 1667.

90. Wokaun, A., Surface-enhanced electromagnetic processes. In *Solid state physics*, Elsevier: 1984; Vol. 38, pp 223-294.

91. Vo-Dinh, T.; Fales, A. M.; Griffin, G. D.; Khoury, C. G.; Liu, Y.; Ngo, H.; Norton, S. J.; Register, J. K.; Wang, H.-N.; Yuan, H., Plasmonic nanoprobes: from chemical sensing to medical diagnostics and therapy. *Nanoscale* **2013,** *5* (21), 10127-10140.

92. Talley, C. E.; Jusinski, L.; Hollars, C. W.; Lane, S. M.; Huser, T., Intracellular pH sensors based on surface-enhanced Raman scattering. *Analytical Chemistry* **2004,** *76* (23), 7064-7068.

93. Zong, S.; Wang, Z.; Yang, J.; Cui, Y., Intracellular pH sensing using p-aminothiophenol functionalized gold nanorods with low cytotoxicity. *Analytical Chemistry* **2011,** *83* (11), 4178-4183.

94. Zheng, X.-S.; Hu, P.; Cui, Y.; Zong, C.; Feng, J.-M.; Wang, X.; Ren, B., BSA-coated nanoparticles for improved SERS-based intracellular pH sensing. *Analytical Chemistry* **2014,** *86* (24), 12250-12257.

95. Gu, X.; Wang, H.; Schultz, Z. D.; Camden, J. P., Sensing glucose in urine and serum and hydrogen peroxide in living cells by use of a novel boronate nanoprobe based on surface-enhanced raman spectroscopy. *Analytical Chemistry* **2016,** *88* (14), 7191-7197.

96. Li, D. W.; Qu, L. L.; Hu, K.; Long, Y. T.; Tian, H., Monitoring of endogenous hydrogen sulfide in living cells using surface-enhanced Raman scattering. *Angewandte Chemie International Edition* **2015,** *54* (43), 12758-12761.

97. Cao, Y.; Li, D.-W.; Zhao, L.-J.; Liu, X.-Y.; Cao, X.-M.; Long, Y.-T., Highly selective detection of carbon monoxide in living cells by palladacycle carbonylation-based surface enhanced Raman spectroscopy nanosensors. *Analytical Chemistry* **2015,** *87* (19), 9696-9701.

98. Rivera_Gil, P.; Vazquez-Vazquez, C.; Giannini, V.; Callao, M. P.; Parak, W. J.; Correa-Duarte, M. A.; Alvarez-Puebla, R. A., Plasmonic nanoprobes for real-time optical monitoring of nitric oxide inside living cells. *Angewandte Chemie* **2013,** *125* (51), 13939-13943.

99. Wang, Y.; Deng, X.; Liu, J.; Tang, H.; Jiang, J., Surface enhanced Raman scattering based sensitive detection of histone demethylase activity using a formaldehyde-selective reactive probe. *Chemical Communications* **2013,** *49* (76), 8489-8491.

100. Collier, B. B.; McShane, M. J., Dynamic windowing algorithm for the fast and accurate determination of luminescence lifetimes. *Analytical Chemistry* **2012,** *84* (11), 4725-4731.

101. Collier, B. B.; McShane, M. J., Temperature compensation of oxygen sensing films utilizing a dynamic dual lifetime calculation technique. *IEEE Sensors Journal* **2014,** *14* (8), 2755-2764.

102. McGown, L. B.; Nithipatikom, K., Molecular fluorescence and phosphorescence. *Applied Spectroscopy Reviews* **2000,** *35* (4), 353-393.

103. Borisov, S.; Nuss, G.; Klimant, I., Red light-excitable oxygen sensing materials based on platinum (II) and palladium (II) benzoporphyrins. *Analytical Chemistry* **2008,** *80* (24), 9435-9442.

104. Vinogradov, S. A.; Lo, L.-W.; Jenkins, W. T.; Evans, S. M.; Koch, C.; Wilson, D. F., Noninvasive imaging of the distribution in oxygen in tissue in vivo using near-infrared phosphors. *Biophysical Journal* **1996,** *70* (4), 1609-1617.

105. Vinogradov, S. A.; Wilson, D. F., Metallotetrabenzoporphyrins. New phosphorescent probes for oxygen measurements. *Journal of the Chemical Society, Perkin Transactions 2* **1995,** 103-111.

106. Borisov, S. M.; Vasylevska, A. S.; Krause, C.; Wolfbeis, O. S., Composite luminescent material for dual sensing of oxygen and temperature. *Advanced Functional Materials* **2006,** *16* (12), 1536-1542.

107. Liebsch, G.; Klimant, I.; Frank, B.; Holst, G.; Wolfbeis, O. S., Luminescence lifetime imaging of oxygen, pH, and carbon dioxide distribution using optical sensors. *Applied Spectroscopy* **2000,** *54* (4), 548-559.

108. Neurauter, G.; Klimant, I.; Wolfbeis, O. S., Microsecond lifetime-based optical carbon dioxide sensor using luminescence resonance energy transfer. *Analytica Chimica Acta* **1999,** *382* (1-2), 67-75.

109. You, Y.-H.; Nagaraja, A. T.; Biswas, A.; Hwang, J.-H.; Coté, G. L.; McShane, M. J., SERS-active smart hydrogels with modular microdomains: from pH to glucose sensing. *IEEE Sensors Journal* **2017,** *17* (4), 941-950.

110. Biswas, A.; Nagaraja, A.; You, Y.; Roberts, J.; McShane, M. J., Cross-linked nanofilms for tunable permeability control in a composite microdomain system. *RSC Advances* **2016**.

111. Bornhoeft, L. R.; Biswas, A.; McShane, M. J., Composite hydrogels with engineered microdomains for optical glucose sensing at low oxygen conditions. *Biosensors* **2017,** *7* (1), 8.

112. Biswas, A.; Bornhoeft, L. R.; Banerjee, S.; You, Y.-H.; McShane, M. J., Composite hydrogels containing bioactive microreactors for optical enzymatic lactate sensing. *ACS Sensors* **2017,** *2* (11), 1584-1588.

113. Decher, G., Fuzzy nanoassemblies: toward layered polymeric multicomposites. *Science* **1997,** *277* (5330), 1232-1237.

114. Sukhorukov, G. B.; Donath, E.; Lichtenfeld, H.; Knippel, E.; Knippel, M.; Budde, A.; Möhwald, H., Layer-by-layer self assembly of polyelectrolytes on colloidal

particles. *Colloids and Surfaces A: Physicochemical and Engineering Aspects* **1998,** *137* (1), 253-266.

115. Hanson, M. A.; Ge, X.; Kostov, Y.; Brorson, K. A.; Moreira, A. R.; Rao, G., Comparisons of optical pH and dissolved oxygen sensors with traditional electrochemical probes during mammalian cell culture. *Biotechnology and Bioengineering* **2007,** *97* (4), 833-841.

116. Naciri, M.; Kuystermans, D.; Al-Rubeai, M., Monitoring pH and dissolved oxygen in mammalian cell culture using optical sensors. *Cytotechnology* **2008,** *57* (3), 245-250.

117. Deepa, N.; Ganesh, A. B., Minimally invasive fluorescence sensing system for real-time monitoring of bacterial cell cultivation. *Instrumentation Science & Technology* **2017,** *45* (1), 85-100.

118. Roberts, J. R.; Ritter, D. W.; McShane, M. J., A design full of holes: functional nanofilm-coated microdomains in alginate hydrogels. *Journal of Materials Chemistry B* **2013,** *1* (25), 3195-3201.

119. Laetsch, T.; Downs, R. In *Software for identification and refinement of cell parameters from powder diffraction data of minerals using the RRUFF Project and American Mineralogist Crystal Structure Databases*, 19th General Meeting of the International Mineralogical Association, Kobe, Japan, 2006; p e28.

120. Biswas, A.; Nagaraja, A. T.; You, Y.-H.; Roberts, J. R.; McShane, M. J., Cross-linked nanofilms for tunable permeability control in a composite microdomain system. *RSC Advances* **2016,** *6* (75), 71781-71790.

121. Won, Y.-H.; Jang, H. S.; Chung, D.-W.; Stanciu, L. A., Multifunctional calcium carbonate microparticles: Synthesis and biological applications. *Journal of Materials Chemistry* **2010,** *20* (36), 7728-7733.

122. Vinogradov, S. A.; Wilson, D. F., Extended porphyrins. In *Oxygen transport to tissue XVIII*, Springer: 1997; pp 597-603.

123. Mortimer, M.; Gogos, A.; Bartolomé, N.; Kahru, A.; Bucheli, T. D.; Slaveykova, V. I., Potential of hyperspectral imaging microscopy for semi-quantitative analysis of nanoparticle uptake by protozoa. *Environmental Science & Technology* **2014,** *48* (15), 8760-8767.

124. Kim, T.; Lee, C.-H.; Joo, S.-W.; Lee, K., Kinetics of gold nanoparticle aggregation: experiments and modeling. *Journal of Colloid and Interface Science* **2008,** *318* (2), 238-243.

125. Wei, H.; Shen, Q.; Zhao, Y.; Wang, D.-J.; Xu, D.-F., Influence of polyvinylpyrrolidone on the precipitation of calcium carbonate and on the transformation of vaterite to calcite. *Journal of Crystal Growth* **2003,** *250* (3), 516-524.

126. Sun, F.; Zhang, P.; Bai, T.; Galvan, D. D.; Hung, H.-C.; Zhou, N.; Jiang, S.; Yu, Q., Functionalized plasmonic nanostructure arrays for direct and accurate mapping extracellular pH of living cells in complex media using SERS. *Biosensors and Bioelectronics* **2015,** *73*, 202-207.

127. Rodriguez, I. H.; Lopez-Reyes, G.; Llanos, D.; Perez, F. R., Automatic raman spectra processing for Exomars. In *Mathematics of planet earth*, Springer: 2014; pp 127-130.

128. Ostrowski, J. C.; Mikhailovsky, A.; Bussian, D. A.; Summers, M. A.; Buratto, S. K.; Bazan, G. C., Enhancement of phosphorescence by surface-plasmon resonances in colloidal metal nanoparticles: the role of aggregates. *Advanced Functional Materials* **2006,** *16* (9), 1221-1227.

129. Pan, S.; Rothberg, L. J., Enhancement of platinum octaethyl porphyrin phosphorescence near nanotextured silver surfaces. *Journal of the American Chemical Society* **2005,** *127* (16), 6087-6094.

130. Bell, S. E.; McCourt, M. R., SERS enhancement by aggregated Au colloids: effect of particle size. *Physical Chemistry Chemical Physics* **2009,** *11* (34), 7455-7462.

131. Jana, N. R.; Pal, T., Anisotropic metal nanoparticles for use as surface-enhanced Raman substrates. *Advanced Materials* **2007,** *19* (13), 1761-1765.

132. Dasary, S. S.; Singh, A. K.; Senapati, D.; Yu, H.; Ray, P. C., Gold nanoparticle based label-free SERS probe for ultrasensitive and selective detection of trinitrotoluene. *Journal of the American Chemical Society* **2009,** *131* (38), 13806-13812.

133. Shao, Q.; Que, R.; Shao, M.; Cheng, L.; Lee, S. T., Copper nanoparticles grafted on a silicon wafer and their excellent surface-enhanced Raman scattering. *Advanced Functional Materials* **2012,** *22* (10), 2067-2070.

134. von Maltzahn, G.; Centrone, A.; Park, J. H.; Ramanathan, R.; Sailor, M. J.; Hatton, T. A.; Bhatia, S. N., SERS-coded gold nanorods as a multifunctional platform for densely multiplexed near-infrared imaging and photothermal heating. *Advanced Materials* **2009,** *21* (31), 3175-3180.

135. Rodríguez-Lorenzo, L.; Krpetic, Z.; Barbosa, S.; Alvarez-Puebla, R. A.; Liz-Marzán, L. M.; Prior, I. A.; Brust, M., Intracellular mapping with SERS-encoded gold nanostars. *Integrative Biology* **2011,** *3* (9), 922-926.

136. Fang, J.; Du, S.; Lebedkin, S.; Li, Z.; Kruk, R.; Kappes, M.; Hahn, H., Gold mesostructures with tailored surface topography and their self-assembly arrays for surface-enhanced Raman spectroscopy. *Nano letters* **2010,** *10* (12), 5006-5013.

137. Xie, J.; Zhang, Q.; Lee, J. Y.; Wang, D. I., The synthesis of SERS-active gold nanoflower tags for in vivo applications. *ACS nano* **2008,** *2* (12), 2473-2480.

138. Cherukulappurath, S., Surface-enhanced Raman spectroscopy for biomedical applications: a review. *Sensors & Transducers* **2016,** *197* (2), 1-13.

139. Yonzon, C. R.; Stuart, D. A.; Zhang, X.; McFarland, A. D.; Haynes, C. L.; Van Duyne, R. P., Towards advanced chemical and biological nanosensors—an overview. *Talanta* **2005,** *67* (3), 438-448.

140. Shah, N. C.; Lyandres, O.; Walsh, J. T.; Glucksberg, M. R.; Van Duyne, R. P., Lactate and sequential lactate-glucose sensing using surface-enhanced Raman spectroscopy. *Analytical Chemistry* **2007,** *79* (18), 6927-6932.

141. Abu Hatab, N. A.; Oran, J. M.; Sepaniak, M. J., Surface-enhanced Raman spectroscopy substrates created via electron beam lithography and nanotransfer printing. *ACS Nano* **2008,** *2* (2), 377-385.

142. Im, H.; Lesuffleur, A.; Lindquist, N. C.; Oh, S.-H., Plasmonic nanoholes in a multichannel microarray format for parallel kinetic assays and differential sensing. *Analytical Chemistry* **2009,** *81* (8), 2854-2859.

143. Betz, J. F.; Yu, W. W.; Cheng, Y.; White, I. M.; Rubloff, G. W., Simple SERS substrates: powerful, portable, and full of potential. *Physical Chemistry Chemical Physics* **2014,** *16* (6), 2224-2239.

144. Stebounova, L. V.; Guio, E.; Grassian, V. H., Silver nanoparticles in simulated biological media: a study of aggregation, sedimentation, and dissolution. *Journal of Nanoparticle Research* **2011,** *13* (1), 233-244.

145. De Jong, W. H.; Hagens, W. I.; Krystek, P.; Burger, M. C.; Sips, A. J.; Geertsma, R. E., Particle size-dependent organ distribution of gold nanoparticles after intravenous administration. *Biomaterials* **2008,** *29* (12), 1912-1919.

146. Helton, K. L.; Ratner, B. D.; Wisniewski, N. A., Biomechanics of the sensor-tissue interface—effects of motion, pressure, and design on sensor performance and the foreign body response—part I: theoretical framework. *Journal of Diabetes Science and Technology* **2011,** *5* (3), 632-646.

147. Zolnik, B. S.; Gonzalez-Fernandez, A.; Sadrieh, N.; Dobrovolskaia, M. A., Minireview: nanoparticles and the immune system. *Endocrinology* **2010,** *151* (2), 458-465.

148. Nel, A.; Xia, T.; Mädler, L.; Li, N., Toxic potential of materials at the nanolevel. *Science* **2006,** *311* (5761), 622-627.

149. Stuart, D. A.; Yuen, J. M.; Shah, N.; Lyandres, O.; Yonzon, C. R.; Glucksberg, M. R.; Walsh, J. T.; Van Duyne, R. P., In vivo glucose measurement by surface-enhanced Raman spectroscopy. *Analytical Chemistry* **2006,** *78* (20), 7211-7215.

150. Register, J. K.; Fales, A. M.; Wang, H.-N.; Norton, S. J.; Cho, E. H.; Boico, A.; Pradhan, S.; Kim, J.; Schroeder, T.; Wisniewski, N. A., In vivo detection of SERS-encoded plasmonic nanostars in human skin grafts and live animal models. *Analytical and Bioanalytical Chemistry* **2015,** *407* (27), 8215-8224.

151. Radtchenko, I. L.; Sukhorukov, G. B.; Möhwald, H., Incorporation of macromolecules into polyelectrolyte micro-and nanocapsules via surface controlled precipitation on colloidal particles. *Colloids and Surfaces A: Physicochemical and Engineering Aspects* **2002,** *202* (2-3), 127-133.

152. Sukhorukov, G.; Donath, E.; Moya, S.; Susha, A.; Voigt, A.; Hartmann, J.; Mohwald, H., Microencapsulation by means of step-wise adsorption of polyelectrolytes. *Journal of Microencapsulation* **2000,** *17* (2), 177-185.

153. Miller, M. D.; Bruening, M. L., Controlling the nanofiltration properties of multilayer polyelectrolyte membranes through variation of film composition. *Langmuir* **2004,** *20* (26), 11545-11551.

154. Weibel, M. K.; Bright, H. J., The glucose oxidase mechanism interpretation of pH dependence. *Journal of Biological Chemistry* **1971,** *246* (9), 2734-2744.

155. Naka, T.; Sakamoto, N., Kinetics of membrane-bound enzymes - validity of quasi-steady-state approximation for a Michaelis-Menten-type reaction. *Journal of Membrane Science* **1992,** *74* (1-2), 159-170.

156. Brown, J. Q.; McShane, M. J., Modeling of spherical fluorescent glucose microsensor systems: design of enzymatic smart tattoos. *Biosensors and Bioelectronics* **2006,** *21* (9), 1760-1769.

157. Bastús, N. G.; Comenge, J.; Puntes, V., Kinetically controlled seeded growth synthesis of citrate-stabilized gold nanoparticles of up to 200 nm: size focusing versus Ostwald ripening. *Langmuir* **2011,** *27* (17), 11098-11105.

158. Hong, S.; Li, X., Optimal size of gold nanoparticles for surface-enhanced Raman spectroscopy under different conditions. *Journal of Nanomaterials* **2013,** *2013*, 49.

159. Jaworska, A.; Jamieson, L. E.; Malek, K.; Campbell, C. J.; Choo, J.; Chlopicki, S.; Baranska, M., SERS-based monitoring of the intracellular pH in endothelial cells: the influence of the extracellular environment and tumour necrosis factor-α. *Analyst* **2015,** *140* (7), 2321-2329.

160. Petrov, A. I.; Volodkin, D. V.; Sukhorukov, G. B., Protein—calcium carbonate coprecipitation: a tool for protein encapsulation. *Biotechnology Progress* **2005,** *21* (3), 918-925.

161. Malaisamy, R.; Bruening, M. L., High-flux nanofiltration membranes prepared by adsorption of multilayer polyelectrolyte membranes on polymeric supports. *Langmuir* **2005,** *21* (23), 10587-10592.

162. Haiss, W.; Thanh, N. T.; Aveyard, J.; Fernig, D. G., Determination of size and concentration of gold nanoparticles from UV-vis spectra. *Analytical Chemistry* **2007,** *79* (11), 4215-4221.

163. Basu, S.; Pande, S.; Jana, S.; Bolisetty, S.; Pal, T., Controlled interparticle spacing for surface-modified gold nanoparticle aggregates. *Langmuir* **2008,** *24* (10), 5562-5568.

164. Irving, R. J.; Nelander, L.; Wadso, I., Thermodynamics of the ionization of some thiols in aqueous solution. *Acta Chemica Scandinavica* **1964,** *18* (3), 769-787.

165. Bishnoi, S. W.; Rozell, C. J.; Levin, C. S.; Gheith, M. K.; Johnson, B. R.; Johnson, D. H.; Halas, N. J., All-optical nanoscale pH meter. *Nano letters* **2006,** *6* (8), 1687-1692.

166. Unruh, R. M.; Roberts, J. R.; Nichols, S. P.; Gamsey, S.; Wisniewski, N. A.; McShane, M. J., Preclinical evaluation of Poly (HEMA-co-acrylamide) hydrogels encapsulating glucose oxidase and palladium benzoporphyrin as fully omplantable glucose sensors. *Journal of Diabetes Science and Technology* **2015**, *9* (5), 985-992.

167. Wencel, D.; Abel, T.; McDonagh, C., Optical chemical pH sensors. *Analytical Chemistry* **2014,** *86* (1), 15-29.

168. Jamieson, L.; Jaworska, A.; Jiang, J.; Baranska, M.; Harrison, D.; Campbell, C., Simultaneous intracellular redox potential and pH measurements in live cells using SERS nanosensors. *Analyst* **2015,** *140* (7), 2330-2335.

169. Guerrini, L.; Arenal, R.; Mannini, B.; Chiti, F.; Pini, R.; Matteini, P.; Alvarez-Puebla, R. A., SERS detection of amyloid oligomers on metallorganic-decorated plasmonic beads. *ACS Applied Materials & Interfaces* **2015,** *7* (18), 9420-9428.

170. Schelvis, J. P.; Pun, D.; Goyal, N.; Sokolova, O., Resonance Raman spectra of the neutral and anionic radical semiquinones of flavin adenine dinucleotide in glucose oxidase revisited. *Journal of Raman Spectroscopy* **2006,** *37* (8), 822-829.

171. Cunningham, D. D.; Stenken, J. A., *In vivo glucose sensing*. John Wiley & Sons 2009, 4.

172. You, Y.-H.; Nagaraja, A.; Biswas, A.; Marks, H.; Coté, G. L.; McShane, M. J. In *SERS-based hydrogel sensors for pH and enzymatic substrates*, Sensors, 2015 IEEE, IEEE: 2015; pp 1-4.

173. Hsu, P.-H.; Tsai, T.-H.; Chiang, H. K. In *In vivo blood lactic acid monitoring using microdialysis and surface-enhanced Raman spectroscopy*, Nanobiosystems: Processing, Characterization, and Applications, International Society for Optics and Photonics: 2008; p 70400R.

174. Torul, H.; Çiftçi, H.; Çetin, D.; Suludere, Z.; Boyacı, I. H.; Tamer, U., Paper membrane-based SERS platform for the determination of glucose in blood samples. *Analytical and Bioanalytical Chemistry* **2015,** *407* (27), 8243-8251.

175. Kim, D. J.; Jeon, T. Y.; Park, S. G.; Han, H. J.; Im, S. H.; Kim, D. H.; Kim, S. H., Uniform microgels containing agglomerates of silver nanocubes for molecular size-selectivity and high SERS activity. *Small* **2017,** *13* (23), 1604048.

176. Yue, S.; Sun, X.-T.; Wang, Y.; Zhang, W.-S.; Xu, Z.-R., Microparticles with size/charge selectivity and pH response for SERS monitoring of 6-thioguanine in blood serum. *Sensors and Actuators B: Chemical* **2018,** *273*, 1539-1547.

177. Lopez, A.; Lovato, F.; Oh, S. H.; Lai, Y. H.; Filbrun, S.; Driskell, E. A.; Driskell, J. D., SERS immunoassay based on the capture and concentration of antigen-assembled gold nanoparticles. *Talanta* **2016,** *146*, 388-393.

178. Graham, D.; Stevenson, R.; Thompson, D. G.; Barrett, L.; Dalton, C.; Faulds, K., Combining functionalised nanoparticles and SERS for the detection of DNA relating to disease. *Faraday Discussions* **2011,** *149* (1), 291-299.

179. Graham, D.; Thompson, D. G.; Smith, W. E.; Faulds, K., Control of enhanced Raman scattering using a DNA-based assembly process of dye-coded nanoparticles. *Nature Nanotechnology* **2008,** *3* (9), 548-551.

180. Jia, Y.; Shmakov, S. N.; Pinkhassik, E., Controlled permeability in porous polymer nanocapsules enabling size-and charge-selective SERS nanoprobes. *ACS Applied Materials & Interfaces* **2016,** *8* (30), 19755-19763.

181. Biswas, A.; Nagaraja, A. T.; McShane, M. J., Fabrication of nanocapsule carriers from multilayer-coated vaterite calcium carbonate nanoparticles. *ACS Applied Materials & Interfaces* **2014,** *6* (23), 21193-21201.

182. Biswas, A.; Banerjee, S.; Gart, E. V.; Nagaraja, A. T.; McShane, M. J., Gold nanocluster containing polymeric microcapsules for intracellular ratiometric fluorescence biosensing. *ACS Omega* **2017,** *2* (6), 2499-2506.

183. Schechinger, M.; Marks, H.; Locke, A.; Choudhury, M.; Cote, G., Development of a miRNA surface-enhanced Raman scattering assay using benchtop and handheld Raman systems. *Journal of Biomedical Optics* **2018,** *23* (1), 017002.

184. Leopold, N.; Lendl, B., A new method for fast preparation of highly surface-enhanced Raman scattering (SERS) active silver colloids at room temperature by reduction of silver nitrate with hydroxylamine hydrochloride. *The Journal of Physical Chemistry B* **2003,** *107*, 5723-5727.

185. Haiss, W.; Thanh, N. T.; Aveyard, J.; Fernig, D. G., Determination of size and concentration of gold nanoparticles from UV− Vis spectra. *Analytical Chemistry* **2007,** *79* (11), 4215-4221.

186. Paramelle, D.; Sadovoy, A.; Gorelik, S.; Free, P.; Hobley, J.; Fernig, D. G., A rapid method to estimate the concentration of citrate capped silver nanoparticles from UV-visible light spectra. *Analyst* **2014,** *139* (19), 4855-4861.

187. Tenzer, S.; Docter, D.; Rosfa, S.; Wlodarski, A.; Kuharev, J.; Rekik, A.; Knauer, S. K.; Bantz, C.; Nawroth, T.; Bier, C.; Sirirattanapan, J.; Mann, W.; Treuel, L.; Zellner, R.; Maskos, M.; Schild, H.; Stauber, R. H., Nanoparticle size is a critical physicochemical determinant of the human blood plasma corona: a comprehensive quantitative proteomic analysis. *ACS Nano* **2011,** *5* (9), 7155-7167.

188. Liu, W.; Rose, J.; Plantevin, S.; Auffan, M.; Bottero, J.-Y.; Vidaud, C., Protein corona formation for nanomaterials and proteins of a similar size: hard or soft corona? *Nanoscale* **2013,** *5* (4), 1658-1668.

189. Li, M.; Cushing, S. K.; Zhang, J.; Lankford, J.; Aguilar, Z. P.; Ma, D.; Wu, N., Shape-dependent surface-enhanced Raman scattering in gold–Raman-probe–silica sandwiched nanoparticles for biocompatible applications. *Nanotechnology* **2012,** *23* (11), 115501.

190. Vetrone, S. A.; Huarng, M. C.; Alocilja, E. C., Detection of non-PCR amplified S. enteritidis genomic DNA from food matrices using a gold-nanoparticle DNA biosensor: a proof-of-concept study. *Sensors* **2012,** *12* (8), 10487-10499.

191. Gaponik, N.; Radtchenko, I. L.; Sukhorukov, G. B.; Rogach, A. L., Luminescent Polymer microcapsules addressable by a magnetic field. *Langmuir* **2004,** *20* (4), 1449-1452.

192. Berger, A. G.; Restaino, S. M.; White, I. M., Vertical-flow paper SERS system for therapeutic drug monitoring of flucytosine in serum. *Analytica Chimica Acta* **2017,** *949*, 59-66.

193. Lee, C. H.; Tian, L.; Singamaneni, S., Paper-based SERS swab for rapid trace detection on real-world surfaces. *ACS Applied Materials & Interfaces* **2010,** *2* (12), 3429-3435.

194. Chamuah, N.; Hazarika, A.; Hatiboruah, D.; Nath, P., SERS on paper: an extremely low cost technique to measure Raman signal. *Journal of Physics D: Applied Physics* **2017,** *50* (48), 485601.

195. Ngo, Y. H.; Li, D.; Simon, G. P.; Garnier, G., Gold Nanoparticle–Paper as a Three-dimensional surface enhanced Raman scattering substrate. *Langmuir* **2012,** *28* (23), 8782-8790.

196. Ladam, G.; Gergely, C.; Senger, B.; Decher, G.; Voegel, J.-C.; Schaaf, P.; Cuisinier, F. J., Protein interactions with polyelectrolyte multilayers: interactions between human serum albumin and polystyrene sulfonate/polyallylamine multilayers. *Biomacromolecules* **2000,** *1* (4), 674-687.

197. Tang, H.; Zhu, C.; Meng, G.; Wu, N., Surface-enhanced Raman scattering sensors for food safety and environmental monitoring. *Journal of the Electrochemical Society* **2018,** *165* (8), B3098-B3118.

198. Wang, C.; Chen, Y.; Wang, T.; Ma, Z.; Su, Z., Biorecognition-driven self-assembly of gold nanorods: a rapid and sensitive approach toward antibody sensing. *Chemistry of Materials* **2007,** *19* (24), 5809-5811.

199. Thanh, N. T. K.; Rosenzweig, Z., Development of an aggregation-based immunoassay for anti-protein a using gold nanoparticles. *Analytical Chemistry* **2002,** *74* (7), 1624-1628.

200. Pavlov, V.; Xiao, Y.; Shlyahovsky, B.; Willner, I., Aptamer-functionalized Au nanoparticles for the amplified optical detection of thrombin. *Journal of the American Chemical Society* **2004,** *126* (38), 11768-11769.

201. Medley, C. D.; Smith, J. E.; Tang, Z.; Wu, Y.; Bamrungsap, S.; Tan, W., Gold nanoparticle-based colorimetric assay for the direct detection of cancerous cells. *Analytical Chemistry* **2008,** *80* (4), 1067-1072.

202. Zhao, W.; Chiuman, W.; Brook, M. A.; Li, Y., Simple and rapid colorimetric biosensors based on DNA aptamer and noncrosslinking gold nanoparticle aggregation. *ChemBioChem* **2007,** *8* (7), 727-731.

203. Zhang, J.; Wang, L.; Pan, D.; Song, S.; Boey, F. Y.; Zhang, H.; Fan, C., Visual cocaine detection with gold nanoparticles and rationally engineered aptamer structures. *Small* **2008,** *4* (8), 1196-1200.

204. Ellington, A. D.; Szostak, J. W., In vitro selection of RNA molecules that bind specific ligands. *Nature* **1990,** *346*, 818-822.

205. Kim, Y.-S.; Oh, C. S.; Kim, M. J.; Ki, H. C.; Hong, J. Y.; Kim, S.; Shin, D. H., Forensic anthropological study on saw marks appearing on the tibiae of a Joseon skeleton. *Korean Journal of Physical Anthropology* **2014,** *27* (1), 29-37.

206. Sefah, K.; Shangguan, D.; Xiong, X.; O'Donoghue, M. B.; Tan, W., Development of DNA aptamers using cell-SELEX. *Nature Protocols* **2010,** *5*, 1169-1185.

207. Chen, A.; Yan, M.; Yang, S., Split aptamers and their applications in sandwich aptasensors. *TrAC Trends in Analytical Chemistry* **2016,** *80*, 581-593.

208. Li, F.; Zhang, J.; Cao, X.; Wang, L.; Li, D.; Song, S.; Ye, B.; Fan, C., Adenosine detection by using gold nanoparticles and designed aptamer sequences. *Analyst* **2009,** *134* (7), 1355-1360.

209. Yang, X.; Huang, J.; Wang, Q.; Wang, K.; Yang, L.; Huo, X., A one-step sensitive dynamic light scattering method for adenosine detection using split aptamer fragments. *Analytical Methods* **2011,** *3* (1), 59-61.

210. Heo, J. H.; Cho, H. H.; Lee, J. H., Surfactant-free nanoparticle–DNA complexes with ultrahigh stability against salt for environmental and biological sensing. *Analyst* **2014,** *139* (22), 5936-5944.

211. Liu, J.; Lu, Y., Preparation of aptamer-linked gold nanoparticle purple aggregates for colorimetric sensing of analytes. *Nature Protocols* **2006,** *1* (1), 246-252.

212. Lévy, R.; Thanh, N. T.; Doty, R. C.; Hussain, I.; Nichols, R. J.; Schiffrin, D. J.; Brust, M.; Fernig, D. G., Rational and combinatorial design of peptide capping ligands for gold nanoparticles. *Journal of the American Chemical Society* **2004,** *126* (32), 10076-10084.

213. Zhao, W.; Brook, M. A.; Li, Y., Design of gold nanoparticle-based colorimetric biosensing assays. *ChemBioChem* **2008,** *9* (15), 2363-2371.

214. Dinish, U.; Fu, C. Y.; Soh, K. S.; Ramaswamy, B.; Kumar, A.; Olivo, M., Highly sensitive SERS detection of cancer proteins in low sample volume using hollow core photonic crystal fiber. *Biosensors and Bioelectronics* **2012,** *33* (1), 293-298.

215. Krpetić, Ž.; Guerrini, L.; Larmour, I. A.; Reglinski, J.; Faulds, K.; Graham, D., Importance of nanoparticle size in colorimetric and SERS-based multimodal trace detection of Ni (II) ions with functional gold nanoparticles. *Small* **2012,** *8* (5), 707-714.

216. Afseth, N. K.; Bloomfield, M.; Wold, J. P.; Matousek, P., A novel approach for subsurface through-skin analysis of salmon using spatially offset Raman spectroscopy (SORS). *Applied Spectroscopy* **2014,** *68* (2), 255-262.